VERIFICATION AND VALIDATION OF A GEOMODEL AIMED AT SIMULATING WELLBORE COMPLETION VIA SHAPED-CHARGE JET PERFORATION OF METAL AND PENETRATION INTO SANDSTONE

by

David Mark Austin

A thesis submitted to the faculty of
The University of Utah
in partial fulfillment of the requirements for the degree of

Master of Science

Department of Mechanical Engineering

The University of Utah

December 2013

The University of Utah Graduate School

STATEMENT OF THESIS APPROVAL

The thesis of **David Mark Austin**

has been approved by the following supervisory committee members:

Rebecca M. Brannon	, Chair	**27-June-2013** Date Approved
Daniel O. Adams	, Member	**27-June-2013** Date Approved
John D. McLennan	, Member	**27-June-2013** Date Approved

and by **Tim Ameel** , Chair/Dean of

the Department/College/School of **Mechanical Engineering**

and by David B. Kieda, Dean of The Graduate School.

ABSTRACT

Verification and validation (V&V) principles are applied to assess massively parallel simulations of hypervelocity perforation of a well bore casing and subsequent penetration into oil-laden sandstone via shaped-charge jet. This technique for liberating oil from geological formations has the potential to be optimized through development of robust and accurate computational frameworks. Accordingly, the overarching objective of this research is to systematically assess the accuracy of the numerical algorithms used (verification) and the appropriateness of those equations for this engineering purpose (validation). Automated methods for single-element verification of constitutive models under a variety of loading modes are developed. This modular test suite incorporates previously documented verification tests, both generally applicable to plasticity models reducing to von Mises plasticity, as well as model specific tests of the geomechanics model (Arenisca) under continual development. These tools are extended to extract the deformation histories of single particles from full-scale Material Point Method (MPM) simulations, which helps to analyze problematic loading modes of a larger simulation on a single-processor workstation. The velocity gradient in these single-element tests must be evaluated in a manner consistent with the underlying integration algorithm used in the source simulation, which is a nontrivial observation making this new capability novel. Testing capabilities are extended to provide arbitrary loading paths similar to those extracted from full-scale penetration problems to serve as robustness and verification tests in future regression testing. A key focus of the work was devising methods to automate the testing of Arenisca and its implementation. As MPM is a relatively new approach to modeling large deformation problems, novel visualization methods are developed along with supporting Python postprocessing scripts. Analytical penetration models in the literature, which have historically been developed for hydrodynamic flow of metals, are tested for their applicability to the penetration of sandstone. A representative sampling of simulation results (some using new methods to account for confining stress) are presented to illustrate how full-scale V&V trend testing often reveals issues not evident in smaller tests, thereby helping code developers better understand, and eliminate, undesired trends or anomalies in the results.

CONTENTS

ABSTRACT . . . . **iii**

LIST OF FIGURES . . . . **vi**

LIST OF TABLES . . . . **xi**

CHAPTERS

1. INTRODUCTION **1**

- 1.1 Motivation 2
- 1.2 Objectives 4

2. DEFINITIONS AND TERMINOLOGY **5**

- 2.1 Verification & Validation Testing 5
- 2.2 Stress Tensor 6
- 2.3 Strain Tensor 7

3. LITERATURE REVIEW **8**

- 3.1 Penetration Models 8
- 3.2 Simulating Penetration 16
- 3.3 Summary 17

4. BUILDING MODEL CONFIDENCE THROUGH V&V PRACTICES **19**

- 4.1 Automation of Current Verification Tests 19
  - 4.1.1 Single Element Verification Tests 20
- 4.2 Robustness Testing 32
  - 4.2.1 Reproduction of Particle Histories as Extracted from Simulation Results 32
  - 4.2.2 Automated Single Element Testing Driven by Simulation Results 34

5. PENETRATION SIMULATION RESULTS **36**

- 5.1 Simulation Setup 36
  - 5.1.1 Sensitivity to Simulated Boundary Conditions 45
- 5.2 Simulation of Hypervelocity Long-Rod Penetration 48
- 5.3 Simulated Overburden 59

6. ISSUES EXPOSED BY V&V 68
6.1 Locking 68
6.1.1 Shear Locking 68
6.1.2 Volumetric Locking 73
6.2 Residual Pressures 78
6.3 Kinematic Anomalies 82
6.4 Erosion Algorithm 87

7. POSTPROCESSING SIMULATION RESULTS 105
7.1 Improved Visualization Techniques 105
7.2 Automated Data Decimation and Visualization 109

8. SUMMARY AND FUTURE WORK 116
8.1 Future Work 116
8.1.1 Resolution of the kinematic anomaly 116
8.1.2 Implementation of More Effective Anti-Locking Methods 117
8.1.3 Accurate Computation of the Strain Rate 117
8.1.4 Splitting/Deletion/Freezing of Damaged/Failed Particles 117
8.1.5 Continued Validation Through Comparison Against Analytical Theory and Experimental Observations using Simplified Tests 118
8.1.6 Development of a plastic strain and Damage/Permeability Correlation . 118
8.1.7 Nonlinear Non-Drucker-Prager Limit Surface 118
8.1.8 Texture, Both Intrinsic and Induced 119
8.1.9 Development of Path Dependent Plasticity Verification Tests 119
8.2 Summary 119

APPENDIX: SIMULATION INPUTS AND SOURCE CODE 122

REFERENCES 123

LIST OF FIGURES

1.1 Illustrations of (a) a shaped charge, and (b) the well-bore completions process. 1

3.1 Birkoff Bernoulli penetration. 9

4.1 Illustration of basic frame-indifference test. 21

4.2 Basic frame-indifference test results. 21

4.3 Comparison of von Mises and Arenisca yield surfaces. 22

4.4 Comparison of uniaxial strain and uniaxial stress loading. 23

4.5 Basic uniaxial strain single element test. 23

4.6 Uniaxial-strain test results both with and without hardening. 25

4.7 Constant eigen vectors with transient eigen values. 26

4.8 Geometry of Drucker-Prager verification test. 27

4.9 Linear Drucker-Prager verification test results. 27

4.10 Linear Drucker-Prager verification test results. 29

4.11 Evolving porosity as a result of yield surface cap evolution test results. 31

4.12 Hydrostatic load-unload verification test results. 31

4.13 Fluid effects verification test. 32

4.14 Error in comparing extracted and expected deformation histories of a particle at three stages of the solution. 35

5.1 Illustration representing a simulations domain and discretization. 37

5.2 Illustration of the discrete shaped-charge jet model. 37

5.3 The discrete jet description's individual cylinder properties. 38

5.4 The discrete jet description's properties as they vary with time. 39

5.5 Pressure histories at different points in space without using viscous damping. . 40

5.6 Multiple pressure histories demonstrating the effectiveness of viscous damping. 41

5.7 Comparison of penetration histories obtained for three different background grid resolutions. 46

5.8 The effects of free surface boundary type selection. 47

5.9 Comparison of fixed outer boundary effects for two versions of Arenisca each using different erosion options and penetrators. 48

5.10 Illustration of $\partial(R-Y)/\partial V^2$ over a range of slopes (b) in the linear relationship between penetration velocity and rate of penetration. 50

5.11 Plot of the linear relationship between rate of penetration and penetrating rod velocity. 51

5.12 Normalized penetration velocity versus penetrating rod velocity. 51

5.13 Dynamic strength difference $(R - Y)$ versus penetrating rod velocity. 53

5.14 Plot of penetration velocity versus penetrating rod density. 54

5.15 Plot of normalized penetration depth versus penetrating rod density. 54

5.16 Legend for combined plots of volumetric plastic strain and pressure. 55

5.17 Penetration histories for simulations investigating the combined effects of density and length. 56

5.18 Rate of penetration histories for simulations investigating the combined effects of density and length. 57

5.19 Plots of the resulting penetration channel for simulations investigating the combined effects of density and length that used erosion option *none*. 58

5.20 Plots of the resulting penetration channel for simulations investigating the combined effects of density and length that used erosion option *ZeroStress*. . . 58

5.21 Depth of penetration results for simulations having an anisotropic preconfining stress state. 60

5.22 Normalized penetration depth of a rod penetrator penetrating into drained and undrained targets at various levels of preconfinement using different erosion options. 61

5.23 Penetration histories for a tungsten rod penetrator using erosion option *none* to penetrate drained and undrained targets at various levels of preconfinement. 62

5.24 Penetration histories for a tungsten rod penetrator using erosion option *ZeroStress* to penetrate drained and undrained targets at various levels of preconfinement. 63

5.25 Rate of penetration histories for a tungsten rod penetrator using erosion option *none* to penetrate drained and undrained targets at various levels of preconfinement. 64

5.26 Rate of penetration histories for a tungsten rod penetrator using erosion option *ZeroStress* to penetrate drained and undrained targets at various levels of preconfinement. 65

5.27 Plots of the resulting penetration channel for simulations of a tungsten rod penetrator using erosion option *none* to penetrate drained targets at various levels of preconfinement. 65

5.28 Plots of the resulting penetration channel for simulations of a tungsten rod penetrator using erosion option *none* to penetrate undrained targets at various levels of preconfinement. 66

5.29 Plots of the resulting penetration channel for simulations of a tungsten rod penetrator using erosion option *ZeroStress* to penetrate drained targets at various levels of preconfinement. 66

5.30 Plots of the resulting penetration channel for simulations of a tungsten rod penetrator using erosion option *ZeroStress* to penetrate undrained targets at various levels of preconfinement. 67

6.1 Example of the characteristic checkerboarding of solution fields that presents in locking phenomena. 69

6.2 Shear locking benchmark problem illustration. 70

6.3 Shear locking benchmark problem results. 71

6.4 Shear locking benchmark problem results comparing the effects of basic strain regularization. 72

6.5 Energy versus time for third order B-spline interpolator solving the cantilever beam shear locking problem. 72

6.6 Volumetric locking benchmark problem illustration. 73

6.7 Error plots for 2-d volumetric locking problem varying Poisson's ratio by means of the bulk modulus. 76

6.8 Convergence plots for 2-d volumetric locking problem varying Poisson's ratio by means of the bulk modulus. 76

6.9 Error plots for 2-d volumetric locking problem varying Poisson's ratio by means of the shear modulus. 77

6.10 Convergence plots for 2-d volumetric locking problem varying Poisson's ratio by means of the shear modulus. 78

6.11 Error plots for 2-d volumetric locking problem varying Poisson's ratio by means of the bulk modulus. 79

6.12 Error plots for 2-d and 3-d volumetric locking problem varying Poisson's ratio by means of the shear modulus. 79

6.13 Comparison of manufactured solution problems with and without basic strain regularization. 80

6.14 Residual pressure along the penetration cavity walls. 81

6.15 Kinematic anomaly over ten µs. 83

6.16 Total kinetic energy of jet material, demonstrating energy spike. 83

6.17 Comparison of manufactured solution problems with and without enhancements to the computation of velocity gradient. 84

6.18 Von Mises equivalent stress legend for tungsten penetration of steel simulations. 85

6.19 Kinematic anomaly without using Arenisca in simulating perforation of a thick steel plate by a tungsten penetrator. 85

6.20 Kinematic anomaly breaking dam problem. 86

6.21 Simulating perforation of a thick steel plate by a segmented rod tungsten penetrator to evaluate the effects of basic strain regularization. 87

6.22 Simulated liner perforation and penetration into sandstone using the erosion option *none*. 90

6.23 Simulated well-liner perforation and penetration into sandstone using the erosion option *RemoveMass*. 91

6.24 Simulated well-liner perforation and penetration into sandstone using the erosion option *AllowNoTension*. 91

6.25 Simulated well-liner perforation and penetration into sandstone using the erosion option *AllowNoShear*. 92

6.26 Simulated well-liner perforation and penetration into sandstone using the erosion option *ZeroStress*. 92

6.27 Comparison of penetration though time for different erosion algorithms solving perforation of a well liner followed by penetration into sandstone. 93

6.28 Comparison of von Mises equivalent stress, using the erosion algorithms *none* (left) and *ZeroStress* (right), for tungsten long-rod penetration of a steel billet. 94

6.29 Comparison of von Mises equivalent stress, using the erosion algorithms *none* (left) and *ZeroStress* (right), for tungsten segmented-rod penetration of a steel billet. 95

6.30 Constant velocity discrete jet penetrator description. 98

6.31 Comparing erosion algorithm effects on depth of penetration through time, for tungsten into sandstone. 99

6.32 Combined legend for Jacobian and von Mises equivalent stress. 100

6.33 Plots of Jacobian and equivalent stress for tungsten long-rod penetrator using erosion algorithm *none* to penetrate into sandstone without a steel liner. 101

6.34 Plots of Jacobian (left) and equivalent stress (right) for tungsten long-rod penetrator using erosion algorithm *ZeroStress* to penetrate into sandstone without a steel liner. 101

6.35 Plots of Jacobian and equivalent stress for a tungsten discrete jet penetrator having a constant velocity and using erosion algorithm *none* to penetrate into sandstone without a steel liner. 102

6.36 Plots of Jacobian and equivalent stress for a tungsten discrete jet penetrator having a constant velocity and using erosion algorithm *ZeroStress* to penetrate into sandstone without a steel liner. 102

7.1 Comparison of different glyphs used to visualize particle data. 107

7.2 Comparison of different glyphs used to visualize particle data. 108

7.3 Example video frame generated using automated visualization methods. 109

7.4 Example depth of penetration plots generated using automated visualization methods. 110

7.5 Example rate of penetration plots generated using automated visualization methods. 111

7.6 Example penetrator total kinetic energy plots generated using automated visualization methods. 112

7.7 Example penetrator segment total kinetic energy plots generated using automated visualization methods. 113
7.8 Example penetration histories of individual penetrator particles. 114
7.9 Example frame from an animated history of particle velocity, acceleration, and position. 115

LIST OF TABLES

5.1 Target and equilibrium times for simulations with confinement. 42

5.2 Simulation results investigating the effects of patching and number of processors on runtime. 44

5.3 Penetrator properties and resulting depth of penetration used to investigate the combined effects of rod density and length. 54

5.4 Anisotropic confinement used to obtain the results of Fig. 5.21. 60

5.5 Depth of penetration results from simulations of a tungsten rod using different erosion options to penetrate a target with and without fluid effects at differing levels of confinement. 61

6.1 Shear locking problem interpolators. 70

6.2 Material properties for volumetric locking test. 74

6.3 Convergence rates for 2-d volumetric locking problem varying Poisson's ratio by means of the bulk modulus. 75

6.4 Convergence rates for 2-d volumetric locking problem varying Poisson's ratio by means of the shear modulus. 77

6.5 Comparing erosion algorithm effects on depth of penetration, for tungsten into a steel billet. 95

6.6 Comparing erosion algorithm effects on the dimensionless penalty parameter, for tungsten into a steel billet. 96

6.7 comparing erosion algorithm effects on the dimensionless segmentation parameter, for tungsten into a steel billet. 96

6.8 Comparing erosion algorithm effects on depth of penetration, for tungsten into sandstone. 99

CHAPTER 1

INTRODUCTION

In the late 1800's it was discovered almost in unison by German engineer Max von Foerster and America Professor Charles E. Munroe that the force of an explosive device can be focused through incorporation of a hollow cavity into the devices design [1, 2]. This effect was later termed the *Munroe, Neumann, von Foerster* or *shaped-charge effect* [3]. Nearly forty years later Dr. Henry Mohaupt of Switzerland would discover that by lining this hollow cavity with material, a charge's ability to defeat a target could be significantly improved [4]. Most commonly associated with weapons of war (the bazooka, rocket propelled grenade, and torpedo), the shaped charge sees a great deal of use in other applications. For instance, shaped charges are used in cutting, demolition, geophysical prospecting, mining, hypervelocity impact studies, and prevalently in the petroleum industry during the *completions* process for *well-bore perforation* and reservoir stimulation, which is the subject of this research (a shaped charge and the completions process are demonstrated in Fig. 1.1). In fact, the petroleum industry uses more shaped charges per year than any other industry (including the defense industry) [5, 2].

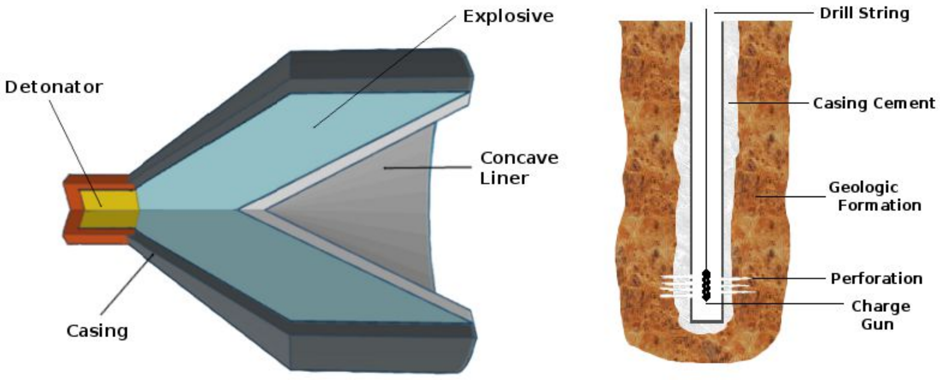

(a) (b)

Figure 1.1: Illustrations of (a) a shaped charge, and (b) the well-bore completions process.

After a wellbore has been drilled into a geologic formation, it is typically *cased*, wherein a steel liner is cemented in place along its length. This liner acts both to stabilize the wellbore and to provide a clean and consistent means of product transmission to the surface. In order to re-establish contact with the geologic reservoir after casing, a "carrier-tube" or "charge-gun" is loaded with multiple shaped charges and lowered downhole. As illustrated in Fig. 1.1, charges of this device are oriented so that they face radially outward. The extremely high pressures of the detonation front act to invert a conical liner, forming an elongated hypervelocity jet (velocities of 2-10 km/s are common), which acts to perforate the casing and subsequently penetrate deep into the surrounding formation. Shaped charges are also used in the absence of a liner to stimulate oil and natural gas recovery, which Walters [2] points out is an important goal as drilling costs roughly one million dollars per mile drilled. The task of shaped-charge design for use in completion tasks presents a considerable challenge because of the limited usable space available within a wellbore, the hostile downhole conditions, interplay of multiple charges detonating simultaneously, and the need to control debris along with formation damage.

1.1 Motivation

Many analytical and experimental models exist to predict the penetrative characteristics of a shaped charge [6, 7]. Some of these models have seen widespread use and can successfully predict the penetration of metal jets into metal targets after sufficient experimental calibration of material properties. For tractability, these models rely on simplifying assumptions (strength and viscous effects are ignored, constant velocity and radius jet, steady state penetration, no rate effects, etc.), which should preclude their use in predicting shaped charge penetration into geologic targets. While models having less restrictive assumptions do exist, they are often difficult to solve as a result of the nonlinear nature of the governing equations. Where solutions do exist, such as in the case of the Alekseevski-Tate equations [8, 9], exact solutions were first found as an implicit function of time [10], failing to provide explicit functional dependence of the penetration event on material properties [11]. Explicit solution of these equations exist [10], but as a result of involved mathematical acrobatics the importance of different prameters is not clearly evident [12]. Further, many of these models fail to provide predictions of the resulting cavity dimensions, its growth, or the effects of penetration on the surrounding material properties (especially permeability). Each of which are important, insomuch as they ultimately affect the flow properties of a completed well and the ability to better design new shaped charges.

In the past thirty years the Finite Element Method (FEM) and more recently the Material Point Method (MPM) have been employed successfully to model complicated dynamic phenomena not easily presenting themselves to analytical solution, such as the above problem of wellbore perforation/penetration. To this end, Schlumberger contracted the University of Utah to research and develop a phenomenological geoplasticity model, herein referred to as Arenisca (which is Spanish for sandstone). Quoting from the Arenisca users manual [13],

> Arenisca is a two-surface plasticity model combining a linear Drucker-Prager pressure- dependent strength (to model influence of friction at microscale sliding surfaces) and a cap yield function (to model influence of microscale porosity). The latter cap part reflects the fact that plastic deformations can occur even under purely hydrostatic compression as a consequence of void collapse. This model uses a multi-stage return algorithm published in [14].

This material model is currently being developed using the Uintah research code framework, which the Uintah manual [15] describes as "an environment for scientists to solve coupled multi-physics problems using modern parallel computing resources." This framework extensively makes use of the Material Point Method (MPM), originally developed at Sandia National Laboratories [16, 17]. MPM is an extension to the Particle-In-Cell (PIC) method using a mixed Eulerian-Lagrangian formulation which preserves the integrity of history-dependent internal state variables developed in each discrete material particle throughout a loading process, at the same time allowing massive deformations to develop without encountering the problem of mesh entanglement in its traditional form. By virtue of the MPM algorithm's nature, no-slip no-stick contact is free (assumed) between material particles sharing a computational cell, provided that the particles were initially separated by more than one grid cell. This property reduces the cost of multibody interactions such as impact events. More information on MPM and its implementation within Uintah is available in the following resources: [15, 18, 19, 20, 21, 22, 23, 24].

Development of Arenisca has been ongoing for four years, the aims of which are ultimately to improve the predictive capability of numerical models of well bore completion. To achieve this goal, a hierarchical approach to verification and validation (V&V) is employed [25], progressing through the following sequence of increasingly complicated simulations:

1. Numerous straightforward single-element verification tests, including confirmation of frame indifference [26].

2. Tests of code convergence behavior using the method of manufactured solutions [22, 27].

3. Calibration simulations (reproducing observed unconfined and confined uniaxial stress data for drained and undrained sandstone) [28, 29].
4. Partial validation of the host code for penetration of aluminum plates [30].
5. Development and testing of methods to establish appropriate initial and boundary conditions.
6. Ultimately, full-scale simulations of the entire well-bore completion process.

Most of these efforts are summarized in detailed annual reports for this project [28, 29, 31, 32]. The primary aim of this research has been to aid this endeavor through automation of V&V testing, development of novel and automated postprocessing techniques for visualization and decimation of simulation results, as well as comparisons between model predictions and currently available experimental results and theory during development.

1.2 Objectives

The present research focuses on the following areas and objectives:

- A review of current literature concerned with shape charge penetration, with special attention paid to models and results involving penetration of tungsten-lined shaped-charge jets into sandstone and similar targets where available.
- The automation of currently existing V&V tests in order to ensure code confidence as it is rapidly developed.
- Improvement of current single element (constitutive model) V&V testing methods. Extension of current capabilities to use existing simulation results as part of the design and test loop.
- Improvement and automation of current post processing techniques to increase both the fidelity and information content of visualizations.
- Development of new data decimation methods as necessitated by the large amounts of data (10-100 GB) produced by a single simulation.
- Execution of a large number of simulations meant to serve as qualitative validation in comparison against available experimental data and analytical theory.
- Investigation of unexpected results, their cause, and proposed resolution as such results emerge.

CHAPTER 2

DEFINITIONS AND TERMINOLOGY

Throughout this document, a clear and consistent notation is used to differentiate between tensors of different rank. The use of an under-tilde will explicitly denote the rank of a tensor. A scalar is a tensor of rank zero and so will have no under-tilde. A vector is a first rank tensor and so has two. The typical second-order tensor will have two under-tildes and so on. For instance: P is a scalar measure of penetration depth, $\underset{\sim}{\mathbf{V}}$ is a materials velocity vector at a point, and $\underset{\approx}{\mathbf{F}}$ is the deformation gradient tensor at a point.

2.1 Verification & Validation Testing

The American Society of Mechanical Engineers (ASME) recently published a guide on V&V practices in the field of computational solid mechanics, and has defined verifcation and validation as follows [33],

- Verification: The process of determining that a computational model accurately represents the underlying mathematical model and its solution.
  - Code Verification: establishing confidence, through the collection of evidence, that the mathematical model and solution algorithms are working correctly.
  - Calculation Verification: establishing confidence, through the collection of evidence, that the discrete solution of the mathematical model is accurate.
- Validation: The process of determining the degree to which a model is an accurate representation of the real world from the perspective of the intended uses of the model.
  - Validation Experiments: The process of determining that a computational model accurately represents the underlying mathematical model and its solution.

- Accuracy Assesment: The process of determining the degree to which a model is an accurate representation of the real world from the perspective of the intended uses of the model.

This definition will be used in refering to the principles of V&V throughout the body of this text.

2.2 Stress Tensor

Throughout this document in referring to stress $\underset{\approx}{\sigma}$, the cauchy stress tensor is meant. This measure of stress is a real valued, second-rank, symmetric tensor defining the stress state at a point inside a material in the spatial (deformed) configuration [34]. Caucy stress when dotted with a unit vector perpandicular to a plane ($\underset{\sim}{\mathbf{n}}$), returns the the stress in the direction of that vector acting across the plane ($\underset{\sim}{\mathbf{T}}$).

$$\underset{\sim}{\mathbf{T}} = \underset{\sim}{\mathbf{n}} \cdot \underset{\approx}{\sigma} \tag{2.1}$$

This property of the Cauchy stress tensor is not universally true of all stress measures. A real symmetric second-rank tensor such $\underset{\approx}{\sigma}$ can have up to three independant invariants. On occasion a memeber of the following specific subset of invariants, the "mechanics invariant triplet" [35] will be referred to.

$$I_1 = tr(\underset{\approx}{\sigma}) \tag{2.2}$$

$$J_2 = \frac{1}{2}\mathrm{tr}\left[\left(\underset{\approx}{\sigma} - \frac{1}{3}tr(\underset{\approx}{\sigma})\underset{\approx}{\mathbf{I}}\right)^2\right] \tag{2.3}$$

$$J_3 = \frac{1}{3}\mathrm{tr}\left[\left(\underset{\approx}{\sigma} - \frac{1}{3}tr(\underset{\approx}{\sigma})\underset{\approx}{\mathbf{I}}\right)^3\right] \tag{2.4}$$

The invariant I_1 acts to measure the magnitude of the isotropic portion of a stress state, while J_2 and J_3 measure the deviatoric (shear) component. Pressure, P, then is defined in terms of I_1 as

$$P = \frac{-I_1}{3} \tag{2.5}$$

2.3 Strain Tensor

The constitutive model belongs to the general framework of small-elastic-strain platicity theories [36] for which the symmetric part of the velocity gradient $\underset{\approx}{\mathbf{D}}$ is treated as an approximation to the Hencky (logarithmic) strain rate. To satisfy the principle of material frame indifference, the model accommodates large rotations by working in the so-called "unrotated" frame so that the constitutive model is called with the approximation of strain rate being set as

$$\underset{\approx}{\bar{\mathbf{D}}} = \underset{\approx}{\mathbf{R}}^{T} \cdot \underset{\approx}{\mathbf{D}} \cdot \underset{\approx}{\mathbf{R}} \tag{2.6}$$

in which $\underset{\approx}{\mathbf{R}}$ is the rotation from the polar decomposition of the deformation gradient $\underset{\approx}{\mathbf{F}}$ as $\underset{\approx}{\mathbf{F}} = \underset{\approx}{\mathbf{R}} \cdot \underset{\approx}{\mathbf{U}}$, where the right-stretch tensor $\underset{\approx}{\mathbf{U}}$ is symmetric and positive definite (*c.f.* [37]). The strain rate $\underset{\approx}{\dot{\epsilon}}$ appearing later in the constitutive model is, in the numerical implementation, actually given by $\underset{\approx}{\dot{\epsilon}} \approx \underset{\approx}{\bar{\mathbf{D}}}$. This approximation is exact if the principal directions of the right-stretch tensor $\underset{\approx}{\mathbf{U}}$ do not rotate (which is not the case in penetration) and it is a very good approximation if strains are small (which is presumed to be the case for sandstone penetration since the material is expected to fail at small strains).

CHAPTER 3

LITERATURE REVIEW

A wealth of algebraic models exist to predict penetration depth, and in some instances, other attributes of a penetration process. The majority of these models are best suited to metal-on-metal penetration, as they are based on the Bernoulli principle for incompressible hydrodynamic flows and might therefore fail to be predictive for porous quasibrittle media like sandstone. The purpose of this section is to review and outline such models for use later in validating simulation results. Further, following a discussion of penetration models relevant and seminal works pertaining to MPM, the development of Arenisca, and simulation of penetration phenomena within this framework will be briefly reviewed.

3.1 Penetration Models

Penetration phenomena as driven by explosively formed penetrators, or by other means, have been studied for some time now. As a result, a large amount of literature on the subject exists. The following is not a comprehensive review of all the models and theory in existence, but instead meant as a review of those models which might be useful in early validation of a numerical scheme meant to be predictive of the aforementioned phenomena. Walters *et al.* [6] on the other hand did conduct such an extensive survey of penetration models, from their infancy, to the late 1980s. Walters also provides an overview of the shaped charge concept in [2] and [38].

The first of the basic 1-d analytical penetration models was developed by Birkoff *et al.* [3], who assumed that the pressures produced during penetration significantly exceed the yield strength of either the jet or target and therefore they neglect strength and viscous effects by treating the jet as incompressible and inviscid (*hydrodynamic*). For steady-state penetration occurring at velocity U into a semi-infinite target of density ρ_t, driven by a penetrating jet of length L, density ρ_p, and velocity V, using a frame of reference that is fixed at the forefront of penetration as illustrated in Fig. 3.1 allows application of Bernoulli's principal to equate pressures in the target and jet at their interface resulting in

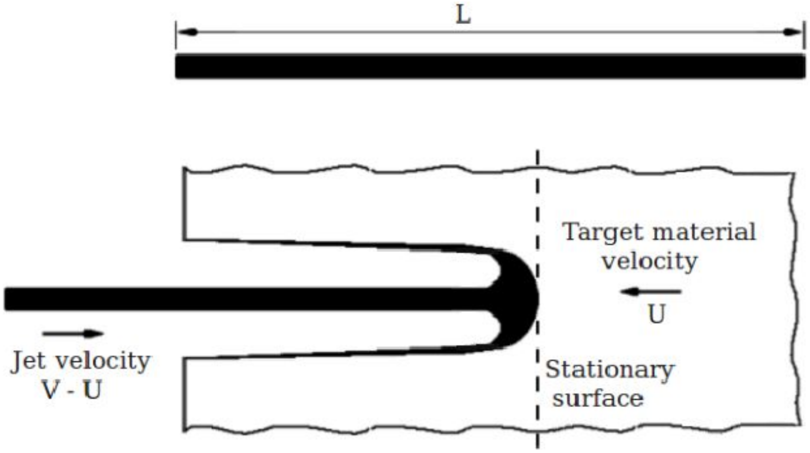

Figure 3.1: Birkoff Bernoulli penetration.

$$\frac{1}{2}\rho_p(V-U)^2 = \frac{1}{2}\rho_t U^2 \tag{3.1}$$

which assuming that penetration ceases once the jet is consumed (*i.e.,* once the last jet/penetrator particle strikes the target) produces a total penetration depth of P, found by the penetration velocity times the duration of penetration.

$$P = U\frac{L}{V-U} = L\sqrt{\frac{\rho_p}{\rho_t}} \tag{3.2}$$

A simple modification was made to this theory by Birkoff to account for the particulation/breakup of real jets:

$$\lambda\rho_{\text{avg}}(V-U)^2 = \rho_t U^2 \tag{3.3}$$

where λ is a measure of jet particulation ranging from 1 for a continuous jet to 2 for a fully particulated jet, and ρ_{avg} is the average jet density, defined to be the mass of the jet divided by the volume of its convex hull. This formulation then has the ability to represent penetration by jets at intermediate stages of particulation producing a penetration depth of

$$P = L\sqrt{\frac{\lambda\rho_{\text{avg}}}{\rho_t}} \tag{3.4}$$

Despite failure to incorporate the physical effects of material strength, strain, and strain-rate dependence in determining penetration depth, as well as being unable to account explicitly for the spatially varying nature of actual shaped charge jets, the Birkoff model frequently sees use as a first approximation, and (arguably) even theoretical limit, because of the reduced importance of these effects with increasing impact velocities [6].

Later work by Pack and Evans [39] built on this foundation to incorporate target strength and secondary penetration effects. Pack suggested that target strength could be accounted for by comparing pressure at the penetration front and the target's yield strength. Doing so resulted in the nondimensional quantity $\sigma_y/\rho_p V^2$, a factor of which was used to penalize Birkoff's penetration depth (Eqn. 3.4). To account for afterflow, Pack reasoned that secondary penetration is the result of continued plastic flow in the target material, similar to that observed laterally in a soft target, reaching the conclusion that secondary penetration depth should be approximately equal to the radius of the cavity. Total penetration then is the combination of these two effects, given by

$$P = L\sqrt{\frac{\lambda\rho_p}{\rho_t}}\left(1 - \frac{\alpha\sigma_y}{\rho_p V^2}\right) + r \tag{3.5}$$

where r is the radius of the penetration channel, and α is understood to be a function of the jet and target densities.

Eichelberger [40] a contemporary of Birkoff, Pack, and Evans, after establishing a means to measure penetration through time, postulated the virtual origin concept, proposed an alternative interpretation of λ, and devised a new method to incorporate strength effects. Using penetration through time measurements, he determined that the particulated velocity varies affinely over the length of the jet, and therefore the impacting particle velocity varies through time. For an affine velocity profile, the virtual origin is defined to be the location in space all jet particles appear to originate from. Using this relationship he posits that λ can be used as a statistical factor to capture jet variance such as changes in mode of transfer of momentum (dependent on particle size, shape, and velocity), particulation of the jet (dependent on standoff, velocity gradient, strength, and ductility of the jet), and variance in the material properties of the charge and liner. Motivated by experimental results, Eichelberger also modifies Eqn. 3.4 to incorporate strength effects in the following way:

$$\lambda\rho_p(V-U)^2 = \rho_t U^2 + 2\sigma \tag{3.6}$$

where σ in the above equation represents the difference in dynamic resistance to plastic deformation between the target (R) and jet (Y) materials

$$\sigma = R - Y \tag{3.7}$$

The strength terms R and Y were found to be one to three times the quasistatic uniaxial yield stress for metals, attributed to the combined effects of the strain-rate and nonunixiallity of the stress state. The above governing equation leads to the following depth of penetration:

$$P = L\sqrt{\frac{\lambda\rho_p}{\rho_t} - \frac{2\sigma}{\rho_t(V-U)^2}} \tag{3.8}$$

Note two important aspects of incorporating strength in this way, one strength effects dominate as V approaches the steady state penetration velocity U, and two that jet/penetrator and target strength work to offset one another [41]. Further notice that Eichelberger's penetration depth can be reduced to that of Birkoff (3.4) in like material penetration ($R - Y = 0$) or situations where $\rho_t(V-U)^2 = 2(R-Y)$ suggesting the potential for optimization through materials and penetrator velocity selection. Eichelberger concludes his theory with an alternative understanding of residual penetration, remarking that Packs' definition is limited to jets traveling overall at very high velocities and which terminate abruptly, which would only account for five percent of the observed residual penetration in his experiments. Instead Eichelberger interprets residual penetration to result from the slower moving tail portion of the jet being able to defeat target materials having a low dynamic strength, as the impact pressures generated by this portion of the jet are similarly low. This understanding is supported by the remarkably increased penetration (40%) in lead versus that into aluminum or steel using the same shaped charge jet.

Independently, Alekseevskii [8] and Tate [9] developed a modified version of the Bernoulli equation taking into account dynamic strength effects similar in nature to Eichelberger's formulation:

$$Y + \frac{1}{2}\rho_p(V-U)^2 = \frac{1}{2}\rho_t U^2 + R \tag{3.9}$$

where R is the target's resistance to penetration frequently taken as the Vickers hardness, and Y is the 'dynamic yield point' of the penetrator. The Alekseevskii-Tate equations have become the standard representation of long-rod penetration into semi-infinite targets [42].

While these equations account for strength of both the target and penetrator, this model suffers from making the assumption that at the interface both the target and penetrator behave as incompressible inviscid fluids, failing to account for the onset and termination of this behavior where quasistatic strength dominates. Further the Alekseevskii-Tate model involves solution of a differential system, often requiring somewhat involved mathematical acrobatics and frequently numerical solution methods [43]. An exact solution exists as obtained by Walters and Segletes [10], which Segletes admits fails to provide any insight into the underlying mechanics involved and is in practice difficult to use [12].

Gladkikh *et al.* [7] describe a simple penetration equation, based on integration of the Birkhoff-Bernoulli model (Eqn. 3.1) to account for jets having a linear velocity gradient. This model assumes the velocity gradient acts to stretch the jet axially as it contracts radially in a proportional manner, while maintaining a constant density, arriving at penetration depth represented by the density ratio $\gamma = \sqrt{\frac{\rho_p}{\rho_t}}$, and ratio of the tip ($V_{\text{tip}}$) tail ($V_{\text{tail}}$) velocities $R = V_{\text{tip}}/V_{\text{tail}}$. The assumption of a constant density jet results in an infinitesimally thin jet tip which is nonphysical and is reported to overpredict depth of penetration. Therefore the model was reformulated to assume a constant diameter jet having a time/spatial density variation subject to conservation of mass, which produce a penetration depth of

$$P = L\gamma \left[\frac{(2+\gamma)\Gamma - 2(1+\gamma)\sqrt{\Gamma} + \gamma}{\Gamma - 1} \right] \tag{3.10}$$

Gladkikh reports this to provide a more reasonable penetration prediction given the underlying assumptions [7]. Still this model suffers from failure to incorporate strength effects or compressibility and breaks down for jets having a small/nonexistent velocity gradient.

A number of authors have approached the problem of particulation/segmentation of shaped-charge jets [44, 45, 46], but either as a result of the current discretization used to describe the jet [30] , or the assumption that incremental jet segments penetrate at the same rate regardless of their spacing – which has been repeatedly and compellingly been disputed in the literature [47, 48, 49] – they will not be reviewed presently. More recently, Grove [41], building on the work of Flis and Crilly [50], developed a model to account for a particulated jets compressibility. This is important as Grove reports that typical oil well perforators use a pressed powder metal liner to prevent large solid debris, in the form of slugs, from clogging the penetration channel. The jets formed by such liners exhibit no tensile strength, and in stretching distend to very low densities, which according to Grove calls into question analysis based on solid incompressible theory, such as those of Birkoff, Pack and Evans, and Eichelberger. Grove then describes penetration as a two-step process using a sequence of shock compaction of the distended jet to its pore-free density, and following this process, the compacted jet then penetrates according to incompressible Bernoulli theory like that of Eichelberger. This viewpoint results in a pressure within the target given by

$$R + \frac{1}{2}\rho_t U^2 \tag{3.11}$$

Next, the Rankine-Hugonoit shock-jump conservation equations are used to arrive at the pressure in the jet given by

$$Y + \frac{1}{2}\rho_d (V - U)^2 (1 + \phi) \tag{3.12}$$

where $\phi = 1 - \rho_d/\rho_s$ is jet porosity, representing the difference between the distended (porous) jet density prior to impact ρ_d and its initially solid (pore-free) density ρ_s. Equating pressure in the target (Eqn. 3.11) and jet (Eqn. 3.12) and solving for depth of penetration results in

$$P = L\sqrt{\frac{\rho_d}{\rho t}(1 + \phi) - \frac{2\sigma}{\rho_t (V - U)^2}} \tag{3.13}$$

which, for hydrodynamic penetration, reduces to the Birkoff model where $\lambda = 1 + \phi$. Grove concludes by warning that nonsteady effects are likely significant in a noncontinuous jet, precluding application of any continuum steady-state treatment, including his own.

Other authors ([51, 52, 5]) have made attempts to predict the development of 2-d penetration channels but frequently suffer the same shortcomings as all the above models in that they also are primarily applicable to hydrodynamic (incompressible and inviscid and frequently strengthless) penetration of constant velocity penetrators, require extensive experimentation to be calibrated, and/or are only applicable to specific material types.

When used to predict penetration of geomaterials (such as sandstone) by an explosively formed penetrator, the above models are in practice overly simplistic and fail to provide accurate predictions for depth of penetration [7]. This result can likely be attributed to a failure to account for compressibility, strength effects, rate effects, and failure modes, which are thought to play critical roles in the hypervelocity response of such materials [53]. The problems of inaccuracy are further compounded by an inability to predict the damage that results in the surrounding formation and accompanying changes in permeability (70-90%), which together result in significant productivity losses [54]. Together these problems have prevented widespread use of such models in the design of shaped charges for wellbore perforation jobs.

Alternatively, the oil services industry widely uses experimental correlations to predict the performance of explosively formed penetrators [7, 55]. Many of these proprietary models are based on experimental data obtained from penetration into unstressed concrete targets, and as a result, are not accurate predictors of a charges performance under downhole conditions [56, 55]. Further there is considerable discrepancy between models, which in some instances predict nearly double the penetration into the same target, for the same conditions, using the same calibrating data [55].

Despite what can be wildy different predictions concerning penetration depth these models all incorporate the following correlations in some form or another as reported by Behrmann *et al.* [55] and Harvey *et al.* [57]:

1. API Section I test penetration ⇒ Penetration of Berea sandstone unconfined compressive strength of 7 ksi
2. Berea penetration ⇒ different strength rock (strength effect)
3. Unstressed rock ⇒ Stressed rock (influence of effective stress)
4. Effects of cement, casing, and wellbore fluid, etc.

Harvey attributes this to the factors of economics (its expensive to quarry rock), consistency (assumption that concrete targets will be inherently more consistent than real rock targets), and the assumption that optimization of a charges performance into concrete results in a corresponding increase in performance under downhole conditions. Further, both Behrmann and Harvey come to the conclusion that this method suffers from the following shortcomings: use of old lab data and fits, assumption of a monotonic concrete-sandstone relationship, and the effects of changing API Section I concrete targets from RP 43 to RP 19B in 2006 (which have been shown to be more difficult to penetrate).

Grove *et al.* [58] initially suggest a more predictive model in the form of an exponential correlation. They also introduce the *ballistic pore pressure coefficient*, a, which they claim is an intrinsic rock property. The pore pressure coefficient decreases with increasing rock strength, acting to decrease the penetration depth in stronger rocks by means of pore pressure. This coefficient ranges from 0 to 1, and for Berea sandstone is reported to be limited to a range of 0.5 – 0.7. Harvey *et al.* [57] build on the work of Grove *et al.* to develop a correlation in the form of a polynomial fit to material and penetration data (dependent on thirteen fitting parameters in total), which despite being unwieldy to use, is able to predict data across multiple rocks, at multiple stress levels, using multiple charges, with an average error of only 8% [57]. Harvey *et al.* later revise this model to an exponential formulation [59] based on the work of Thompson [60], which results in predicted penetration depth taking the following exponential form in US Imperial units

$$P = P_{\text{ref}} \exp(\alpha_0(10000 - F_{\text{BI}})) \tag{3.14}$$

$$F_{BI} = \sigma_{\text{ucs}} + bP_{\text{eff}} \tag{3.15}$$

$$P_{eff} = P_{\text{c}} = aP_{\text{p}} \tag{3.16}$$

$$a\left(\phi\right) = 0.0967\phi^{0.428} \tag{3.17}$$

$$b\left(\sigma_{\text{ucs}}\right) = \begin{cases} 0.7336 - 1.813x10^{-5}\sigma_{\text{ucs}} & \sigma_{\text{ucs}} < 30000 \text{ (psi)} \\ 3.33\exp(-9.55x10^{-5}\sigma_{\text{ucs}}) & \sigma_{\text{ucs}} \geq 30000 \text{ (psi)} \end{cases} \tag{3.18}$$

Where F_{BI} is the so called *ballistic indicator function* of a formation having units of pressure, and P_{ref} is the reference penetration depth for a formation having a ballistic indicator function equal to 10000 psi, α_0 is the charge coefficient, σ_{ucs} is the unconfined compressive strength of the formation, b is the stress influence coefficient, P_{eff} is the effective stress which accounts for fluid pressure, P_{p} is the fluid pressure, P_{c} is the confining stress or overburden, a is the ballistic pore pressure coefficient, and ϕ is the material porosity in percent ranging from 0 to 100. Harvey *et al.* demonstrate this model to be significantly more accurate at predicting depth of penetration under downhole conditions. Despite this success, use of this correlation requires a minimum of twelve calibrating experiments for each new charge, makes the assumption of isotropic confining stress (which is rarely the case [61]), and does not resolve temporal behavior or resulting channel geometry. Further, to account for differences in formation lithography, pore fluid, casing material, and casing cement, would require added experimentation which is expensive and time consuming. For the above reasons, and the relative shortcoming of both analytical formulations and predictive correlations, work has focused on predictively simulating the dynamic process of hypervelocity penetration.

3.2 Simulating Penetration

Many numerical solution schemes for penetration problems exist. In particular, two promising particle methods are the smoothed particle method (SPH) and the material point method (MPM). Ma *et al.* [62] compared MPM against SPH and came to the conclusion that MPM has many advantages over SPH. MPM is simpler than SPH and its formulation is similar to tradition FEM, MPM does not require particle neighbor searching at each step, does not suffer from the tensile instability that SPH does, boundary conditions are easily implemented in MPM, and no-slip contact is free/assumed.

MPM is an arbitrary Eulerian-Lagrangian method whereby the solution is obtained using discretization of the domain by an arbitrary Eulerian background grid. The governing momentum equations are solved on this grid, and frequently to avoid mesh entanglement problems, deformation of this background grid is discarded at each timestep. When implemented this way (as is done in Uintah) MPM is particularly well suited to problems involving massive deformations, such as the problem of shaped charge jet formation and penetration. Materials within the domain are further discretized to Lagrangian material points, which contain material state data and deformation histories. These particle are used by the background grid as points of integration, in fact if deformations are sufficiently small MPM can be reduced to traditional FEM, where the particles become Gauss integration points.

Development of the material model Arenisca is currently being done within the MPM research code Uintah [19, 15]. Previously Burghardt *et al.* [30] demonstrated that Uintah is capable of representing the penetration phenomena of metals. This was done using a simplified representation of a shaped charge jet. The intent of Arenisca is to extend this work to the penetration of geomaterials, and eventually, use as a design aid in the development of shaped charges. The development of Arenisca has has been similar in nature to that of the plasticity code Kayenta. Kayenta was originally developed as a geomaterials model at Sandia National Labs [35] and has since grown to incorporate the features of many other materials. Both models use a composite yield surface formed by a linear Drucker-Prager surface with a curved cap, the likes of which is frequently used to numerically model geomaterials [63]. Both support nonlinear elasticity to account for fluid filled porosity, support softening to account for weakening in dilatation, and multiple forms of hardening to account for strengthening during pore collapse as well as the microscale frictional effects accounting for shear dependent strength. Arenisca's development was motivated by the need for a phenomenologically based geomaterials plasticity model that was unencumbered by the restrictive licensing agreements of a national lab.

Progress to date for the Arenisca material model is summarized in project reports,[28, 29, 31, 28]. and the development manual [13]. Arenisca further, has the ability to reduce to a von Mises plasticity surface. This is a beneficial feature as it can simplify V&V testing, givent that von Mises plasticity solutions more readily lend themselves to analytical solution resulting in a number of such problems existing to verify both the material model and its implementation within a given host code. [14, 64, 27, 22]. Many of these tests may appear simple, but it is often such simple tests that reveal the most fundemental algorithmic implementation errors [26], stressing the need to formalize such testsing in the continued development of any numerical constitutive model. Though it is desired to perform a verification of Arenisca's full history dependent plasticity algorithms, there exist few such tests, making development of such testing an active research area having considerable impact potential.

Following basic verification testing, systematic validation should be performed. Numerical solution methods frequently lend themselves to a bottom up approach, whereby features can be tested addatively. Using this method allows the employ of the previously reviewed analytical solutions, which in practice elsewhere have only limitied applicability. After this, full model validation can be performed in comparing numerical results against experimental data sets. This leads to greater confidence in the model and extension of use to domains outside those tested.

3.3 Summary

While a variety of analytical penetration models exist, as a result of the simplifying assumptions made in their formulation, they fail to accurately predict the penetration of geomaterials. This failure can be attributed to neglecting the effects of compressibility, material strength, strain rate, stress state triaxiality, and material failure modes, all of which are thought to play important roles in the impact loading response of such materials. These same models further fail to predict material damage, which can have a significant impact of the resulting productivity of a completed well. Recently, new experimental correlations have been developed, which are more accurate, but also fail to provide fundemental insights in the penetration process, or its effects on surrounding rock properties.

To both solve the problem of not being predictive of the resulting penetration cavities properties as well as to better understand the more subtle effects that a penetration process can have on a surrounding formation's flow properties, physically motivated numerical solution schemes have been employed. Doing this requires both a suitable framework and the development of an appropriate constitutive model, which captures the nuanced response of geomaterials to a variety of loadings.

To this end, the Uintah MPM framework was selected, and the Arenisca material model developed. Verification and validation practices are important during such an undertaking. The selected form of V&V used is that of a ground up approach, which requires the use/development of relatively simple verification tests to substantiate the model in a reduced form. Following such tests, the model can then be validated against analytical theory using simulations tailored to the limitations of each theory. Lastly, the model in full form, should then be validated against experimental data sets. This approach serves to highlight shortcomings in the model and/or its implementation early during development, thereby preventing the unescessary wasting of human and computational resources, ultimately providing more accurate and insightful results, and the extension to domains outside of those which have been adeqautely tested with a certain level of confidence.

CHAPTER 4

BUILDING MODEL CONFIDENCE THROUGH V&V PRACTICES

Code verification will be the primary focus of this chapter with calculation verification (primarily convergence analysis) being discussed in Chapter 5. The inputs to the material model are input strain, strain rate, and an element's associated internal state variables (ISVs). The outputs are the updated stress state and updated ISVs. Accordingly, prescribed-deformation single-element tests are the most appropriate method of constitutive model verification. Inherent to this method are the laborious and even intractable solutions that arise in trying to solve analytically, tortuous deformation histories, using the full features of a complicated plasticity code such as Arenisca. For this reason relatively few such tests exist, making this an active research area. Tests that do exist often apply simplifying constraints (reduction to a simpler model such as J_2 plasticity, solution in the principle basis, nonhardening/softening, etc.), or are merely qualitative verification, acting to confirm that the expected trends are reproduced under certain loading conditions (reduction in porosity, hardening effects, fluid effects, etc.).

4.1 Automation of Current Verification Tests

Many verification tests were developed concurrently with Arenisca [31], and are specific to model features; these tests are documented in the Arenisca developers manual [13] and in the open literature [26, 14]. Despite this accomplishment, such tests have not seen regular use by model developers as a result of the inconvenience and time-consuming process of having to manually execute and postprocess them. Some consequences of neglecting verification are errors in the algorithm, implementation, and/or theory being carried forward in each successive version of the model. To resolve this problem the benchmark tests above were incorporated into the currently available Uintah nightly regression tester as well as into an automated standalone verification suite. Making the verification process pain free and information rich in this manner has provided greater insight into the cause and subsequent resolution of errors. Because this test suite was done entirely in the open source Python programming language, it is operating-system independent. To see the Python code, refer to the Appendix. To follow is documentation of tests included in the aforementioned testing suite.

4.1.1 Single Element Verification Tests

4.1.1.1 Testing for frame indifference

According to Noll [65], the principle of material frame indifference is that *the constitutive laws governing the internal interactions of a system should not depend on whatever external frame of reference is used to describe them.* Stated mathematically for an arbitrary time-dependent orthogonal rotation tensor $\underset{\approx}{\mathbf{Q}}(t)$, connecting two frames ϕ and ϕ^*, which themselves are used to describe the spatial scalar field $s(\phi)$, vector field $\underset{\sim}{\mathbf{u}}(\phi)$, and tensor field $\underset{\approx}{\mathbf{T}}(\phi)$, then these fields are said to be *frame indifferent* (observer indifferent, or objective) spatial fields if they satisfy the following relationships

$$
\begin{aligned}
s(\phi^*) &= s(\phi) \\
\underset{\sim}{\mathbf{u}}(\phi^*) &= \underset{\approx}{\mathbf{Q}}(t) \cdot \underset{\sim}{\mathbf{u}}(\phi) \qquad (4.1) \\
\underset{\approx}{\mathbf{T}}(\phi^*) &= \underset{\approx}{\mathbf{Q}}(t) \cdot \underset{\approx}{\mathbf{Q}}(\phi) \cdot \underset{\approx}{\mathbf{Q}}(t)^T
\end{aligned}
$$

A simple yet surprisingly effective test of material model frame indifference prescribes uniaxial strain with large superimposed rotations. In this test, a single material element is simultaneously pulled along a given reference axis while undergoing rigid rotation. At the end of the test, the material element has undergone a full 360° rotation. Such a test is illustrated in Fig. 4.1. To pass this test, the spatial Cauchy stress must rotate according to Eqn. 4.1, while the unrotated Cauchy stress ($\underset{\approx}{\bar{\sigma}} := \underset{\approx}{\mathbf{R}}^T \cdot \underset{\approx}{\sigma} \cdot \underset{\approx}{\mathbf{R}}$ in which $\underset{\approx}{\mathbf{R}}$ is the polar rotation) must not be affected.

This test has previously been shown [26] to reveal problems in a common approach to strong objectivity [66] as implemented in many finite element codes. In fact this test has repeatedly proven effective at catching errors in both Uintah and Arenisca [26, 31, 32], and is so simple it is recommended as a verification test before assigning any amount of confidence to a given solid mechanics code. The results of a successful test are presented below in Fig. 4.2. At 0.25, 0.50, 0.75, and 1.00 seconds into the test a successive rotation of 90° CCW has been completed with respect to the previous interval, this results in the primary

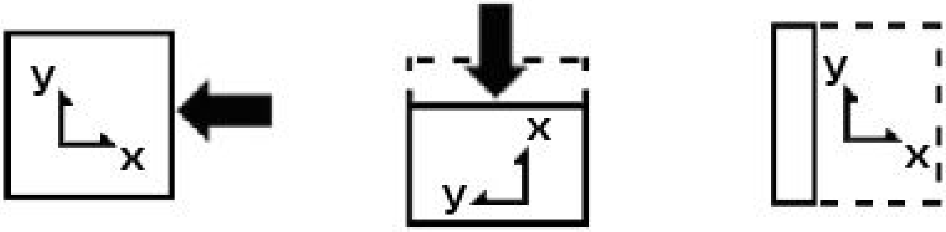

(a) (b) (c)

Figure 4.1: Illustration of basic frame-indifference test. (a) Stretching begins in the reference configuration; (b) while applying continued loading, the material element undergoes CCW rotation and, as shown, has undergone 90° of rotation and one quarter the total deformation; (c) the material element in its final state fully deformed and having gone through 360° of rotation returning to its original orientation.

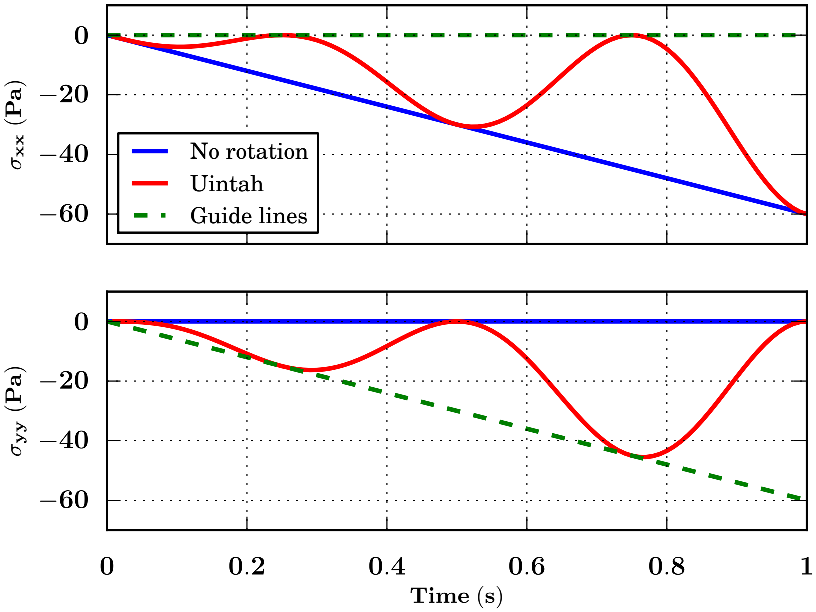

Figure 4.2: Frame indifference test results as produced using Arenisca's automated test suite. Solution without superimposed rotation in blue, with sequential rotation and then stretch in green, and spatial output from Uintah in red. At all times, the red solution line should lie between the green and blue lines.

components of stress in each instance trading place. Concurrently a small elastic uniaxial stretch – reaching a magnitude of $\lambda = 0.998$ – is applied in a primary direction of the reference configuration. The solution without superimposed rotation (reference solution) is indicated by the blue line, while the solution with sequential rotation and stretch (solution in final spatial configuration) is indicated by the green dashed line, the red line represents parallel application of the stretch and rotation (instantaneous spatial solution).

4.1.1.2 Model reduction to J_2 (von Mises) plasticity

Arenisca supports reduction to J_2 (von Mises) plasticity. Figure 4.3 illustrates the differences between the initial yield surface using a J_2 specification versus that of the combined linear Drucker-Prager with curved cap yield surface used to represent various geomaterials. The reduced form lends itself to analytical solutions use in single-element verification tests. Many of these tests for J_2 plasticity are uniaxial-strain tests. This loading mode is of interest in the field of shock physics as the fastest elastic wave to propagate in isotropic media (P-wave) and initially subjects the material to uniaxial-strain loading upon first passage through the material [64]. Uniaxial strain is also convenient because it is purely strain-driven, consistent with the nature of inputs of the constitutive model.

One such uniaxial-strain test is the Hugoniot uniaxial-strain shock test. Hugoniot according to Zukas *et al.* [67], refers to all stress states achievable under shock loading given known material properties and constitutive relationships. The objective of this test is to reproduce the results of Brannon [64], specifically the stress versus strain plots of Fig. 4.4. The axial stress state, when plotted against the axial strain, is expected to initially increase with a slope equal to the constrained modulus C. Upon reaching yield, the stress state then increases with a shallower slope equal to the bulk modulus K. After reaching the maximum strain, the load is released at the initial slope until yield is again reached, after which the slope is again the bulk modulus. The results of this test are presented as Fig. 4.5.

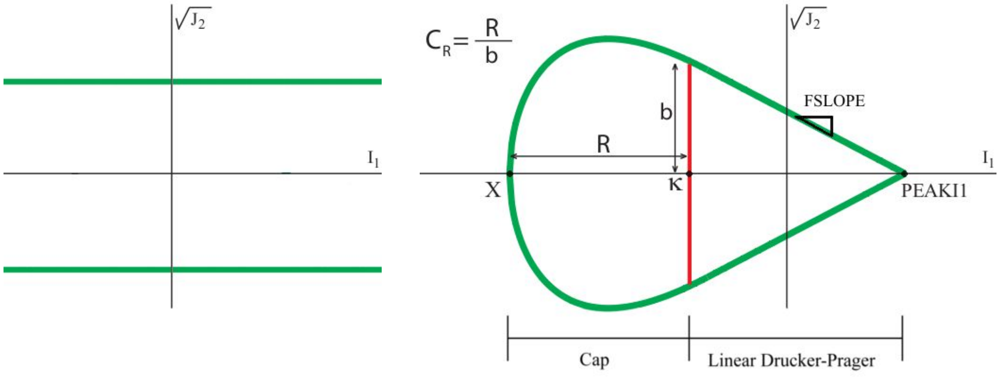

(a) von Mises (b) Arenisca

Figure 4.3: Comparison of von Mises and Arenisca yield surfaces in stress invariant space. The parameters defining Arenisca's yield surface consist of the tensile verticie for the linear Drucker-Prager portion ($PEAKI1$), the slope for this same region ($FLOPE$), transition to the cap portion (κ), the caps major and minor radii (R and b, respectively), thier eccentricity (C_r), and the compressive limit (X).

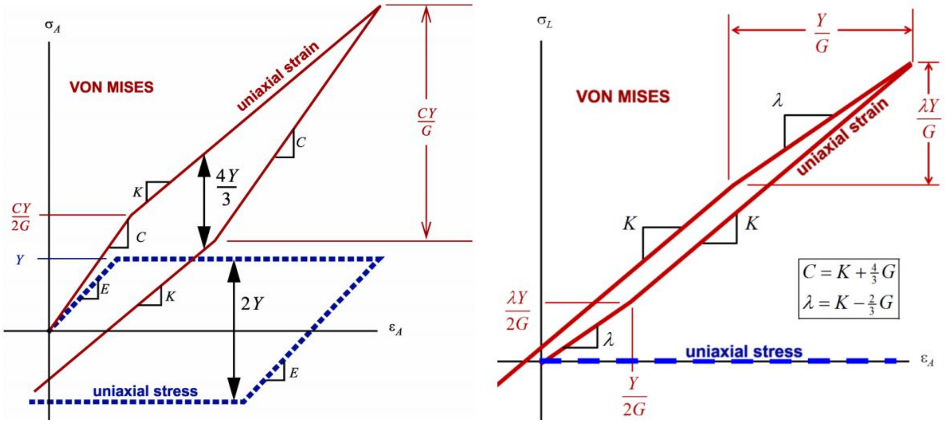

Figure 4.4: Comparison of uniaxial strain and uniaxial stress loading. Source – [64]

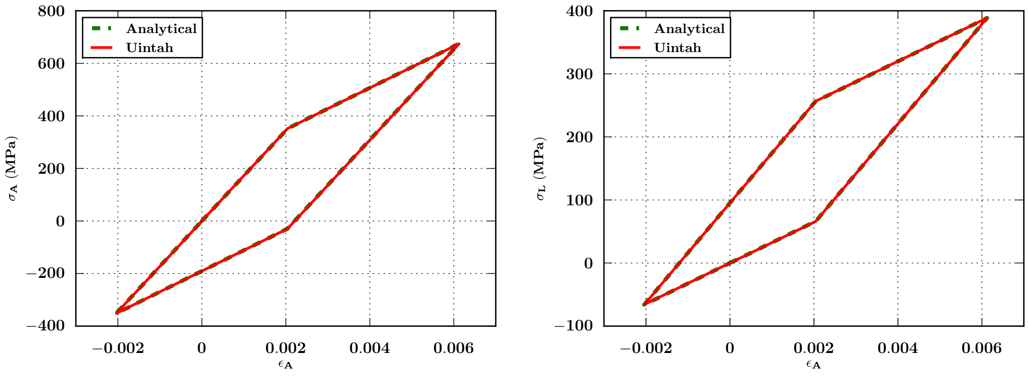

(a)

(b)

Figure 4.5: Results of uniaxial strain single element test. (a) and (b) correspond to the left and right sides of Fig. 4.4, respectively.

In reduced form a number of qualitative checks are performed on yield surface evolution in the forms of isotropic and kinematic hardening. Isotropic hardening is a form of hardening where a yield function that is initially isotropic – that is the function depends only on the invariants of stress – will remain isotropic. It is a common misconception that isotropic hardening results in uniform expansion of the yield surface for all plasticity models, this is a result of confusing the terms *isotropic function* and *isotropic mapping*, which is further compounded by isotropic hardening resulting in a uniform expansion of the von Mises cylinder in J_2 plasticity. Kinematic hardening fixes the size and shape of the yield surface while translating it in space by a backstress tesor ($\underset{\approx}{\alpha}$). For J_2 plasticity this corresponds to the von Mises cylinder moving up/down from the hydrostat. Three uniaxial-strain tests are used to verify the implementation of hardening, for each test Arenisca is reduced to von Mises plasticity. In the first test, both isotropic and kinematic hardening are disabled, for the second and third tests respectively isotropic and then kinematic hardening are independently enabled.

The results of each test are presented as a plot on the meridional profile. For simplified J_2 theory this is the side view of an infinite cylinder. The results for nonhardening (von Mises perfect plasticity), which are presented in Fig. 4.6, therefore correspond to the following phases of loading:

1. The stress state evolves elastically until it reaches the cylinder's surface as indicated by the dashed line.
2. The stress state moves tangentially along the cylinder surface under continuued plastic deformation.
3. The stress state is elastically unloaded, crosses the isomorphic pressure axis, and elastically loaded until it again reaches the cylinders surface.
4. The stress state moves tangentially along the cylinder surface under continuued plastic deformation as before.

A hardening response would instead result in the stress state upon reaching yield, continuing to evolve beyond the initial cylinder radius. For both isotropic and kinematic hardening as implemented in Arenisca this would initially take the same form. Upon reaching yield, continued loading would result in an increased stress state at a slope shallower than the initial elastic loading. Unloading occurs at the same slope as the initial elastic portion. The unloading leg is followed by an elastic loading leg in the opposite direction as before. For the case of isotropic hardening, yield is reached at a now increased radius as a result of the earlier isotropic expansion of the von Mises cylinder, and then continued loading further expands the cylinder. For the case of kinematic hardening, the second yielding is reached earlier, which is a result of the von Mises cylinder having translated along the initial loading trajectory in stress space. Both of these features were initially present within the Arenisca framework, but (as a result of other work) they have been temporarily removed. Consequently, these benchmarks are not currently passing. Results obtained using a previous version having these features are also presented in Fig. 4.6. It is expected these features will be added in the future, at which point these tests will serve as verification.

Another verification test recommended for material models supporting J_2 plasticity was formulated by Brannon and Leelavanichkul [14]. Deformation is prescribed in such a way

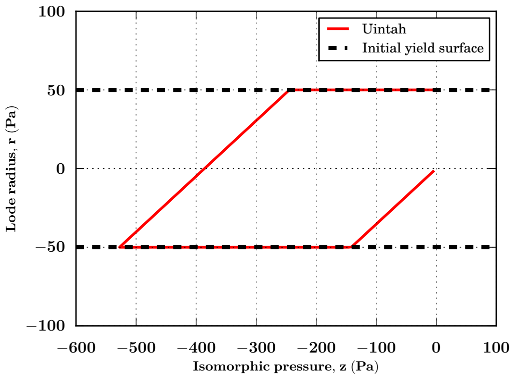

(a) Nonhardening

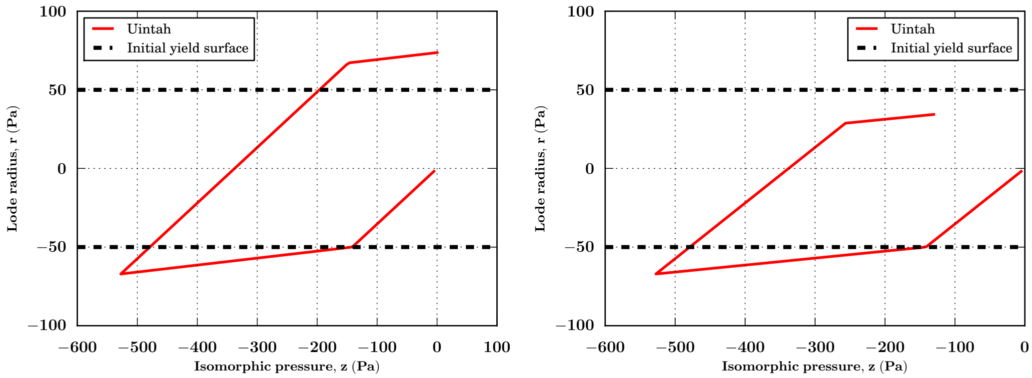

(b) Isotropic hardening (c) Kinematic hardening

Figure 4.6: Uniaxial-strain test results both with and without hardening. View of the stress state (solid line) and yield surface (dashed line) as meridional profile.

that both the stress and strain have fixed eigen vectors with transient eigen values. Further, the strain rate is intentionally misaligned from the yield normal. This test served to verify that the nested return algorithm is able to keep the stress state on the yield surface despite this surface's curvature. The result of this test is presented as Fig. 4.7.

4.1.1.3 Drucker-Prager yield function

Arenisca uses a linear Drucker-Prager yield criterion of the form

$$J_2 + \alpha(I_1 - I_1^{\max})^2 \tag{4.2}$$

in which α and $I_1^{\max}$ are material parameters. Brannon and Leelavanichkul [14] propose a test having a tortuous path meant to comprehensively evaluate the implementation of such a material model (without hardening) near the yield surface's vertex acting both as algorithmic verification and a check of code robustness. Brannon and Leelavanichkul write

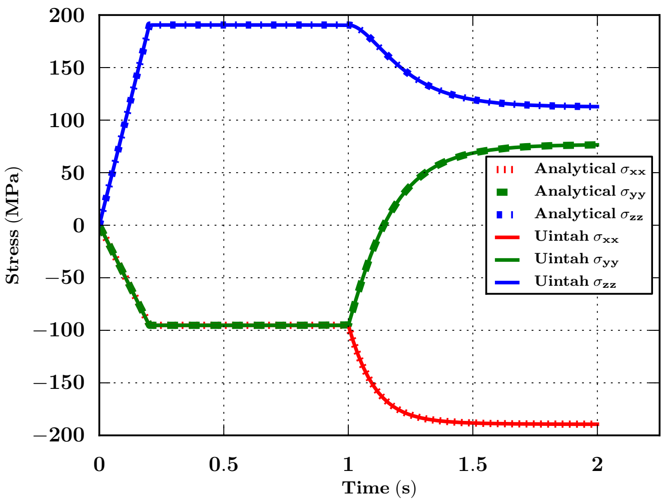

Figure 4.7: Constant eigen vectors with transient eigen values.

the yield criterion in the form

$$\frac{r}{r_0} + \frac{z}{z_0} = 1 \tag{4.3}$$

where r is the cylindrical Lode radius ($r = \sqrt{2J_2}$), z is the isomorphic pressure ($z = I_1/\sqrt{3}$), and r_0 and z_0 are experimentally determined constants determining the friction angle and tensile yield strength, respectively. Comparing the above two equations permits identifying the following relationships between parameters:

$$\alpha = -\frac{r_0^2}{6z_0^2} \qquad \text{and} \qquad I_1^{\max} = \sqrt{3}z_0 \tag{4.4}$$

As illustrated in Fig. 4.8 the material initially undergoes hydrostatic compression followed by loading and unloading legs. The yield events were intentionally devised such that they occur exactly halfway through the second and third legs. Further, the first yield event may appear to only just briefly contact the yield surface prior to unloading, but in fact by design, dwells at this point undergoing extended plastic deformation, the dwell period being the result of alignment between the trial stress rate and the return projection direction $\underset{\approx}{\mathbf{P}}$. On the last leg, the trial stress rate is exactly parallel to the yield surface normal $\underset{\approx}{\mathbf{N}}$, not to be confused with the flow direction $\underset{\approx}{\mathbf{M}}$. The results of this test, presented as Fig. 4.9, demonstrate that the model is performing accurately on all but the last leg, thus highlighting as-yet unresolved problems in the return algorithm used to compute plastic stress updates.

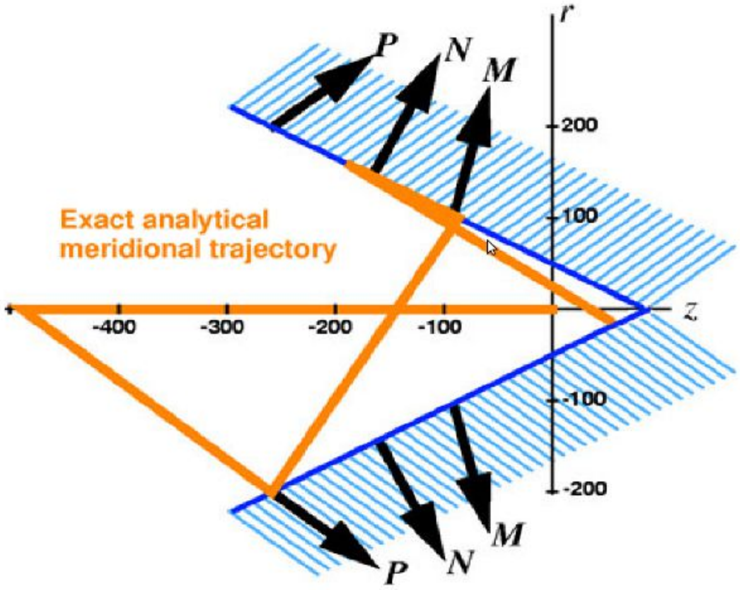

Figure 4.8: Geometry of Drucker-Prager verification test. Alignment of the trial-stress rate with the return projection direction ($\underset{\approx}{\mathbf{P}}$) results in stagnation at the stress states intersection with the yield surface under continued plastic deformation by design. From [14]

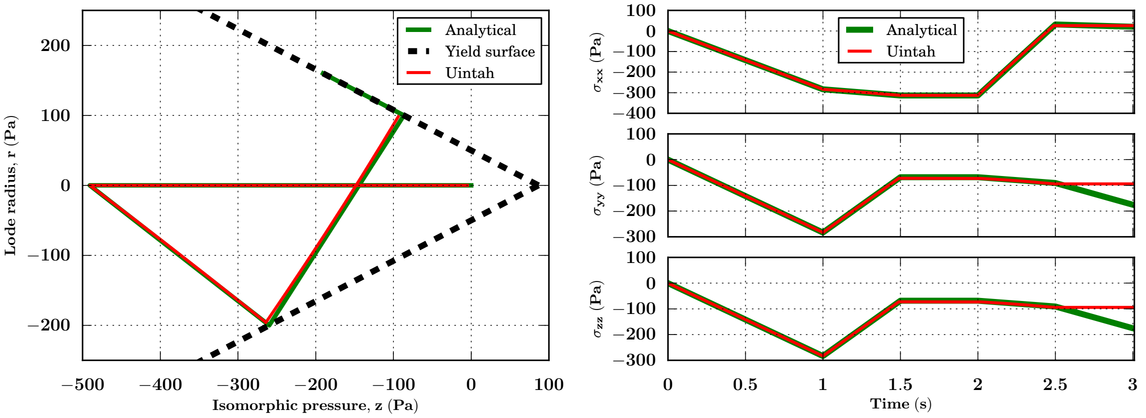

(a) (b)

Figure 4.9: Linear Drucker-Prager verification test results.

4.1.1.4 Yield surface with curved cap

Arenisca uses an associative multisurface Drucker-Prager cap model. This class of model is widely used to predict the constitutive behavior of geomaterials in numerical analyses [63]. The first portion of this surface is described by a linear Drucker-Prager model, while the second portion, the cap, is described by an ellipse having eccentricity which allows porosity to affect material shear strength [32].

Similar tests to those of section 4.1.1.2 are now performed as a qualitative evaluation of the full curved-cap linear Drucker-Prager yield surface. Analytical solutions of these problems do not currently exist because of the complicated path-dependent evolution of the ISVs describing the yield surface. These tests therefore are meant to serve as *trend* verifications built on the previous analytical uniaxial-strain J_2 verification tests. For the first test, compressive uniaxial strain brings about yielding while hardening and cap evolution are suppressed, fixing the yield surface in place. By design, the stress path first intersects the Drucker-Prager portion of the surface. With increasing stress, the stress state transitions from the linear to the curved cap portion of the yield surface. As hardening and cap evolution are not allowed, the expected outcome is one where the stress history traces the fixed yield surface, and this result along with those discussed below for hardening are presented in Fig. 4.10.

A second test of the full yield surface allowing hardening through cap evolution (representing changes in porosity) serves as test of these features. In this instance, upon reaching yield, the stress state is expected to move outwards from the initial yield surface in order to stay always on the outwardly expanding yield surface. This trend is exhibited in Fig. 4.10b, though more rigorous verification against analytical solutions is warranted.

Hydrostatic compression is another important loading mode in geomaterials specifically in the simulation of penetration. Currently, in order to achieve preconfinement (overburden/confining stress), the process of applying this pressure (hydrostatic compression) must be simulated, which requires verification. Similar to the approach taken for verification in uniaxial strain, first the material model is tested without hardening. In hydrostatic compression the stress state is expected to be purely isotropic (have no shear components, *i.e.,* lying on the hydrostat), which upon reaching the yield surface should dwell at this intersection, as is verified in Fig. 4.10c.

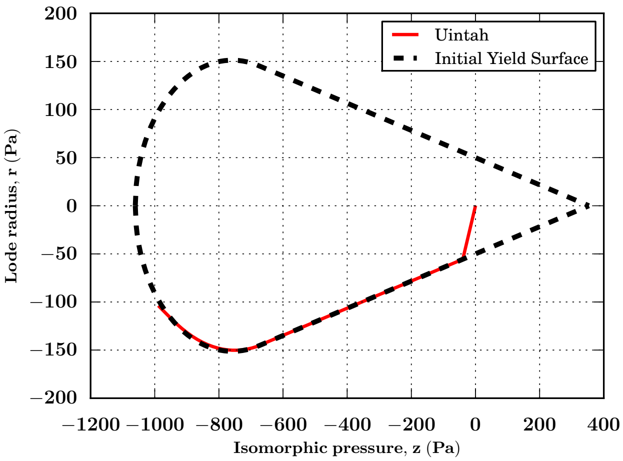

(a) Nonhardening

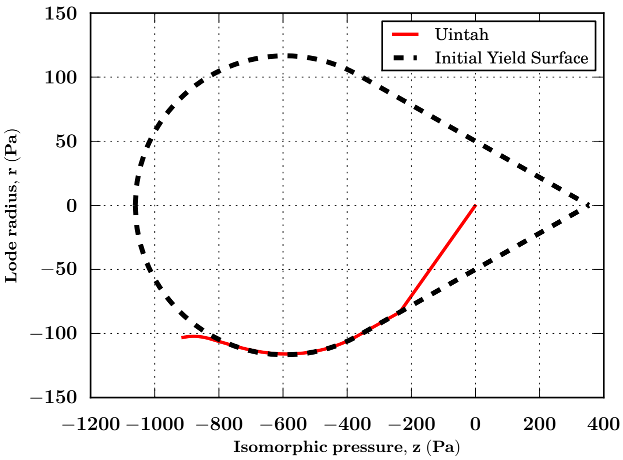

(b) Isotropic hardening with cap evolution

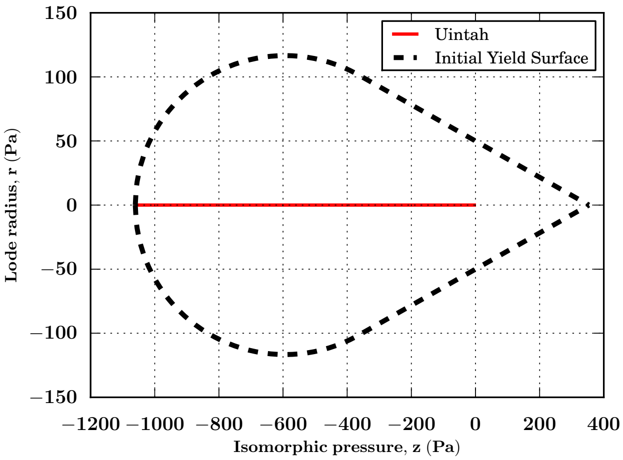

(c) Hydrostatic compression fixed cap

Figure 4.10: Linear Drucker-Prager verification test results.

Now verification of cap evolution is performed. Cap evolution results from pore compaction (*i.e.,* changes in porosity). In hydrostatic pressure vs. volumetric strain data, pore compaction is inferred from the observered accumulation of plastic volumetric strain. Specifically, the following empirical relationship is assumed to exist between the cap location on the hydrostat and the material porosity:

$$\phi = \begin{cases} 1 - \exp(-P_3 \exp(P_1(I_1 - P_0))) & I_1 < P_0 \\ 1 - \exp(1 - P_0 P_1 P_3 \left(\frac{I_1}{P_0}\right) - P_3) & I_1 \geq P_0 \end{cases} \tag{4.5}$$

where ϕ is material porosity, I_1 is the first invariant of stress, and the material parameters P_0, P_1, and P_3 are inferred from experimental undrained hydrostatic compression data, and are used to establish the initial yield surface. Plastic stress states where $I_1 < P_0$ represent plastic pore compression with respect to the initial material properties and conversely $I_1 \geq P_0$ is a state representing plastic pore expansion. In post processing of simulation results the relationship

$$\phi = 1 - \exp(-(P_3 + \epsilon^p_{\text{vol}})) \tag{4.6}$$

is used to determine porosity from the plastic volumetric strain ϵ^p_{vol} and P_3 parameter. Fig. 4.11 presents the results of a hydrostatic compression test. Initially porosity remains constant (horizontal component of the red line) until the material yields and plastic pore compaction occurs, at which point simulated porosity follows the dashed-green compressive analytical solution line.

Having performed basic qualitative verification of the porosity model, simulation of a complicated hydrostatic load-unload curve – like those used experimentally to calibrate the model – is undertaken. On the first leg of the test the material undergoes elastic compression (1 to 2), followed by plastic compression (2 to 3) and then elastic relaxation (3 to 4) to a tensile state, followed by further plastic dilatation (4 to 5) resulting in increased material porosity after which the material is compressed elastically (5 to 6) before transitioning to plastic deformation and nearly being completely crushed to a nonporous state (6 to 7). The results of this test are presented as Fig. 4.12.

Incorporation of fluid effects into the Arenisca geomodel has been a continued focus of model developers. As in both laboratory and in-situ testing environments, fully drained sandstone is rarely used, making a properly functioning fluid effects model of high importance. A challenge to this continued effort is the development of verification tests to

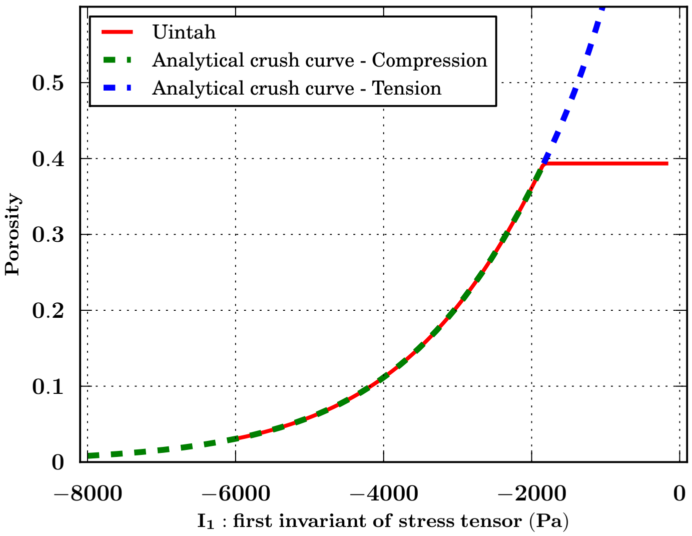

Figure 4.11: Evolving porosity as a result of yield surface cap evolution test results.

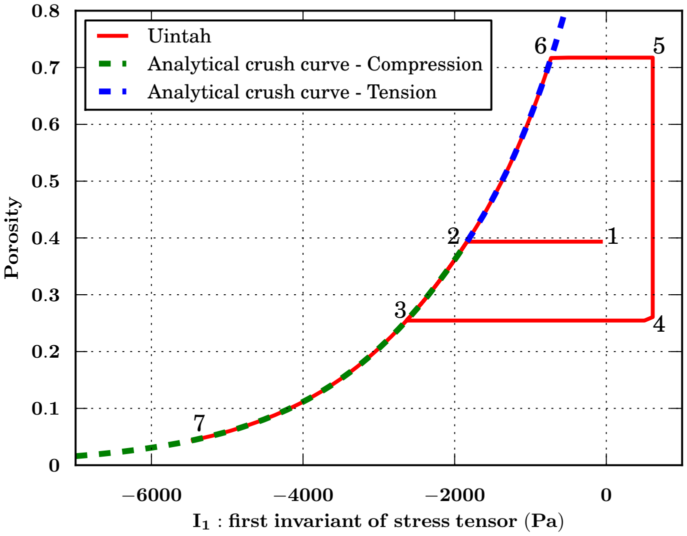

Figure 4.12: Hydrostatic load-unload verification test results.

ensure that the fluid model is functioning as desired. One such (qualitative) verification test compares the response of a material element undergoing hydrostatic compressive loading with and without fluid effects enabled. The desired trend is an apparent increase in material stiffness with fluid in the pore space. Interpreted physically, this fluid carries a portion of the applied pressure and accordingly the change in porosity is smaller. This desired trend is demonstrated in Fig. 4.13. Currently Arenisca does not pass this test. The effective-stress concept, meant to account for this result in analytical penetration models, is an important

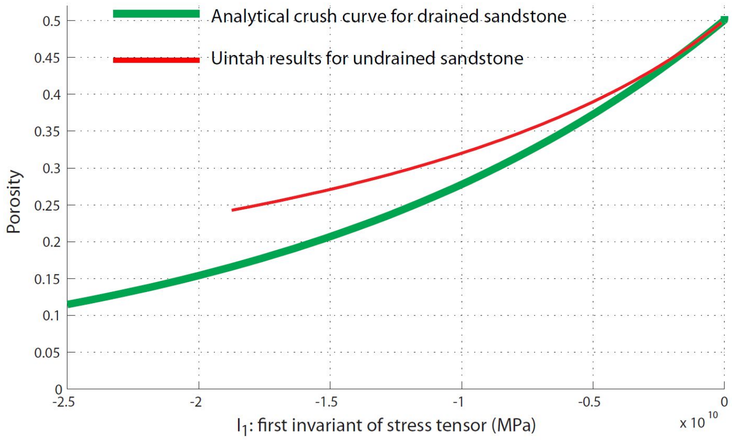

Figure 4.13: Fluid effects verification test. Hydrostatic compression demonstrating the expected trend when simulating the effects of fluid in the porespace.

part of the Grove penetration correlation formulas discussed previously in Chapter 3.

4.2 Robustness Testing

While the above verification tests and tools are important in maintaining confidence in the model, these tests because of their relatively simple nature frequently fail to capture material states leading to nonphysical solutions and/or code-halting events. This breakdown of simple verification tests in preventing such failures is largely due to the extremes associated with a hypervelocity penetration event, which can be characterized by high velocities (6–10 km/s), strains (> 10), strain rates ($10^7/s$), rotation rates, pressures (200^+ Gpa), and temperatures (500-600 C) [5, 2]. In this loading domain, carefully crafted analytical solutions are not readily available, though model confidence is needed if predictions in this regime (the purpose of its development) are to be meaningful. Further it is most typically under these conditions that unexpected model failures occur. Frequently such failures appear without apparent cause. The ability to extract particle histories from existing simulation datasets was therefore undertaken so that those histories could be analyzed in single-element testing in order to understand and resolve these issues.

4.2.1 Reproduction of Particle Histories as Extracted from Simulation Results

Previous work [28] added the ability to apply homogeneous deformation histories to a material within the Uintah computational framework. This feature was intended for use in single element testing whereby time varying deformation/rotation of a material element is specified in the form of an F-table. An F-table consists of discrete time entries and the associated components of a material's deformation gradient tensor $\underset{\approx}{\mathbf{F}}$, with an option to include a superimposed rotation matrix $\underset{\approx}{\mathbf{Q}}$ (specified by angle of rotation in degrees θ about a specified axis $\underset{\sim}{\mathbf{a}}$). Simulation timesteps during the execution of a single-element test were originally controlled by host-code/input specifications, where the deformation gradient at any given time is obtained by linearly interpolating between $\underset{\approx}{\mathbf{F}}$ values in the F-table, while the superimposed rotation was constructed by linearly interpolating the angle and axis individually (then applying the Euler-Rodrigues formula to construct $\underset{\approx}{\mathbf{Q}}$). While this interpolation scheme served well for the above simple verification tests, it is inherently unable to reproduce the exact deformation histories experienced by a particle in the simulation from which the F-table values were extracted. These small interpolation errors accumulated over time, resulting in particle histories that were initially very similar to those in the source simulation, but which eventually deviated enough to preclude reproducing the particle failure. The source of this problem, as well as its resolution, is rooted in the need to compute changes in kinematical quantities in a manner that is exactly consistent with kinematics assumptions in the host code. Specifically, the constitutive model at each step takes as input the velocity gradient tensor $\underset{\approx}{\mathbf{L}}$, as computed by the host code from the deformation gradient tensor $\underset{\approx}{\mathbf{F}}$ and its rate $\underset{\approx}{\dot{\mathbf{F}}}$ by the well-known relationship

$$\underset{\approx}{\mathbf{L}} = \underset{\approx}{\dot{\mathbf{F}}} \cdot \underset{\approx}{\mathbf{F}}^{-1} \tag{4.7}$$

Initially, when F-tensors were interpolated linearly, the velocity gradient was approximated as

$$\underset{\approx}{\mathbf{L}}^{n+1/2} = \frac{\underset{\approx}{\mathbf{F}}^{n+1} - \underset{\approx}{\mathbf{F}}^{n}}{\Delta t} \cdot \left(\frac{\underset{\approx}{\mathbf{F}}^{n+1} + \underset{\approx}{\mathbf{F}}^{n}}{2} \right)^{-1} \tag{4.8}$$

In a collaborative analysis of this problem with an original Uintah developer [68], it was proposed to change the interpolation scheme to be consistent with the kinematics updates actually performed in the source simulation, where the velocity gradient $\underset{\approx}{\mathbf{L}}^{n+1/2}$ is taken to be constant thoughout the step. During a full simulation, the velocity gradient $\underset{\approx}{\mathbf{L}}$ is computed and, taking it to be constant though the step, the deformation gradient $\underset{\approx}{\mathbf{F}}$ is then evaluated using a the first-order updated-Lagrangian integration of $\underset{\approx}{\dot{\mathbf{F}}} = \underset{\approx}{\mathbf{L}} \cdot \underset{\approx}{\mathbf{F}}$ as follows:

$$\underset{\approx}{\mathbf{F}}^{n+1} = \left(\underset{\approx}{\mathbf{I}} + \Delta t \underset{\approx}{\mathbf{L}}^{n+1/2} \right) \cdot \underset{\approx}{\mathbf{F}}^{n} \tag{4.9}$$

Solving this equation for $\underset{\approx}{\mathbf{L}}^{n+1/2}$ ensures that the velocity gradient sent to the constitutive model in a single element test would be consistent with the source simulation providing its F-table. This correction was made where, instead of Eqn. 4.8, the following discrete update is now used:

$$\underset{\approx}{\mathbf{L}}^{n+1/2} = \frac{\underset{\approx}{\mathbf{F}}^{n+1} \cdot (\underset{\approx}{\mathbf{F}}^{n})^{-1} - \underset{\approx}{\mathbf{I}}}{\Delta t} \tag{4.10}$$

Making the above change resulted in the ability to exactly reproduce a particle's history, or any arbitrary history, so long as the material model is able to track the intended strain rate at each step. As a result of these changes, additional inspection of the results [68] suggested that the current calculation of $\underset{\approx}{\mathbf{L}}^{n+1/2}$ used as input to the constitutive model might also need revision.

Figure 4.14 illustrates accumulated absolute L_2 error in comparing the expected and extracted deformation history of a single-element test, as generated from an extracted particle's history, at various stages of the solution. At first, inability to reproduce particle histories was recognized. Then the use of exactly specified time steps resulted in overall reduction in the error, and ultimately the method as described above resolved the issue resulting in exact reproduction of the particle history up to and including particle failure. The single error spike at the last step is in fact the sought-after particle failure.

4.2.2 Automated Single Element Testing Driven by Simulation Results

A python script was written (see Appendix) in order to automate the process of parsing a simulation log file, extracting failed particles histories, converting them to input F-tables, writing a corresponding input file for Uintah, executing said test, and comparing the results. The purpose of this effort was two-fold: first to determine if consistent particle failure can be achieved using only the available output data, and second to create a database of failed particle histories that might be useful in determining characteristic load paths that might induce q model failure. These archived histories can be perturbed by a user using the same script in a variety of manners in order to generate an infinite number of unique but similar histories, which will hopefully provide future insight into what algorithmically causes failures of this type under large-deformation high-rate loading. The intent being development of verification tests to capture these problems, and ultimately their resolution.

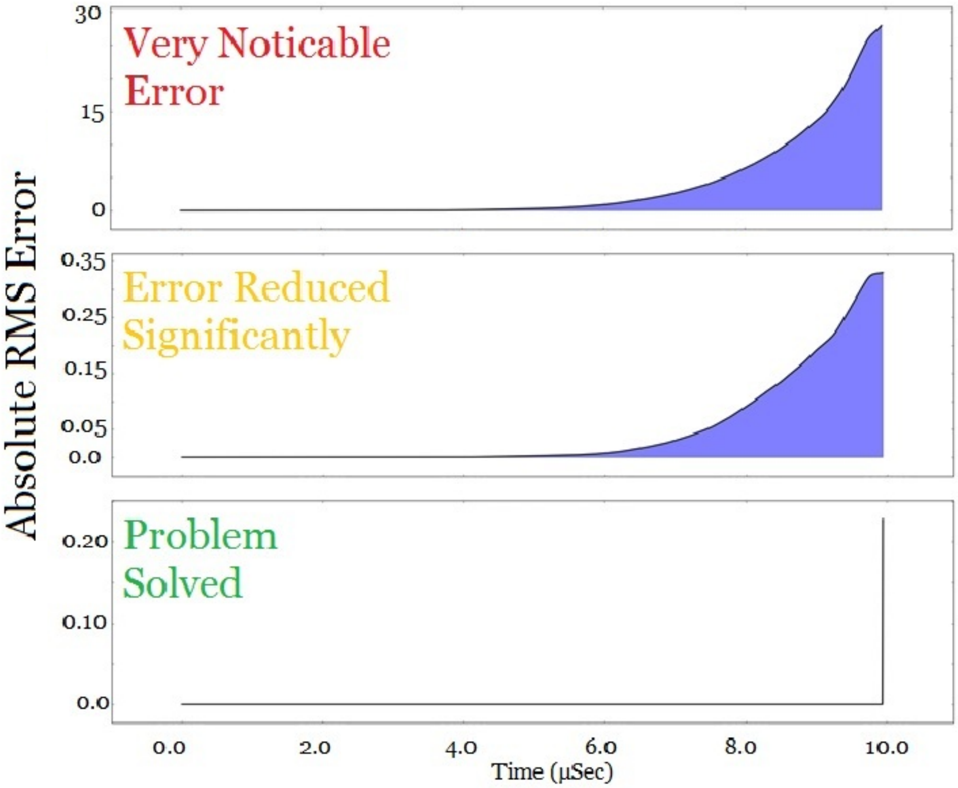

Figure 4.14: Error in comparing extracted and expected deformation histories of a particle at three stages of the solution. At first the problem was recognized as in the top frame. Then a more exact time step was used, resulting in the reduction in error of the middle frame. Ultimately, the described method of section 4.2.1 was used to reproduce particle failure, which is the cause of the small error spike on the last step of the bottom frame. For numerical reasons, especially considering that the source simulation was run using different processors than the single-element simulation, it is not surprising that the end state might be slightly different.

CHAPTER 5

PENETRATION SIMULATION RESULTS

This chapter focuses on full-scale simulations of the wellbore completions process. Simulations of this nature are very complex, as they require multiple numerical solution schemes in order to model the behavior of very different materials, each of which undergoes rapid and extensive deformations during a simulation. Further, such numerical solutions are computationally expensive and frequently necessitate simplifying assumptions for tractability. Additionally, both the model and host code are in a constant state of flux as they undergo continued and extensive modification, making direct comparison of results obtained at different points in time problematic. Despite these challenges, a large number of simulations were executed, the purpose of which was twofold: to validate the model against the experimental and simulation results of others and to test the material-model and host-code robustness.

5.1 Simulation Setup

All penetration simulation results presented in the following sections take advantage of axisymmetry. In each, a 2-d plane is used to simulate a larger 3-d cylinder of sandstone like those used to obtain experimental results. This plane represents the computational domain, which is represented by a structured background grid of cells much like in a traditional finite element scheme. In contrast to FEM, the material point method represents materials within this domain not by the aforementioned grid but by an overlaid discretization of particles. A typical simulation domain and discretization is illustrated in Fig. 5.1.

Another simplification used to reduce computational costs is a model developed by Burghardt *et al.* [30] to represent a shaped charge jet. This model represents the jet by discretization to cylinders, each of which is separated by a void space (Fig. 5.2). Such a representation is similar in nature to the way Birkoff [3] originally represented particulation and breakup of a jet in his modified Bernoulli model (Eqn. 3.4). Each cylinder has the same density and has its own velocity and geometrical properties. These parameters are tailored to represent the spatially varying properties of a given jet. Hereafter in referring to the 'jet'

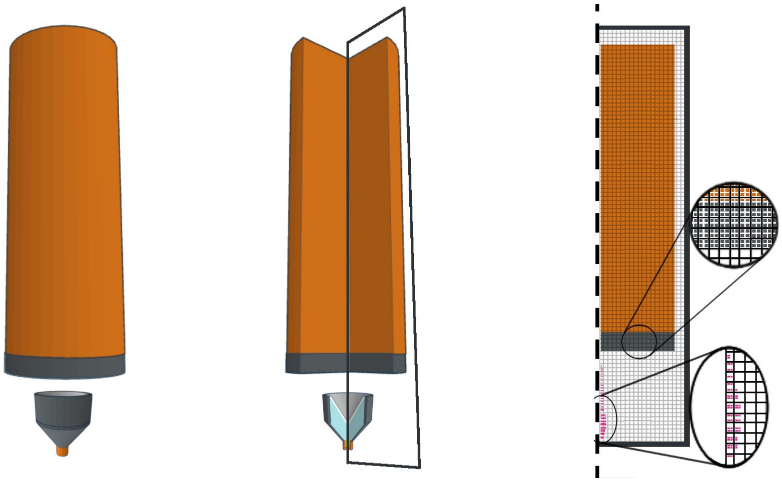
(a) 3-d (b) 2-d slice (c) Simulation

Figure 5.1: Illustration representing a simulations domain and discretization.

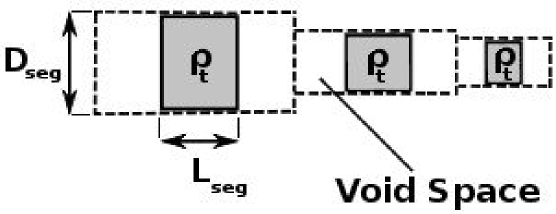

Figure 5.2: Illustration of the discrete shaped-charge jet model. Each cylindrical segment has the same density (ρ_t), but has its own velocity (V_{seg}) and geometrical properties (diameter D_{seg} and length L_{seg}).

penetrator, the discrete cylinder properties of Figures 5.3 through 5.4 are being used. This model was shown by Burghardt *et al.* as capable of accurately capturing the penetration history of a shaped-charge jet in penetrating an aluminum target. It was discovered that this model is more susceptible to certain issues as discussed later in Chapter 6. As a result, this penetrator is frequently replaced by a long-rod penetrator preventing these issues; doing so has the added benefit of being more directly comparable to many analytical penetration models used as a form of validation.

The motivation of Arenisca's development, as mentioned previously, is to improve the predictive capabilities of numerical models for well bore completion. Overburden, which is the rock or soil overlying a target geologic formation, is recognized as playing a significant role in the resulting depth of penetration of a shaped charge. To obtain experimental results capturing the influence of overburden, the oil industry uses a fluid bath and hydraulic cylinders to hydrostatically compress a target sample of rock mimicking overburden. While

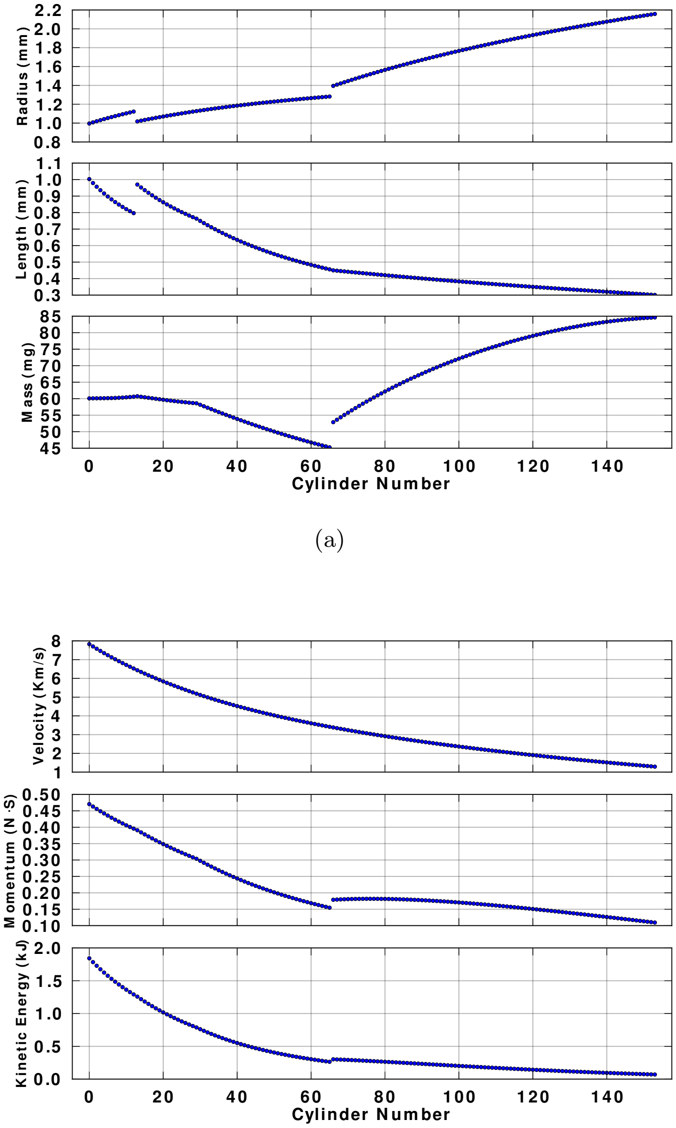

(a)

(b)

Figure 5.3: The discrete jet description's individual cylinder properties. (a) contains profiles for cylinder radius, length and mass, while (b) contains profiles of cylinder insert velocity, momentum, and kinetic energy. Figure 5.4 correlates these properties with time.

this entire process could in theory be simulated by Uintah, it would significantly increase the cost and complexity of a simulation. Instead, this confining stress is modeled by pressures on the outside, top, and bottom of a target. These pressures are represented by discretization to a group of point loads, each of appropriate magnitude and direction, which are then individually applied to particle centers of the layer of particles nearest to the material's free surface. Because of the way this is done, simulations making use of this method

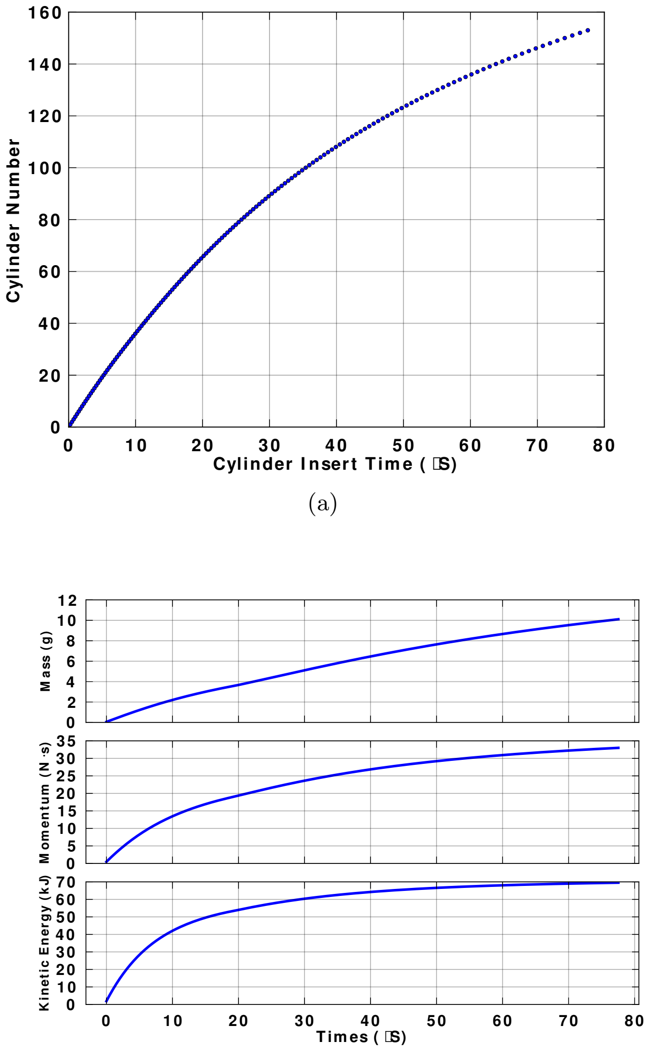

(a)

(b)

Figure 5.4: The discrete jet description's properties as they vary with time. (a) correlates cylinder number with time of arrival/insert time, while (b) contains plots of the cumulative deposition of mass, momentum, and kinetic energy into the simulation domain throughout time. Refer to Fig. 5.3 for the properties of an individual cylindrical segment of the jet.

must necessarily have a free surface, and be placed at least two (and preferably five) cells away from the outer edge of the overlaid grid to avoid having these particle point loads anomalously influence the nodal forces at the grid boundary. Further, while the pressure could be applied at its full magnitude as an initial condition, doing so results in stress waves that propagate throughout the material over time. The constructive/destructive interference of these waves with one another results in large fluctuations throughout time. To mitigate this problem the applied pressures can be prescribed by linear interpolation of a table of times and values. This method was then used to ramp the pressure from zero to a desired value. Using this pressure ramp failed to prevent the significant fluctuations observed in the stress field, which is demonstrated in Fig. 5.5.

Uintah has a viscous damping feature meant to achieve quasistatic solutions. This feature uses an artificial damping coefficient (c) to compute penalized nodal accelerations ($\underset{\sim}{\mathbf{a}}^*$) using the computed nodal accelerations ($\underset{\sim}{\mathbf{a}}$) and velocities ($\underset{\approx}{\mathbf{v}}$) by

$$\underset{\sim}{\mathbf{a}}^* = \underset{\sim}{\mathbf{a}} - c\underset{\sim}{\mathbf{v}} \tag{5.1}$$

Using this feature, a damping coefficient able to critically damp out the pressure oscillations was selected for both material parameterizations with and without fluid effects. To determine these parameters, a sandstone cylinder with a radius of 20 cm and length of 30 cm was subjected to a uniform confining pressure of 6.895 MPa (1 ksi) having a target time of 50 μs at a cell resolution of 1 mm and particle resolution of two particles per cell per direction. Through trial and error, a damping value of 75,000 1/s was found to be most effective (see Fig. 5.6a). For the case of the material parameterization with fluid effects (*i.e.,* for saturated sandstone), it was determined in a similar manner that a value of 90,000 1/s was effective, though minor overshoot above the target value occurs (Fig. 5.6b). Given

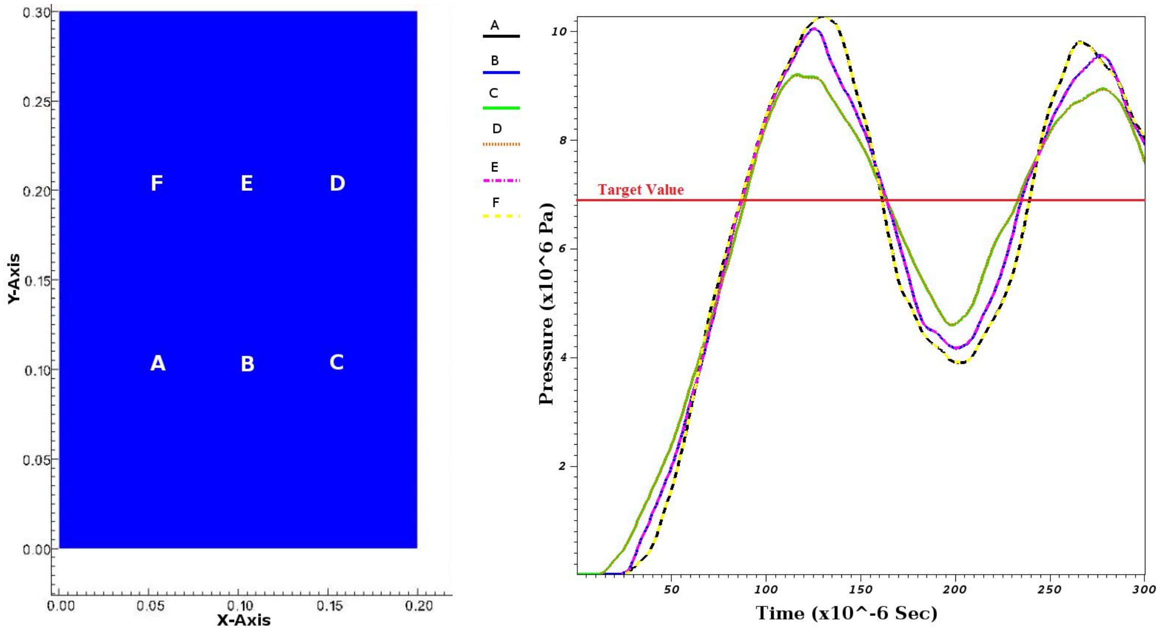

(a) (b)

Figure 5.5: Pressure histories at different points in space without using viscous damping demonstrating large fluctuations in the pressure field throughout time.

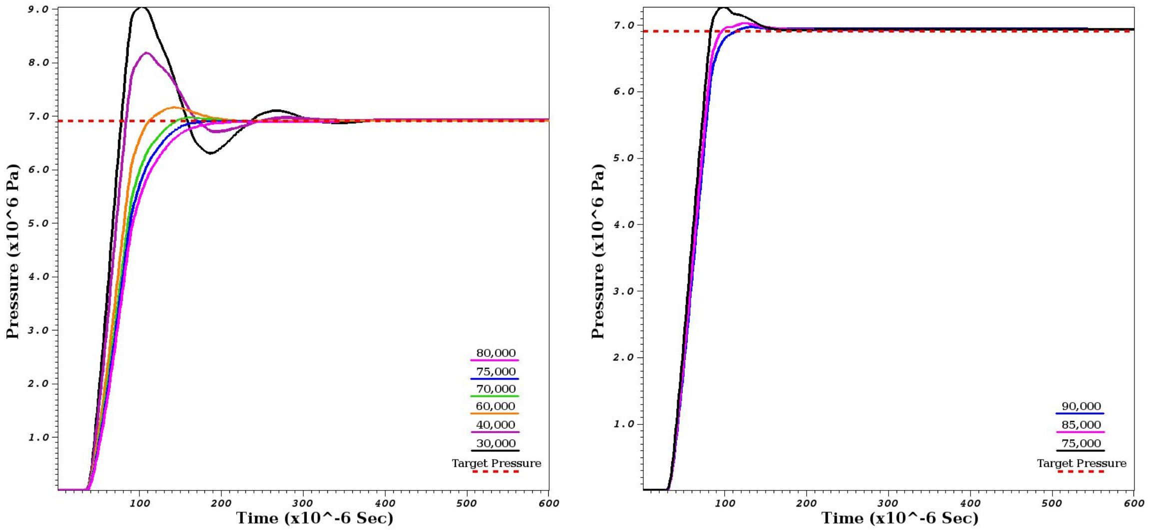

(a) without fluid effects

(b) with fluid effects

Figure 5.6: Multiple pressure histories demonstrating the effectiveness of viscous damping. In both cases the histories were obtained from a point near point A of Fig. 5.5a.

that, at the time, including fluid effects caused considerable robustness issues, a value of c closer to critically damped was not sought. Further, as the model has undergone, and continues to undergo extensive changes, a similar study should be carried out in order to determine appropriate damping coefficient values, as they may change. The same is true of any new material specification until a better method of applying a confining stress is developed. After the most recent code changes, the viscous damping coefficients value was reassessed and the selected value found to be acceptable despite now being slightly under damped.

Having selected an appropriate damping coefficient, target ramp and equilibrium times were determined. The target ramp time is the time used as the input to the pressure condition and the equilibrium time is the time at which the entire target should be within ±5% of the target pressures value and can then be shot with a penetrator. It was found that using the above method, pressure increases at a rate of approximately 0.2 cm μs^{-1}. Using this rate, a rule of thumb was developed that is able to produce satisfactory pressure fields in the target material. First, the expected target time is calculated using the inverse of the ramp rate. Second, this time is multiplied by three and rounded up to the nearest 50 μs, this value is the target time. Third, the satisfactory equilibrium time is set to be approximately 300 μs later rounded up to the nearest 100 μs. It was later determined that the lowest pressure simulations were able to equilibrate earlier, and so the target and equilibrium times of Table 5.1 were used.

Having taken all of the above steps, a simulation must then be stopped at the equilibrium time, and the damping coefficient manually set to zero prior to restarting the simulation and shooting the target with a penetrator. As this must be done frequently, and further, because these simulations must be performed using shared high speed computing resources, this process was automated using a simple Python script (listed in the Appendix) in order to avoid what can be long wait times in the batch queuing system prior to a job's execution.

Uintah's parallelization makes it possible to solve solid mechanics problems like that of the wellbore completions process. Despite this impressive ability, such parallelization is not without certain drawbacks. One such drawback revealed itself as a result of the way the discrete jet is initialized. At the beginning of a simulation, each of the discrete cylinders of the jet is placed in a location sufficiently far away from the target in order to avoid unintended interaction with the debris that results during a penetration event. Initially each cylinder has zero velocity and will stay at rest until a user specified point in time is reached, at which point this cylinder is instantaneously transported along the axial direction towards the target a set distance, and then prescribed a user specified initial velocity. This method allows the jet standoff to be controlled independently from the initial distance to the target. When parallelizing a Uintah simulation, the computational domain is again further subdivided into patches. Each patch is a rectangular selection of background grid cells. The solution of each patch is then computed independently by a single processor. To enforce compatibility, adjacent patches communicate information pertaining to particles as they cross a shared patch boundary. Generally speaking, the greater the number of patches, the smaller a given patch's portion of the solution will be. This approach results in decreased time to solution as the wall time required to compute each timestep is decreased. To better understand the effect of different divisions of the domain into patches, a large number of simulations were executed that varied the patching. These simulations revealed a subtle

Table 5.1: Target and equilibrium times for simulations with confinement.

Pressure		**Target time**	**Equilibrium time**
(MPa)	(ksi)	(μs)	(μs)
6.895	1	50	250
34.48	5	200	500
68.96	10	350	700
103.4	15	550	900

nuance to the way consistency between individual patches is enforced. If a particle travels sufficiently fast in comparison to patch length in the direction of travel, so that it crosses two patch boundaries in a single timestep, then it will be deleted. This is done because the patch this particle would enter is unable to access the particle's information as it is not adjacent to the source cell of the particle at the beginning of the timestep. As part of this investigation into the effect of patching, it was determined that it is preferable to have a greater number of patches in the axial direction. At the time of this investigation, each simulation used 128 processor cores and would take approximately two hours to complete. Accordingly, the simulation domain was regularly patched to have 128 subdivisions along its length. This had the effect of making two patch lengths in some instances small enough that the fastest moving jet particles would be deleted upon being prescribed their initial velocity.

To combat this problem, a Python script was written (see Appendix) which is able to read the input deck, and the two files describing the jet, and then shift each cylinder's initial position and insert distance to avoid crossing multiple patches when prescribed its initial velocity. While effective, care should be taken in using this utility as it does not have an awareness of the relative sizes of a given cylinder in comparison to the background grid's cells. As a result, with short enough patches in the axial direction, a jet cylinder can be prescribed an insert distance that is short enough so that it will interact with the stationary cylinders not yet in free flight upon being inserted. To avoid the problems associated with the way a jet cylinder enters the domain, each could instead initially be prescribed its initial velocity, and then positioned with appropriate spacing along the axis. This is not advisable as doing so increases the computational cost of a simulation. This cost is associated with the domain having to be significantly extended in the axial direction. Further, this cost would be wasteful as the added cells and patches would, throughout the duration of a simulation, remain largely unoccupied by material particles. The above described script also has added functionality allowing the user to easily modify an existing jet description in two ways: first, all cylinders can be shifted in time by some amount to have a new insert time, and second, all the cylinders can be moved up or down along the axial direction by some amount.

The results of the aforementioned study of patching effects are presented in Table 5.2. The first key finding is that over patching – where the number of patches is greater than the number of processor cores – can increase efficiency relative to the same number of patches using a greater number of cores. The second key finding is that axial patching tends to increase both efficiency and speed, appearing to have an optimum at 128 axial patches for

Table 5.2: Simulation results investigating the effects of patching and number of processors on runtime. In each the simulation used the same jet and a domain with a cell resolution of 1 mm containing 85,932 cells and 39,735 particles.

Batch number	**Number CPU cores**	**Number patches (radial)**	**(axial)**	**Runtime (hours)**	**(CPU hours)**
28	32	8	8	4.72	151.0
	64	8	8	3.79	242.6
	128	8	16	2.80	358.4
	256	8	32	1.51	386.6
31	32	16	32	7.83	250.6
	64	16	32	4.80	307.2
	128	16	32	3.33	426.2
	256	16	32	2.27	581.1
	512	16	32	1.98	1013.8
32	512	2	256	1.03	527.4
	512	4	128	0.93	476.2
	512	8	64	0.90	460.8
	512	16	32	1.63	818.3
33	128	1	128	0.81	103.7
	128	2	64	1.23	157.4
	128	4	32	2.50	320.0
	128	8	16	1.67	213.8
	128	16	8	1.40	179.2
34	256	1	256	0.83	212.5
	256	2	128	1.22	312.3
	256	4	64	2.12	542.7
	256	8	32	2.22	568.3
	256	16	16	5.09	1303.0

128 processors. The increase in efficiency observed for cases with over patching is apparent in both batches twenty-eight and thirty-one. While over patching *can* increase efficiency, this is not generally true, and the practice is advised against as it results in extraneous iterations within nested for loops and an increase in the number of cross processor communications required. Further, the use of fewer processors takes considerably longer. Accordingly, if time to solution is the critical factor, then the use of an appropriately patched domain and proper number of processors is recommended. It was found that for this setup, approximately 670 cells per patch with all patch divisions along the axial direction is both the fastest and most efficient scheme. As changes to Arenisca have recently caused a significant increase in average run times, this becomes increasingly important.

Another useful method to decrease the computational cost is the use of a multiple particle resolution domain. Typically this involves having a higher resolution (two particles per cell per direction and is considered the most efficient particle resolution when using the GIMP method [21]) core where the penetration channel is expected to occur. This high resolution core is surrounded by a low resolution elastic zone that is discretized at one particle per cell per direction (which reduces to standard single-point FEM where deformations are small). The jet is modeled at an even higher resolution than the core (four particles per cell per direction), as the objects it is comprised of represent the smallest length scales. This higher resolution is intended to provide more accurate deformations and corresponding stresses. Doing the above frequently reduces the number of particles in a simulation by one half. Instead of using different resolutions for the penetrator and core target regions it would be preferred to use a resolution of two particles per cell per direction for both. As a result of the small length scales of jet objects, doing so might require increased refinement of the background cell size in comparison to what is needed for convergence within the sandstone. This remains an unknown as repeated attempts to determine spatial convergence have been unsuccessful because of code robustness issues. More recently, code halting errors have become less common, but because timestep size is controlled by the host code, and based on the Courant-Friedrichs-Lewy condition (CFL number [69]), these problems have been replaced by small timestep issues as a result of particle deformation. Early work (Fig. 5.7) indicates that rate of penetration is influenced by cell size and it is hypothesized that depth of penetration likely demonstrates a similar pattern. All of the results in this and following chapters, when using Arenisca, are reported for a cell spacing of 1 mm in each direction, as this was repeatedly robust against the above issues. Further, unless otherwise indicated each simulation uses the same material parameterization for steel, tungsten, and sandstone, respectively. Both these standard material parameters and individual simulation input decks with other needed files needs (where available) can be found in the Appendix.

5.1.1 Sensitivity to Simulated Boundary Conditions

Depending on whether a simulation is intended to represent a finite or semi-infinite domain, different boundary conditions should be used. For the case of a finite domain – like those frequently used to research shaped charge penetration phenomena in the laboratory – the material boundary should modeled as a free surface. Doing so acts to reflect the stress waves produced by the penetration event in the same way that these waves would be expected to reflect and interfere in an experimental target. Alternatively, to represent a semi-infinite domain, either a free or fixed boundary condition can be used, but in both

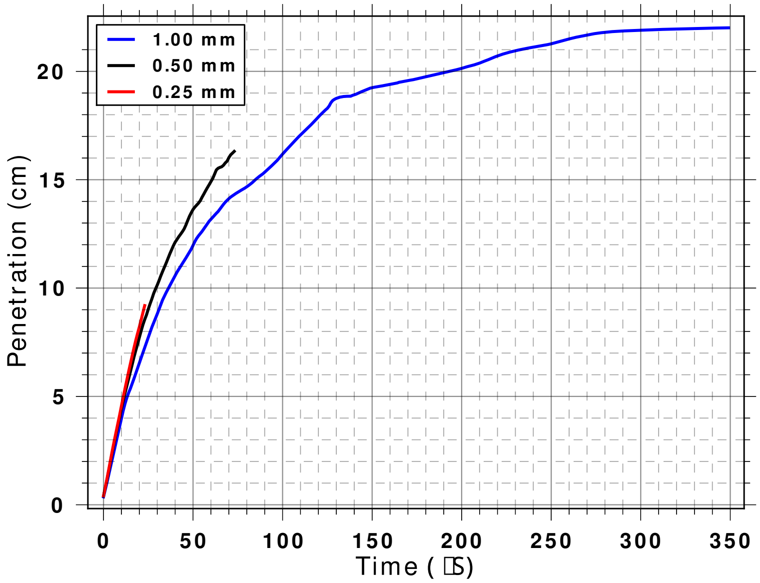

Figure 5.7: Comparison of penetration histories obtained for three different background grid resolutions. While neither the 0.5 m or 0.25 m resolution simulations successfully ran to completion (a result of particle domain inversion errors), the rate of penetration clearly has yet to spatially converege. The same is likely true of other measurable quantities.

cases requires a domain sufficiently extending in radial direction. An extended domain in the radial direction should provide dissipation of stress waves prior to their reflection, which in turn prevents large constructive interference (*e.g.,* spall) at the centerline where penetration takes place. A large number of simulations, using an early version of Arenisca confirmed these results. Using a free surface boundary, penetration depth for large diameter targets is insensitive to target diameters greater than approximately 0.35 m. Otherwise, penetration depth increases with decreasing target diameter. This result, presented in Fig. 5.8, agrees with the finding of Wesson and Pratt [70] who conducted similar experiments in order to determine the effect of differences in standard test sizes used to report the capabilities of a shaped charge. Conversely, for a fixed boundary, as used to simulate a semi-infinite target, penetration depth decreases with decreasing target diameter. This qualitatively makes sense, given that as the fixed boundary gets closer to the centerline the effective radial stiffness increases as outward radial expansion is resisted. More importantly, as the target diameter is increased, both the fixed and free boundary conditions approach the same depth of penetration, which is the qualitatively expected trend. The reason for the penetration depths versus diameter lines of Fig. 5.8 crossing for the two different boundary conditions is not well understood and could be the result of wave phenomena like those

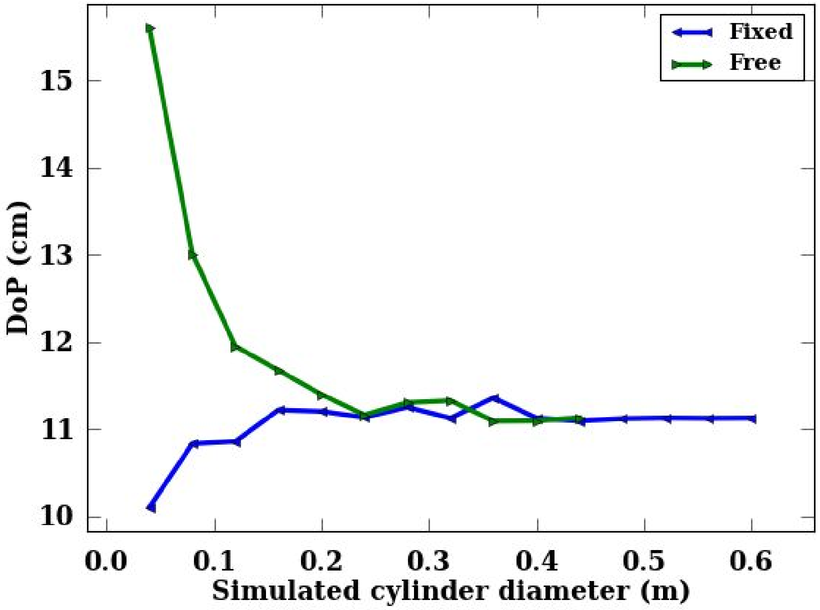

Figure 5.8: The effects of free surface boundary type selection. The legend entry 'Fixed' corresponds to simulating a target cylinder having a fixed (Dirichlet condition to enforce zero velocity on the) outer surface, while 'Free' corresponds to the outer surface being free from the effects of any boundary condition.

previously discussed or possibly of the issues discussed in Chapter 6. A subset of these simulations were repeated for a fixed boundary using a recent version of Arenisca. In this instance, a long-rod tungsten penetrator using a different erosion algorithm was used to penetrate a sandstone target without the steel liner. A comparison of the normalized depth of penetration versus target diameter is presented in Fig. 5.9. In each case, depth of penetration is normalized by the maximum of the dataset. A similar trend is apparent, although the new one is better behaved, with the exception of a small nonmonotonicity as the target diameter was reduced. Though this small jump in penetration depth is currently not well understood, it is not particularly concerning as a fixed boundary target this small would not be used in practice.

A similar study on the effects of target length was conducted in conjunction with the above long-rod penetration simulations. It was found that target length for a fixed boundary has less of an effect on the resulting penetration depth. Only a maximum difference in depth of penetration of approximately 3% was observed over target lengths ranging from 0.2 m to 1.0 m. It is recommended that a similar study be repeated for targets with a free boundary as the reflection of stress off the tail end of a long-rod penetrator is frequently reported to end the initially transient penetration phase for such a penetrator, and it is possible that a

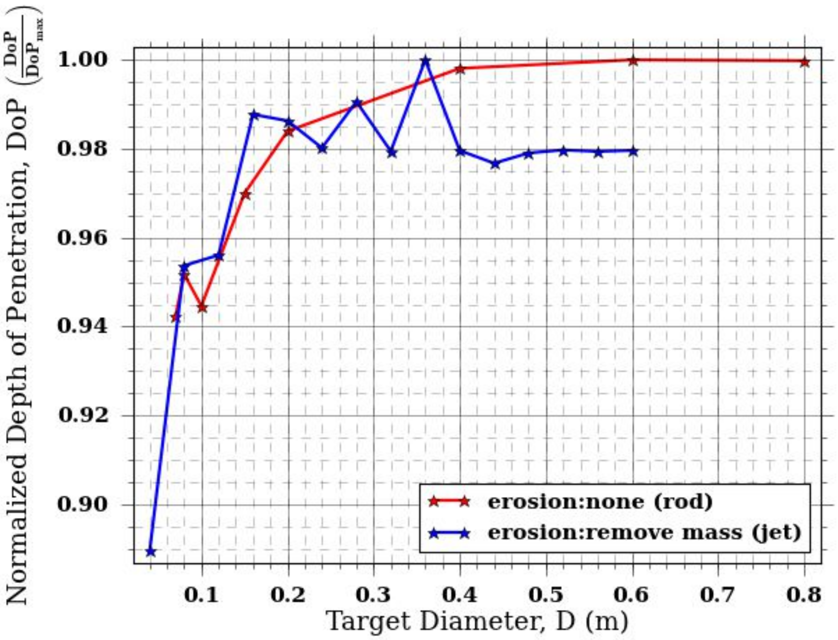

Figure 5.9: Comparison of fixed outer boundary effects for two versions of Arenisca each using different erosion options and penetrators. The blue line of this figure corresponds to the blue line of Fig. 5.8 and uses an older version of Arenisca with the discrete jet as a penetrator and the *RemoveMass* erosion option. The red line on the other hand uses the most recent version of Arenisca, a rod penetrator, and the erosion option *none*.

similar effect might result from wave reflection as the distance from the free surface at the end of the target to the penetration front is reduced.

5.2 Simulation of Hypervelocity Long-Rod Penetration

Largely as a result of issues reported in the next chapter, use of the discrete jet model was abandoned. In its place, long-rod penetrators were used to evaluate Arenisca's ability to simulate hypervelocity penetration phenomena. In each instance, a target having a radius of 20 cm and length of 25 cm (or longer) was used so that boundary effects may be neglected. Recently Orphal and Anderson [71] came to the conclusion that there is fundamentally a linear relationship between the steady-state rate of penetration (U) for an eroding rod penetrator and its initial impact velocity (V).

$$U = a + bV \tag{5.2}$$

where a and b are constants for a given penetrator-target pairing. If hydrodynamic penetration is assumed, a and b become zero and one half, respectively. Though this relationship does not account for the onset of eroding rod penetration it does, where applicable, lead to the observation that the dynamic strength difference (as used in many models) also has to depend on impact velocity. Substituting the above equation for U into the governing equations of Eichelberger/Alekseevskii-Tate (Eqn. 3.9) results in a dynamic strength difference of

$$(R-Y) = \left[(a^2+2ab+b^2V^2)\left(\frac{\rho_p-\rho_t}{2}\right)\right] - a\rho_pV - \left(b-\frac{1}{2}\right)\rho_pV^2 \tag{5.3}$$

which, by taking the partial derivative of the this equation with respect to impact velocity, then setting the result equal to zero and solving for V, gives the location of the maximum or minimum V_m:

$$V_m = \frac{a\rho_p-(\rho_p-\rho_t)(ab)}{\rho_p+(\rho_p-\rho_t)b^2-2\rho_pb} \tag{5.4}$$

To determine if this is a maximum or minimum the second partial derivative is found by

$$\frac{\partial^2(R-Y)}{\partial V^2} = \rho_p(b-1)^2-\rho_tb^2 \tag{5.5}$$

If this value for $\partial^2(R-Y)/\partial V^2$ is negative then the strength difference at $V=V_m$ is a maximum. On the other hand, for a value that is positive at $V=V_m$ the strength difference is at a minimum. Figure 5.10 illustrates these two regions for penetration of sandstone ($\rho_t = 2300$ kg m) by tungsten (red), copper (cyan), and penetrators with a density between these materials (intermediary colors), as these are materials used to manufacture sintered shaped-charge liners. The region where $\partial(R-Y)/\partial V^2$ is negative corresponding to a maximum strength difference and is indicated by the cross hatching. The two vertical dashed lines on the left side of Fig. 5.10 indicate the transition from this region (penetration characterized by having a maximum strength difference), to the region characterized by having a minimum strength difference. These values of b, 0.743 and 0.664 for tungsten (red) and copper (cyan), respectively represent hydrodynamic penetration, where strength effects are unimportant. Further, for the same material combinations, there is theoretically a second root crossing as indicated by the dashed vertical lines on the right of Fig. 5.10, but based on the fact that Orphal and Anderson, for a wide range of material pairings, reported values of b only between 0.269 (Al/Au) and 0.836 (tungsten/Al_2O_3), it is not expected for b to lie outside this range. To determine if Arenisca produces similar trends, long-rod penetration

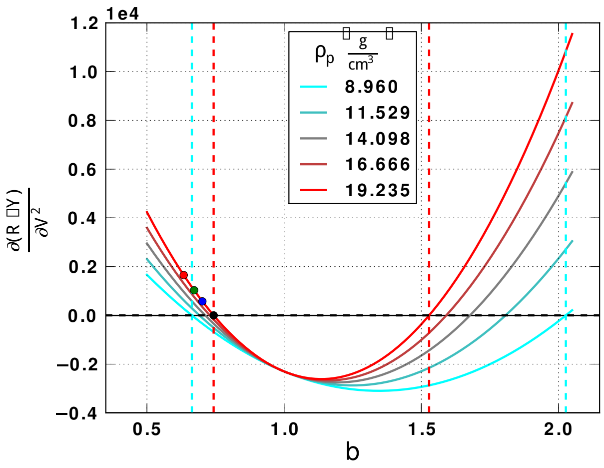

Figure 5.10: Illustration of $\partial(R-Y)/\partial V^2$ over a range of slopes (b) in the linear relationship between penetration velocity and rate of penetration. The lines represent penetrators having a different densities (ρ_p) being used to penetrate sandstone ($\rho_t = 2300$ kg m^{-3}) The region where $\partial(R-Y)/\partial V^2$ is negative and $R-Y$ (Eqn. 5.3) has a maximum is indicated by hatching. The dashed vertical lines indicate transition from the lower (hatched) to upper region (characterised by $R-Y$ having a minimum). The four dots represent different types of penetration: hydrodynamic (black), a 'strengthless' dense water penetrator (blue), tungsten rod using *ZeroStress* as its erosion algorithm (green), and a tungsten rod using *none* as its erosion algorithm (red). These dots correspond to lines of the same colors in Figures 5.11 through 5.13

was simulated for three rods, each having a different material specification, for velocities ranging from 1.5 to 3.9 km/s. Two of the rods used the standard material characterization for tungsten and are only different by use of different erosion algorithms, which where *none* and *ZeroStress* as indicated in the figure legends to follow. The third was intended to approximate penetration by a rod without strength using Uintah's water material model to simulate water with the same density as tungsten. The water model used is unvalidated and not inviscid [15], which may explain some behaviour highlighted in the discussion to follow. For each, a rod with a diameter of 1.5 mm and a length of 0.492 m was used. This length was selected to prevent the onset of secondary penetration phenomena. A line was then fit to the resulting penetration history of each to determine the penetration velocity U. Good agreement with the theory of Orphal and Anderson was produced in comparing the behavior of penetration velocity. Figure 5.11 is a plot of penetration velocity versus initial rod velocity, consistent with Orphal and Anderson's prediction of a linear relationship between penetration velocity and initial rod velocity. As shown in Fig. 5.12, these same penetration velocities, when normalized by the hydrodynamic limit ($U_h = V/(1+(\rho_t/\rho_p)^{\frac{1}{2}})$), approach unity asymptotically from below, which is the expected behavior.

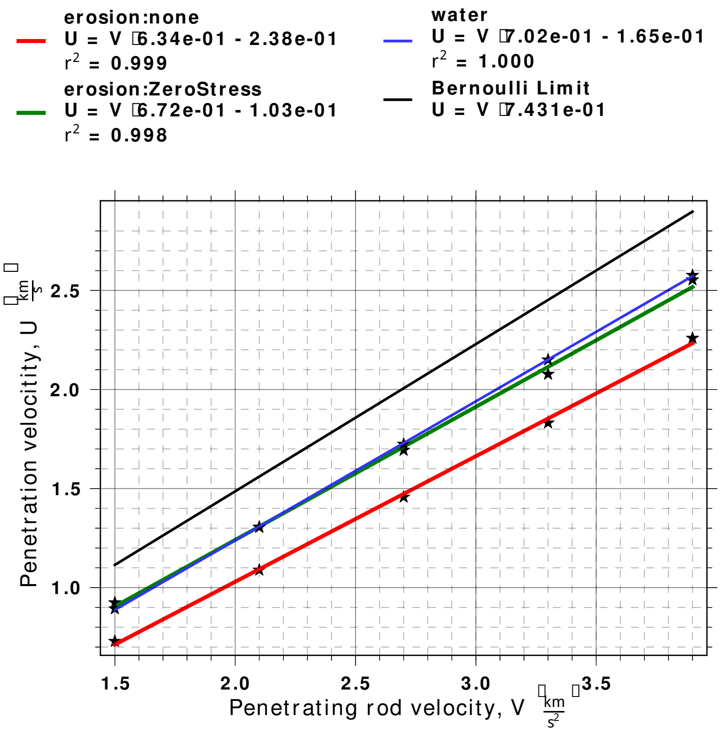

Figure 5.11: Plot of the linear relationship between rate of penetration and penetrating rod velocity. The slope (b), intercept (a), and correlation coefficient (r^2) of each line is indicated in the legend.

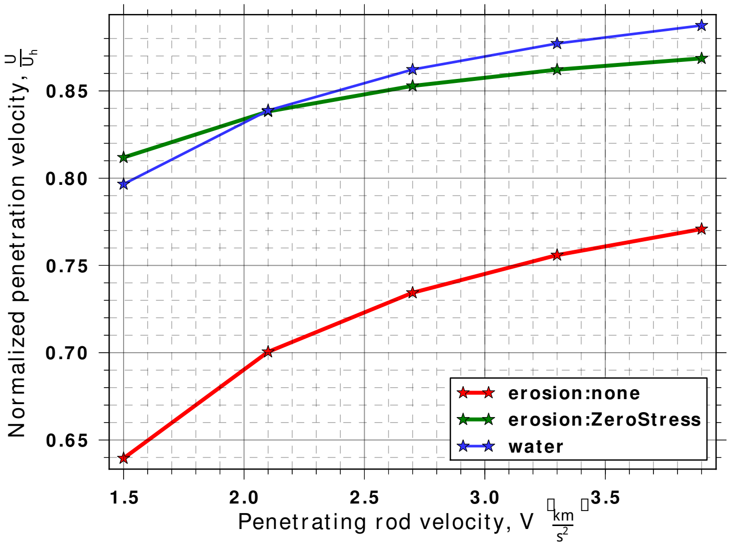

Figure 5.12: Normalized penetration velocity versus penetrating rod velocity. The data of Fig. 5.11 are normalized by the hydrodynamic penetration velocity (U_h, which is the black line in the same figure).

In the legend of Fig. 5.11 are values for the parameters a and b (where a has units of km/s), as well as the correlation coefficient r^2 of the linear fit performed. For the tungsten penetrators, using *none* and *ZeroStress*, b was determined to be 0.634 (red dot in Fig. 5.10) and 0.672 (green dot in Fig. 5.10), respectively, both of which are in the second region of Fig. 5.10 as they are less than the hydrodynamic value of 0.743 (black dot in Fig. 5.10) and therefore expected to experience a minimum at V_m. Using Eqn. 5.4, the predicted values of V_m were all negative. Noting that a negative penetrator velocity is nonphysical, this result precludes confirmation of the predicted minimum. The reported value of b for the dense water penetrator is 0.702 (blue dot in Fig. 5.10) predicting the same behavior as for the tungsten rods, suggesting the possibility that such behavior, if repeatedly observed in future simulations, may be an intrinsic characteristic of porous geologic formations when penetrated within this regime or an indication of a fundamental computational problem. Data to support either claim is currently unavailable. Orphal and Anderson did not have results for materials with both a value of b less than the hydrodynamic value and a value for a less than zero. As indicated previously, mesh refinement was observed to influence the rate of penetration and so specific parameters that depend on this rate (such as a, b, and V_m) can be expected to change until spatial convergence is achieved. Specifically, recalling that rate of penetration increased with mesh refinement, it is suspected that b might increase beyond the hydrodynamic limit. This might result in agreement with the results for other materials, and prediction of a testable value for V_m.

Dynamic strength differences were also calculated for each of the penetrators using Eqn. 5.3 and are presented in Fig. 5.13. Assuming that the dense water represents a penetrator without strength, this value could then be used to determine the dynamic strength of the tungsten penetrators. The dynamic strength difference of the dense water simulation (blue line) was, on average, lowest though it cross the *ZeroStress* simulation (green line) at low velocities, and would therefore predict negative penetrator strengths which is nonphysical, if used in this way. As pointed out earlier though, this model is not inviscid which may explain these results. Further, it is expected that the values of each will change as convergence is achieved and so this is not particularly troubling at this time. It is reccommended that a strengthless model unaffected by viscosity be used in the future, at which point such an analysis should produce both physically realistic values and some insight into the behaviour of sandstone (as modeled) within this loading regime.

A similar investigation was performed to determine the effects of penetrator density on penetration velocity. The same setup and analysis as before was used and the results are

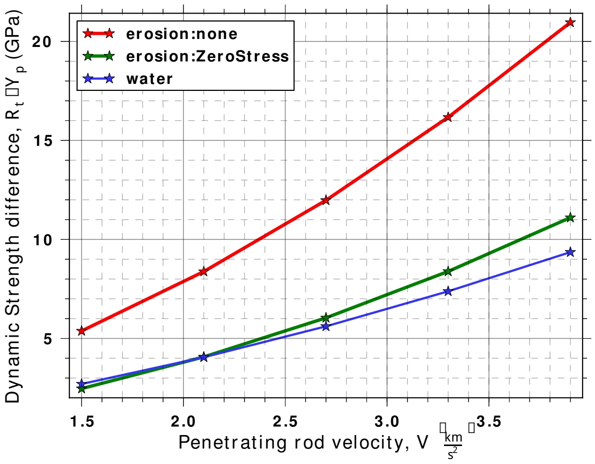

Figure 5.13: Dynamic strength difference $(R - Y)$ versus penetrating rod velocity. The dynamic strength differences were calculated using Eqn. 5.3 and the linear fit of Fig. 5.11 legend.

presented in Fig. 5.14. The expected trend of increasing penetration with density, in a self-similar fashion with hydrodynamic penetration (black line), is observed. Moreover, the results exhibit the expected increase in penetration with decreasing penetrator strength, where the dense water penetrator is closest to hydrodynamic penetration and the line for the tungsten penetrator using erosion option *none* is th furthest from hydrodynamic penetration.

Density effects were further investigated in terms of their impact on the resulting depth of penetration and cavity geometry. The penetrator velocity and diameter were held constant at 3.3 km/s and 3.0 mm, respectively. This was done in order to maintain a total mass, momentum, and energy deposition of 10 g, 33 N s, and 54.5 kJ, respectively. To accomplish this, rod length was varied in inverse proportion to density. Table 5.3 correlates density, length, and penetration results, while Fig. 5.15 is a plot of the same penetration results. In that figure, it is observed (from the impending crossing of the lines) that use of either erosion option would likely predict increasing depth of penetration as density is increased, beyond that of the hydrodynamic value. Partom [72] provides experimental and computational results from a variety of sources that penetration beyond the Bernoulli limit can be attributed to residual penetration associated with kinetic energy of the penetrator's debris after being consumed during the initial penetration event. As this energy increases with density, it is anticipated that penetration might significantly increase in comparison to the value predicted by hydrodynamic theory, which does not account for these secondary penetration effects. The legend presented in Fig. 5.16 will be used repeatedly in following

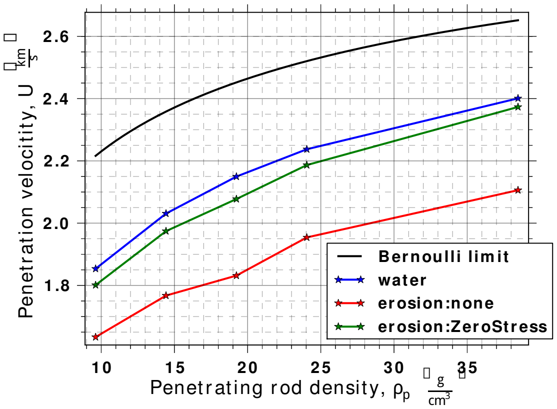

Figure 5.14: Plot of penetration velocity versus penetrating rod density. The black line represents penetration velocity of a Bernoulli penetrator ($U_h = V/(1 + (\rho_t/\rho_p)^{\frac{1}{2}})$).

Table 5.3: Penetrator properties and resulting depth of penetration used to investigate the combined effects of rod density and length. Each row corresponds to a point in Fig. 5.15, a line in Figures 5.17 and 5.18 , and in certain instances an image in Figures 5.19 and 5.20.

Density (g/cm^3)	**Length** (mm)	**Penetration** (cm)		
		none	*ZeroStress*	Hydrodynamic
9.618	147.08	19.08	19.15	30.08
14.426	98.05	17.34	17.07	24.56
19.235	73.54	15.54	15.81	21.27
24.044	58.83	15.03	15.16	19.02
38.470	36.78	14.49	14.86	15.04

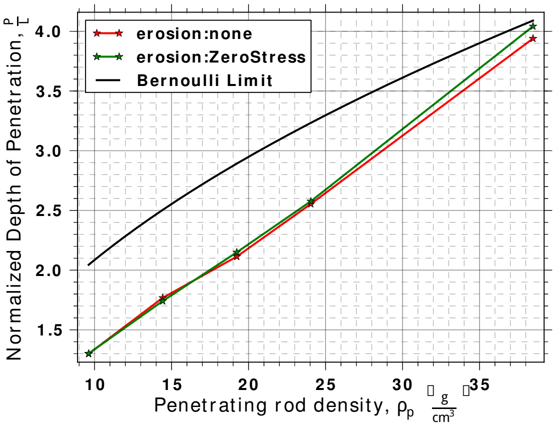

Figure 5.15: Plot of normalized penetration depth versus penetrating rod density. Each line is representing by a column in Table 5.3, while each point corresponds to a row.

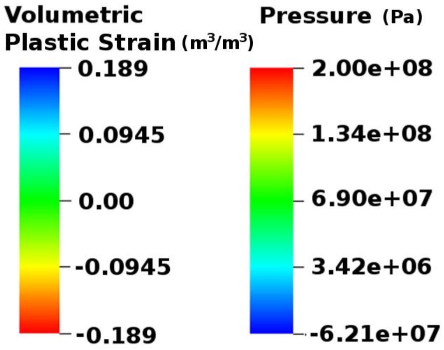

Figure 5.16: Legend for combined plots of volumetric plastic strain and pressure. The pressure limits were selected for their ability to distinguish different overburden values, while also having the ability to capture the shock front. The limits for plastic volumetric strain were selected to indicate the maximum allowable plastic strain in both extension and compression.

presentation and discussion of penetration results in this and the following chapters. Individual penetration histories, rate of penetration histories, and snapshots of each simulation's penetration channel are presented in Figures 5.17 through 5.20.

In comparing the penetration histories of Fig. 5.17, one difference in particular stands out when using the *ZeroStress* erosion option in comparison option *none*. Using *ZeroStress*, there is a clear transition from primary to secondary penetration (for all but the lowest density simulation), as indicated by a decrease in the slope of each line prior to leveling out at a final penetration depth. This same behavior is also evidenced in the rate of penetration history (Fig. 5.18) as a sudden and rapid drop in the rate of penetration followed by a small and brief increase. These same effects are present but do not stand out as clearly in the results obtained using erosion option *none*. Further similarities can be found in comparing the resulting penetration cavities. For instance, the results for a density of ρ_p= 19.235 g/cm^3, for both *none* (Fig. 5.19b) and *ZeroStress* (Fig. 5.20b), exhibit variation in the channel's diameter at similar locations but of differing magnitudes. The cavity at the end of the penetration channel in Fig. 5.19a is the nonphysical result of a kinematic anomaly, discussed in a subsequent chapter.

It is also reported that the resulting channel geometry presented herein for *decreasing* density and *increasing* length (holding mass, momentum, and energy constant), is similar to that observed experimentally by Lach *et al.* [73] for heavy tungsten penetrating hardened steel with *increasing* velocity (energy and momentum are not fixed), though the significance of this is not understood.

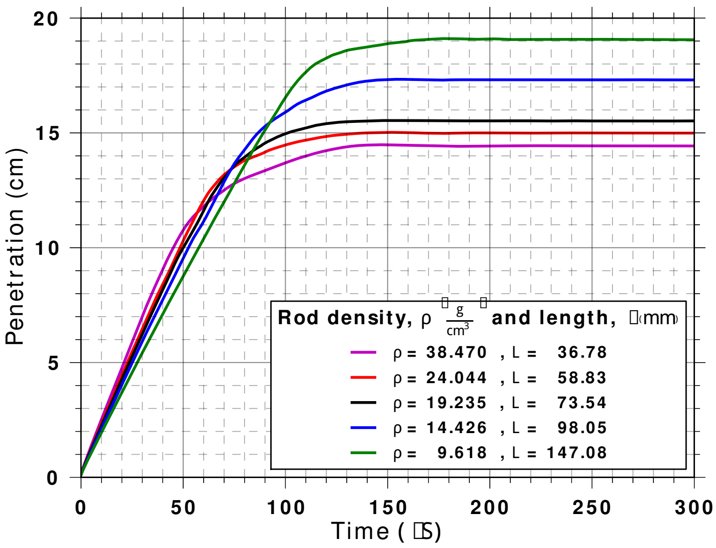

(a) *none*

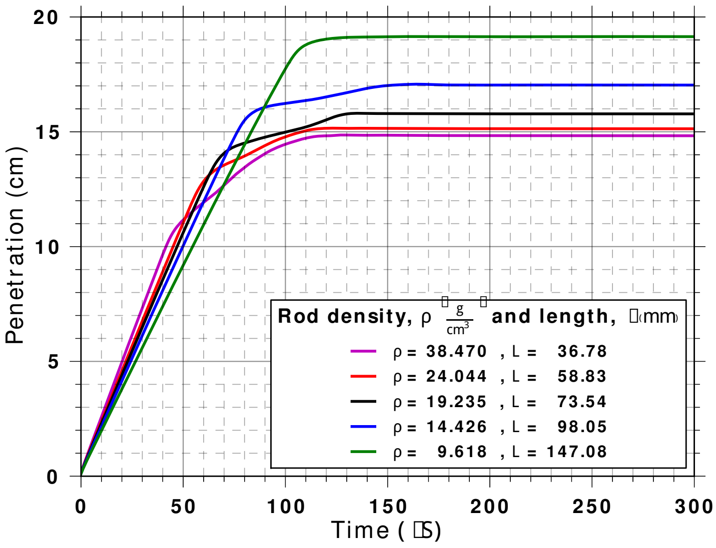

(b) *ZeroStress*

Figure 5.17: Penetration histories for simulations investigating the combined effects of density and length. Each line corresponds to a row in Table 5.3

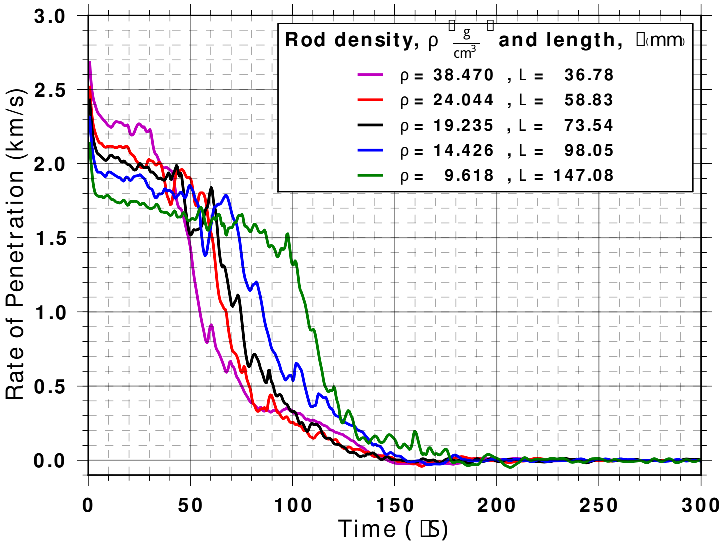

(a) *none*

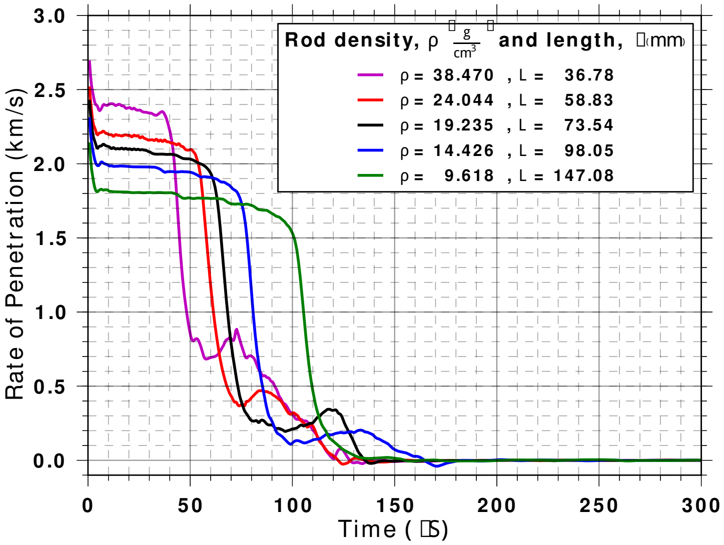

(b) *ZeroStress*

Figure 5.18: Rate of penetration histories for simulations investigating the combined effects of density and length. Each line corresponds to a row in Table 5.3

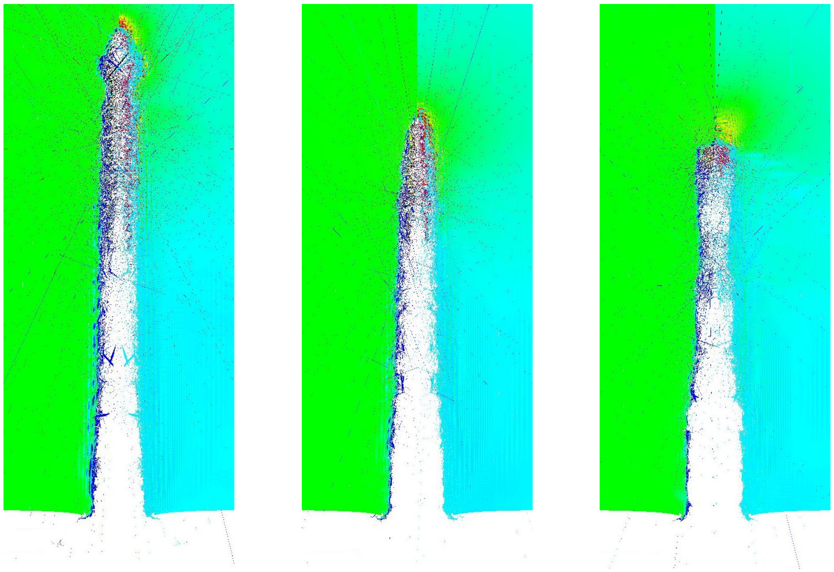
(a) ρ_p=9.618 g/cm^3
L=147.08 mm

(b) ρ_p=19.24 g/cm^3
L=73.54 mm

(c) ρ_p=38.47 g/cm^3
L=36.78 mm

Figure 5.19: Plots of the resulting penetration channel for simulations investigating the combined effects of density and length that used erosion option *none*. Each image corresponds to a row of Table 5.3. Legend in Fig. 5.16.

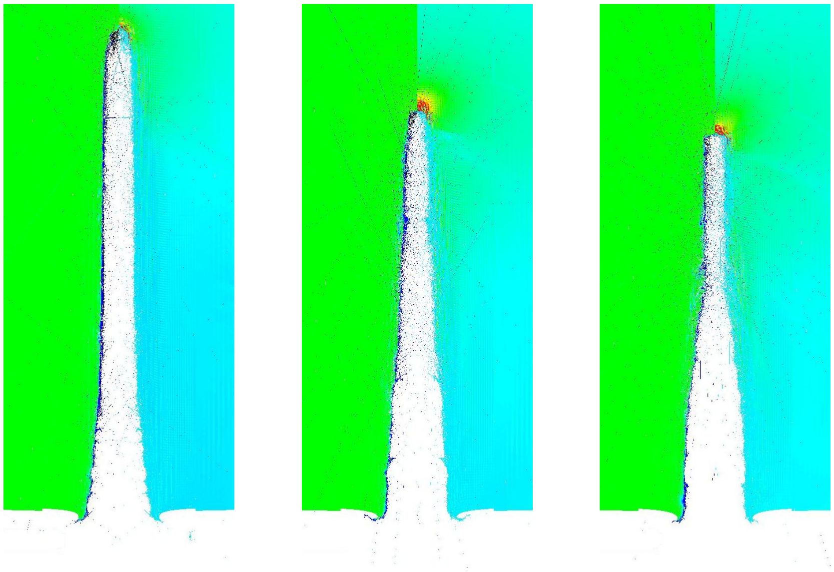
(a) ρ_p=9.618 g/cm^3
L=147.08 mm

(b) ρ_p=19.24 g/cm^3
L=73.54 mm

(c) ρ_p=38.47 g/cm^3
L=36.78 mm

Figure 5.20: Plots of the resulting penetration channel for simulations investigating the combined effects of density and length that used erosion option *ZeroStress*. Each image corresponds to a row of Table 5.3. Legend in Fig. 5.16.

5.3 Simulated Overburden

Throughout the course of this work simulations with confining stress were frequently executed. At first this was done using the discrete jet description. Generally the desired trend was reproduced, for which depth of penetration decreases with increasing confinement. The one exception to this was the unconfined depth of penetration, which was consistently less than the results produced for minimal confinement (*e.g.,* 1 ksi). There were other issues as well, such as observing residual pressures in the area surrounding the penetration cavity, which is discussed in the following chapter. Despite these shortcoming the model was continually tested for its ability to replicate observed trends. One such trend is that for the same hydrostatic pressure (e) found from the axial (σ_{axial}) and radial (σ_{radial}) components of the confining stress by

$$e = \frac{\sigma_{\text{axial}} + 2\sigma_{\text{radial}}}{3} \tag{5.6}$$

that penetration will be increase or decrease respectively, for a hydrostatic stress state with a higher ($\sigma_{\text{axial}} > \sigma_{\text{radial}}$), or lower ($\sigma_{\text{axial}} < \sigma_{\text{radial}}$) axial confinement when compared to isotropic confinement ($\sigma_{\text{axial}} = \sigma_{\text{radial}}$) [74]. To determine whether or not Arenisca had this predictive capability several simulations were executed. The axial, radial, and hydrostatic components of the confining stress for these tests are presented in Table 5.4, and the results are presented in Fig. 5.21. In two of the three cases (for e of 2 and 6 ksi) the expected trend was produced. This is indicated in the figure by the highest point being marked by an upwards triangle indicating a higher axial component, the middle being marked by a right facing triangle denoting an isotropic stress state, and the bottom most marker being a downwards triangle indicating higher radial confinement. For the case of $e = 4$, the depth of penetration for isotropic and higher radial component stress states traded places. Further, the no confinement reference depth of penetration is indicated by the large black circle and is lower than both the isotropic and high axial component stress states for a hydrostatic stress of 2 ksi.

Again as a result of the aforementioned issues associated with using the discrete jet penetrator, it is currently replaced in simulations with overburden, by a long-rod penetrator. The penetrator used is the 19.235 $\mathrm{g\,cm^{-3}}$ of Table 5.3 representing penetration by a solid pure tungsten rod with a length close to that of the collapsed length of the discrete jet. Recently Arenisca's fluid model again became usable providing an opportunity to check two trends, first that penetration depth monotonically decreases with increasing confinement,

Table 5.4: Anisotropic confinement used to obtain the results of Fig. 5.21.

Test number	σ_{axial}	σ_{radial} (ksi)	e
1	4	1	2
2	0	3	2
3	2	2	2
4	8	2	4
5	0	6	4
6	4	4	4
7	10	4	6
8	2	8	6
9	6	6	6

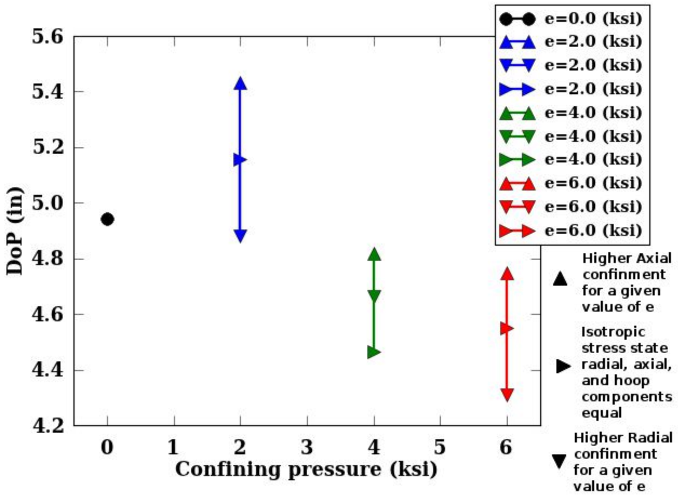

Figure 5.21: Depth of penetration results for simulations having an anisotropic preconfining stress state. Each point corresponds to a row of Table 5.4. An upwards arrow indicates a confining stress state that has a higher axial component, the right facing arrow indicates a stress state was isotropic, and the downwards facing arrow indicates a confining stress state having a larger radial component.

and second that simulations using fluid effects go deeper than those without for the same level of confinement. A summary of the maximum (or as discussed below final) depths of penetration are presented in Table 5.5. These same results are also presented as plots of normalized depth of penetration (P/L) versus confining stress in Fig. 5.22 for both erosion option *none* and *ZeroStress*. In each instance, the set of points were fit to a polynomial, which is the line drawn. Use of *none* (Fig. 5.22a) exhibited a greater degree of scatter, and for the drained case was nonmonotonic for the highest confining stress, though the trend

Table 5.5: Depth of penetration results from simulations of a tungsten rod using different erosion option to penetrate a target with and without fluid effects at differing levels of confinement. Each row corresponds to a line/lines in Figures 5.22 through 5.26 or a figure in Figures 5.27 through 5.30.

Group		**Depth of penetration** (cm)				
		confining stress (ksi)				
erosion − *none*		0	1	5	10	15
	drained	16.58	16.42	15.06	14.91	15.01
	undrained	18.61	17.15	16.70	15.60	15.51
erosion − *ZeroStress*						
	drained	16.69	16.30	15.30	14.89	14.69
	undrained	17.91	17.31	16.19	15.80	15.69

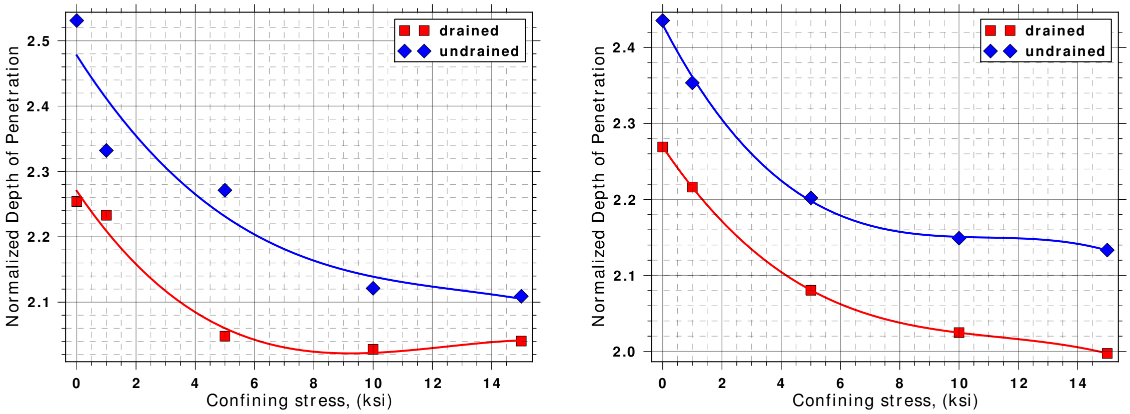

(a) *none*

(b) *ZeroStress*

Figure 5.22: Normalized penetration depth of a rod penetrator penetrating into drained and undrained targets at various levels of preconfinement using different erosion options. The lines in each case represent a polynomial fit to the data points as indicated by the square or diamond markers. Each fit had a correlation coefficient of 0.999 or greater.

of increased depth of penetration when using fluid effects is reported for all levels of confining stress. Using *ZeroStress* (Fig. 5.22b) on the other hand, produced polynomial fits having high correlation coefficients (both greater than 0.9999), and more importantly, both with and without fluid effects, is observed to be monotonically decreasing for increasing confinement. Simulations using the options *ZeroStress* and fluid effects produced the desired trend of increased depth of penetration, over those without fluid effects, for all levels of confinement. In comparing the penetration histories of simulations that use the same erosion and fluid effects options (Figures 5.23 and 5.24), it is observed that steady state penetration is nearly identical, having only minor difference in the time (and as a result the depth of penetration) at which the onset of secondary penetration effects occurs. Further, a separation between high a low confinement results is observed. This effect is particularly well illustrated in Fig. 5.23a where the zero confinement and a confining stress of 1 ksi have similar histories, while confining stresses of 5,10, and 15 ksi cluster together to share similar histories. Figure 5.23b demonstrates the greatest disparity with the preceding observation in that the 5 ksi confinement solution is closer to the 1 ksi solution. Also, for that same group of simulations (erosion option *none* with fluid effects) the no confinement case was run an extra 100 μs before reaching a final depth of penetration, which is the deepest of any group. The same simulation using *ZeroStress* and fluid effects (Fig. 5.24b) exhibited similar prolonged secondary penetration, but as a result of small timestep issues was manually terminated prior to reaching its final depth. Based on its slope at this point, it is hypothesized that it would likely, if able to complete the solution, have had a history similar to the erosion *none* option with fluid effects (Fig. 5.23b). The highest confinement case of the same group (*ZeroStress* with fluid effects) was also manually terminated for the same reasons, but unlike the zero confinement case had already reached its final penetration depth.

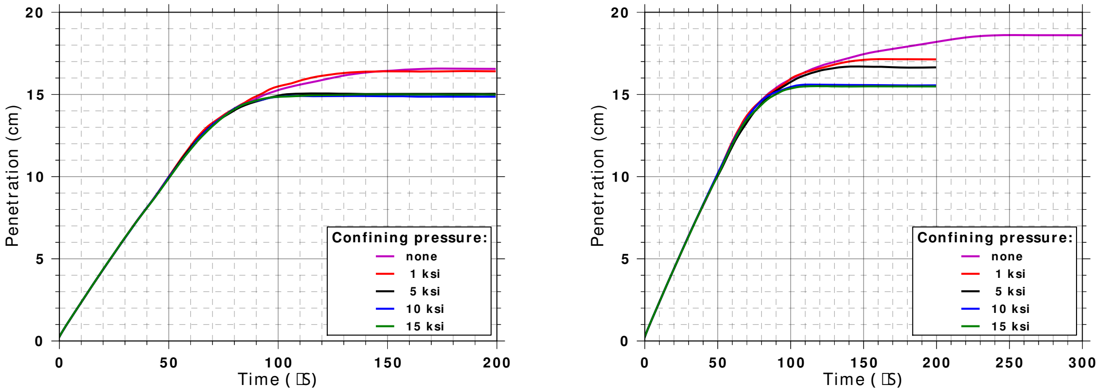

(a) drained

(b) undrained

Figure 5.23: Penetration histories for a tungsten rod penetrator using erosion option *none* to penetrate drained and undrained targets at various levels of preconfinement. The maximum penetration achieved in each history is presented in Table 5.5. Corresponding rate of penetration histories, obtained by numerical differentiation of the lines in this plot, are presented in Fig. 5.25. The final state of each target is presented in Figures 5.27 and 5.28

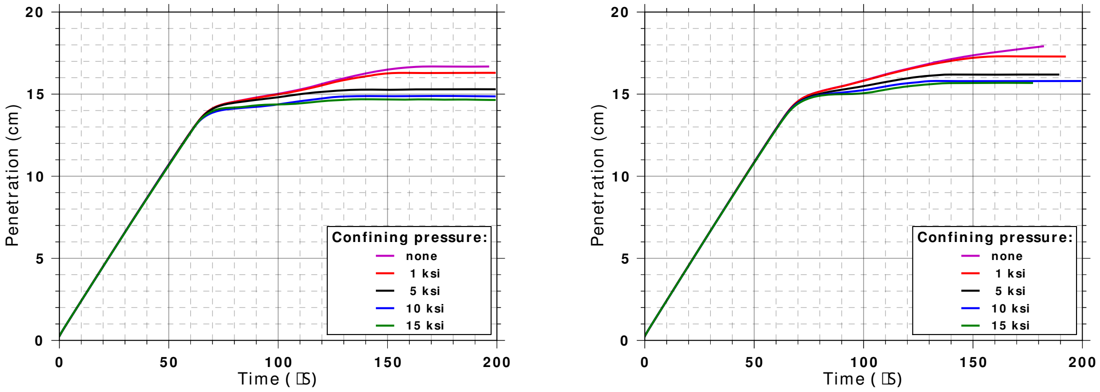

(a) drained

(b) undrained

Figure 5.24: Penetration histories for a tungsten rod penetrator using erosion option *ZeroStress* to penetrate drained and undrained targets at various levels of preconfinement. The maximum penetration achieved in each history is presented in Table 5.5. Corresponding rate of penetration histories, obtained by numerical differentiation of the lines in this plot, are presented in Fig. 5.26. The final state of each target is presented in Figures 5.29 and 5.30

In comparing rates of penetration through time (Figures 5.25 and 5.26) the same observations can be made, namely that the difference between simulations with and without fluid effects is in the nature of terminal penetration phenomena. Further, when using erosion option *none*, the noise in the rate of penetration (resulting from numerical differentiation) is noticeably reduced when incorporating fluid effects (Fig. 5.25b). Resulting channel geometries for each group are compared in Figures 5.27 through 5.30. In comparing the results of erosion option *none* and *ZeroStress* an issues was revealed. During recent migration of kinematics algorithms from within individual constitutive models to a central location within the host code an unintended change was made. As discussed in the following chapter, if the erosion option *ZeroStress* is used, then particle deformation is frozen in time after a particle becomes sufficiently damaged. At the same point in time, the particle is also no longer able to support stress of any kind. When the aforementioned changes were made, the portion of code responsible for freezing a damaged particle deformation was omitted, this resulted in damaged particles undergoing continued and massive deformations, as observed in Figures 5.29 and 5.30. As a result of these simulations this has since been remedied. Focusing now on the results obtained using the erosion option *none* (Figures 5.27 and 5.28), it can be observed that simulations with fluid effects exhibit wider penetration channels with a more rounded tip, this is especially noticeable in comparing Figures 5.27a

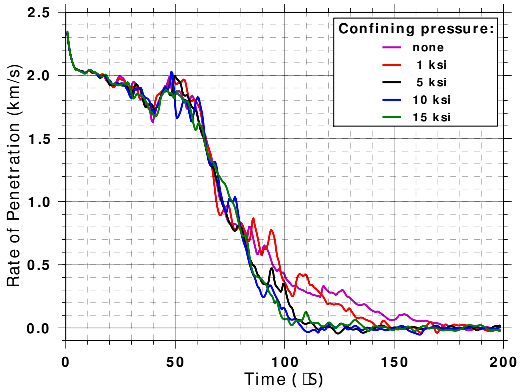

(a) drained

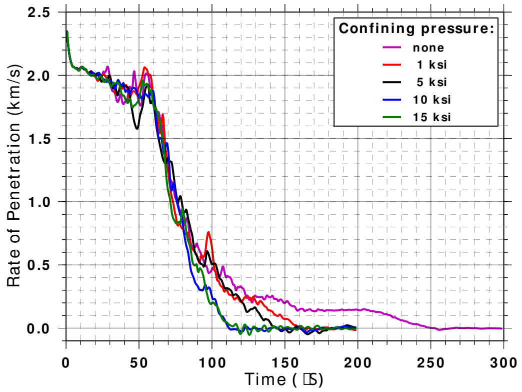

(b) undrained

Figure 5.25: Rate of penetration histories for a tungsten rod penetrator using erosion option *none* to penetrate drained and undrained targets at various levels of preconfinement. Each history was obtained by numerical differentiation of a line in Fig. 5.23.

and 5.28a. Further, the simulations with fluid effects appear to form a shorter and more pronounced slug at the end of the channel, which is particularly evident at lower confining pressures. Higher confining pressure simulations with fluid effects tend to exhibit large residual pressures away from the penetration channel. This phenomena, also presents for simulations using erosion option *ZeroStress* and is the focus of section 6.2 in the following chapter.

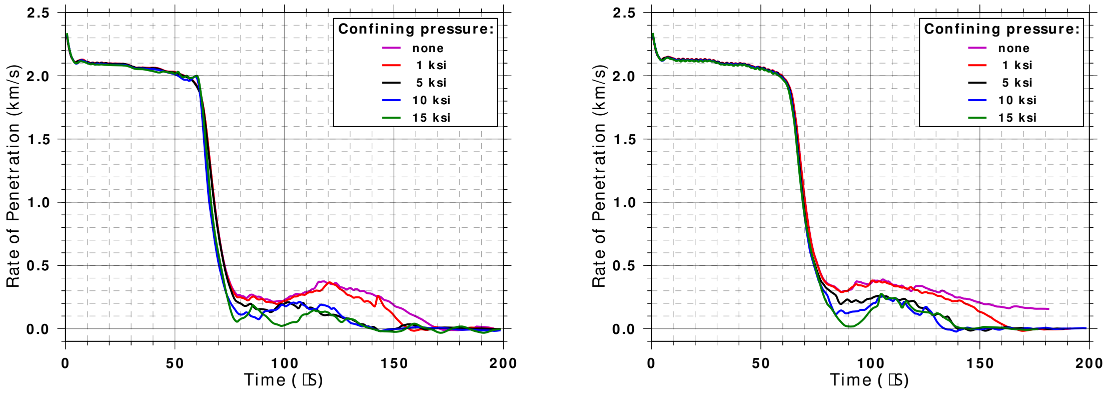

(a) drained

(b) undrained

Figure 5.26: Rate of penetration histories for a tungsten rod penetrator using erosion option *ZeroStress* to penetrate drained and undrained targets at various levels of preconfinement. Each history was obtained by numerical differentiation of a line in Fig. 5.24.

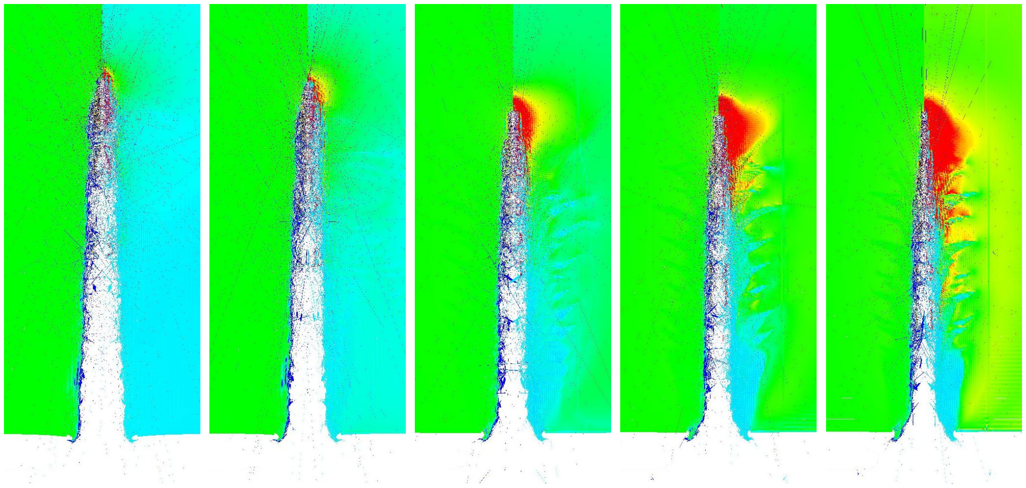

(a) 0 ksi

(b) 1 ksi

(c) 5 ksi

(d) 10 ksi

(e) 15 ksi

Figure 5.27: Plots of the resulting penetration channel for simulations of a tungsten rod penetrator using erosion option *none* to penetrate drained targets at various levels of preconfinement. This set of images correspond to the red line of Fig. 5.22a and a row in Table 5.5. Further, the depth of penetration history that developed each channel is presented in Fig. 5.23a, and a corresponding plot of the rate of penetration in Fig. 5.25a. Legend in Fig. 5.16.

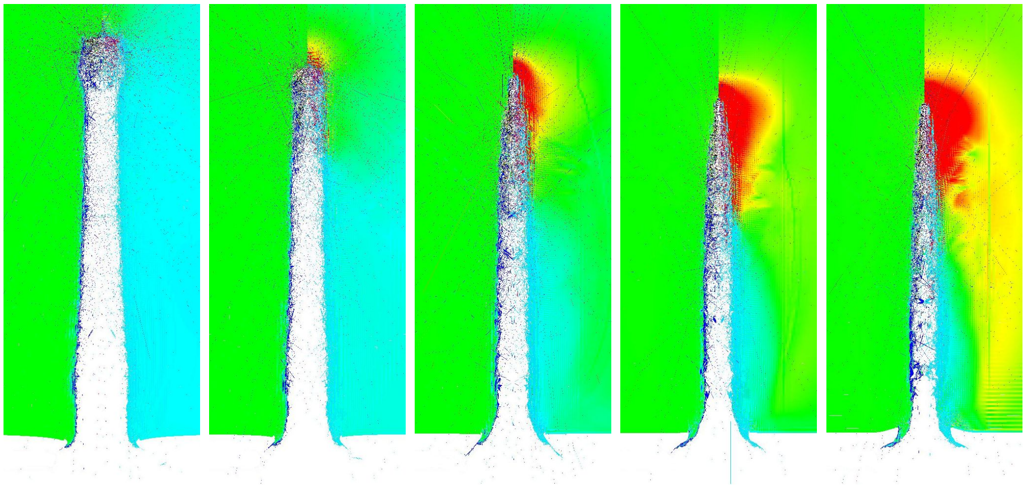
(a) 0 ksi (b) 1 ksi (c) 5 ksi (d) 10 ksi (e) 15 ksi

Figure 5.28: Plots of the resulting penetration channel for simulations of a tungsten rod penetrator using erosion option *none* to penetrate undrained targets at various levels of preconfinement. This set of images correspond to the blue line of Fig. 5.22a and a row in Table 5.5. Further, the depth of penetration history that developed each channel is presented in Fig. 5.23b, and a corresponding plot of the rate of penetration in Fig. 5.25b. Legend in Fig. 5.16.

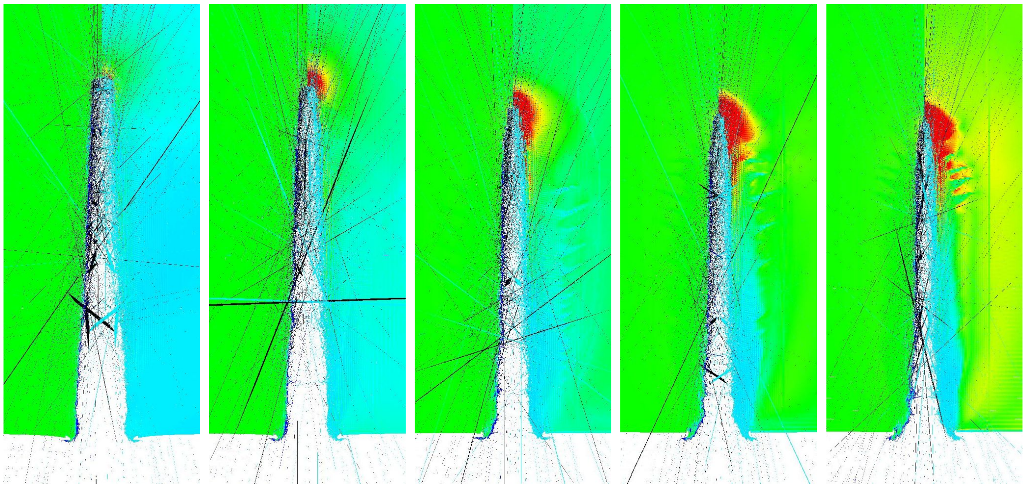
(a) 0 ksi (b) 1 ksi (c) 5 ksi (d) 10 ksi (e) 15 ksi

Figure 5.29: Plots of the resulting penetration channel for simulations of a tungsten rod penetrator using erosion option *ZeroStress* to penetrate drained targets at various levels of preconfinement. This set of images correspond to the red line of Fig. 5.22b and a row in Table 5.5. Further, the depth of penetration history that developed each channel is presented in Fig. 5.24a, and a corresponding plot of the rate of penetration in Fig. 5.26a. Legend in Fig. 5.16.

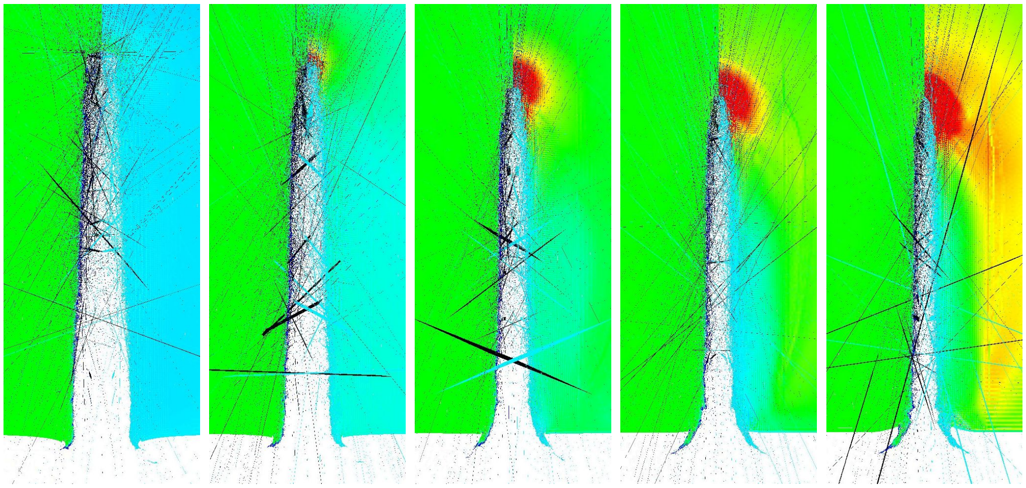

(a) 0 ksi (b) 1 ksi (c) 5 ksi (d) 10 ksi (e) 15 ksi

Figure 5.30: Plots of the resulting penetration channel for simulations of a tungsten rod penetrator using erosion option *ZeroStress* to penetrate undrained targets at various levels of preconfinement. This set of images correspond to the blue line of Fig. 5.22b and a row in Table 5.5. Further, the depth of penetration history that developed each channel is presented in Fig. 5.24b, and a corresponding plot of the rate of penetration in Fig. 5.26b. Legend in Fig. 5.16.

CHAPTER 6

ISSUES EXPOSED BY V&V

This chapter describes a number of unexpected results that were revealed through verification and validation testing. These results at times pointed to fundamental issues for which simple litmus tests exist, and for which solutions are actively being developed, while others have been problematic in that currently they can be neither explained nor resolved.

6.1 Locking

As a result of improved visualization techniques (refer to section 5.1.1), one characteristic symptom of locking (checkerboarding of solution fields) was identified in many simulation results, and is demonstrated in Fig. 6.1. Locking is defined by Mast [75] as 'the build-up of fictitious stiffness due to an element's/cell's inability to reproduce correct deformation mode shapes. The end result is a system that is too stiff, leading to poor kinematics and erroneous strains.' Two common forms of locking inherited by MPM from FEM are volumetric and shear locking. Locking can significantly affect problem convergence, and so is a serious concern where high computational overhead is already an issue. Having identified a symptom of locking, testing to confirm the presence and prevalence of locking within the Uintah framework was undertaken and is the focus of this section. As a result of this work, development of antilocking methods is now a project objective.

6.1.1 Shear Locking

Shear locking results when element interpolation functions are unable to accurately approximate the strain distribution associated with bending. The name shear locking stems from the large unphysical shear strains found in bent elements susceptible to this form of locking [76, 75]. Stiffness is also noted to increase anomalously with the aspect ratio of an element [77] (*e.g.,* in an axisymmetric 2-d simulation the aspect ratio of a particle/cell is the ratio of its edge lengths). Common indicators of shear locking are the

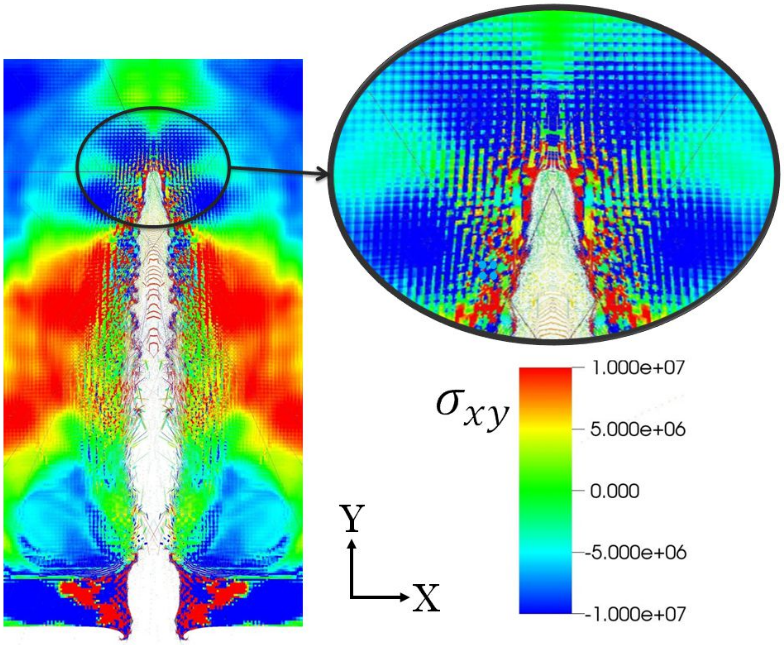

Figure 6.1: Example of the characteristic checkerboarding of solution fields that presents in locking phenomena.

aforementioned presence of checker boarding in solution fields – particularly in the shear components of stress – and slow solution convergence, both of which were identified in penetration simulations. Massively sheared high-aspect-ratio particles have also frequently been observed in simulating the perforation/penetration process. If possible, sufficient mesh refinement should significantly improve solution accuracy, though this convergence is often characterized by a sudden change in the rate of convergence (i.e., a bilinear convergence plot); no theory yet exists for predicting the threshold value of mesh size at which the rate of convergence suddenly improves. Unconventional integration schemes like those described by Bower [76] have been effective at countering this problem in FEM, and strain regularization techniques like those described by Mast [75] have been effective in MPM. Despite previous work being able to accurately capture penetration into aluminum targets using a different material model [30], the degree to which locking plays a deleterious role in Arenisca simulations remains unclear. For this reason the simple bending beam problem proposed by Mast [75] was solved using Uintah and its basic NeoHookean elastic material model; this was done to confirm the presence of shear locking and better understand its pervasiveness within this framework.

The problem solved is that of an elastic cantilever beam subjected to an initial velocity field corresponding to the first mode of free vibration, this problem is illustrated in Fig.

6.2. Both a more in depth explanation of the problem setup and shear locking is provided by Mast in [75]. Shear locking is reported to be a problem predominantly in using linear interpolators (which are usually selected for their high efficiency, algorithmic simplicity, and ability to avoid negative values of field interpolation in high gradient problems) [75, 77]. For this reason, different interpolators were used to describe fields on the background grid, and their respective performances were evaluated. These interpolators are listed in Table 6.1 and include single point integration which uses the linear shape functions inherited from FEM, the generalized interpolation material point (GIMP [21]) method, which uses smooth differentiable support functions over the initial domain of a particle, the convected particle domain interpolation (CPDI [24]) method, which accounts for the evolving extents of a particle as it deforms using a 4-node FEM interpolation over this domain, and B-Splines, which provide smoother gradients over a greater support domain than linear shape functions [78]. Each of these interpolation methods, other than single point integration, is meant to counteract the cell crossing and/or tensile instability inherent to most basic formulation of MPM.

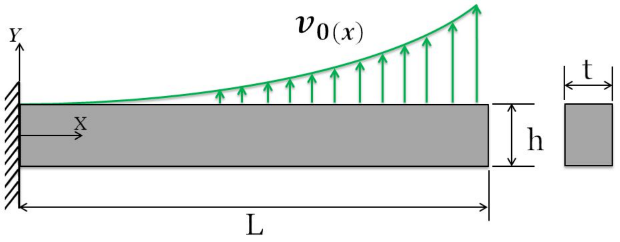

Parameter	**Value** (m)
L	10
h	1
t	1

Figure 6.2: Shear locking benchmark problem illustration. The initial velocity field of a cantilever beam undergoing the first mode of free vibration, $V_0(x)$, is applied to a cantilever beam of length L, height h, and thickness t.

Table 6.1: Shear locking problem interpolators.

Interpolator	**Description**
Single point integration	Effectively a lumped mass solution.
GIMP	Accounts for the initial spatial extent of particles.
CPDI	Accounts for deforming particles by using different shape functions.
3^{rd} order B-Spline	Like GIMP, uses higher-order B-spline shape functions.
4^{th} order B-Spline	Like GIMP, uses higher-order B-spline shape functions.

The above problem was executed at three background grid cell sizes consistent with the work of Mast, which are 1.0, 0.5, and 0.25 m, respectively. Each resolution was further carried out at two amplitudes: large displacement with associated high bending stress and small displacement with low bending stress. The aim was to determine if the resultant error was a combination of shear locking and the cell crossing instability as described by Bardenhagen and Kober [21]. Shear locking was found to be present at all resolutions, for both amplitudes, using all interpolators, though solution quality does appear marginally improved at higher resolutions using high-order B-spline interpolators. This result indicates that shear locking is unrelated to the cell-crossing instability, and therefore a currently unresolved concern even in quasistatic problems.

The single-point integration interpolator simulations often failed to run to completion, with the code reporting a negative Jacobian. Given the small deformations of this test problem, such an error was unexpected and not yet understood. The earliest simulation failure occurred at the 25^{th} of 24,000 steps. For this reason, the comparisons of interpolators in this section are all evaluated at this point in time. The axial-lateral (σ_{xy}) shear stress component results very early in the solution for each resolution of the large-displacement problem specification are presented as Fig. 6.3.

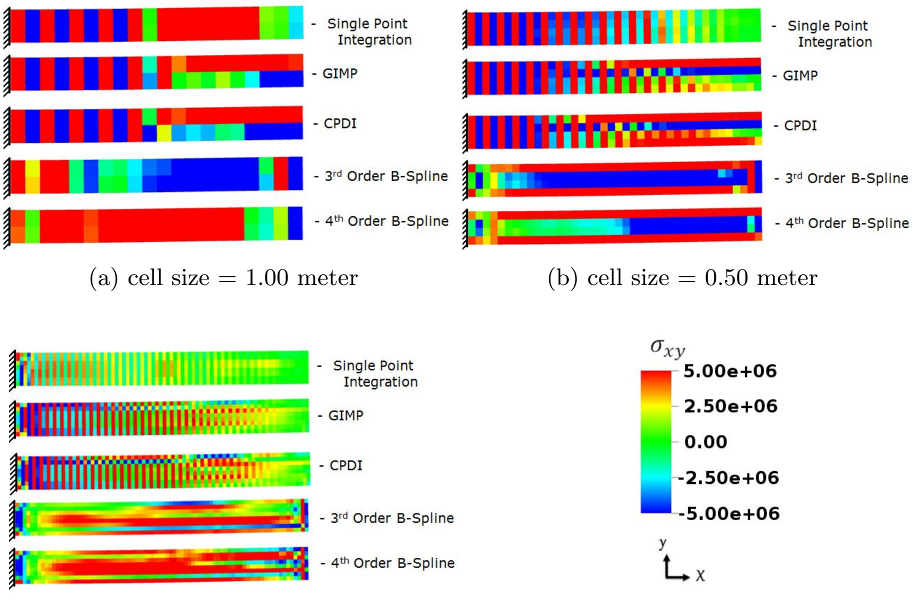

(a) cell size = 1.00 meter (b) cell size = 0.50 meter

(c) cell size = 0.25 meter

Figure 6.3: Shear locking benchmark problem results. Plots of shear stress σ_{xy}. Each has a particle resolution of 2 per direction per cell.

Though the high-order B-spline interpolators appear less susceptible to shear locking, they too produce nonphysical discontinuous fields at later stages of the solution.

Uintah is currently equipped with a basic strain regularization method to counteract volumetric locking like that of Mast *et al.* [75]. Though this method is not expected to be particularly effective for the case of shear locking, the effect of this feature was investigated. Results using this strain regularization method are presented as Fig. 6.4. Use of the strain regularization method was found to be ineffective at combating the effects of shear locking, producing no visible changes in the checkerboarding of shear stress.

Upon closer inspection it was found that, for all interpolators, energy was not conserved. Further, the use of strain regularization worsened this problem resulting in rapid energy loss. These effects, presented in Fig. 6.5, are more pronounced when using both strain regularization and a high-order B-spline interpolator. The reasons for this behavior are not currently well understood.

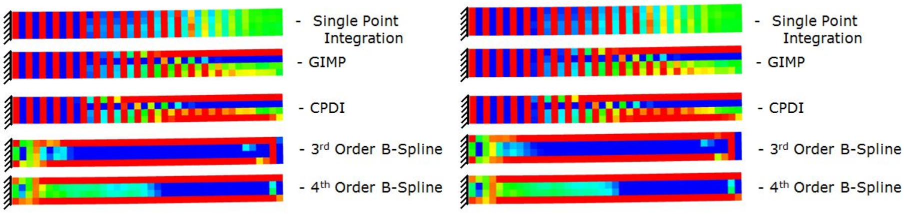

(a) without regularization

(b) with regularization

Figure 6.4: Shear locking benchmark problem results comparing the effects of basic strain regularization. Each is for the 0.50 m resolution and uses the legend of Fig. 6.3

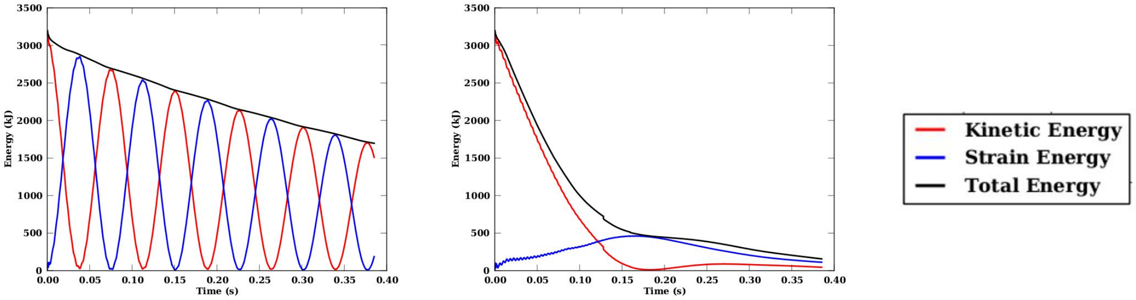

(a) without regularization

(b) with regularization

Figure 6.5: Energy versus time for a third order B-spline interpolator solving the cantilever beam shear locking problem.

6.1.2 Volumetric Locking

Similar to shear locking, volumetric locking is also the result of the interpolating function being unable to accurately approximate physical phenomena, in this case the interpolation is unable to approximate volume-preserving strain fields [76]. Traditionally, volumetric locking has been a more serious issue than shear locking in FEM, as it cannot be resolved with increasing mesh refinement. The solution in FEM again is to use modified integration schemes like those described by Bower [76], in MPM the methods of Mast *et al.* [75] have proven effective at improving simulation results where volumetric locking plays a dominant role. Mast proposed using the same problem to test for both volumetric and shear locking. However, because that problem is slow to solve, and because there was a desire to concurrently test other features crucial to penetration problems (2-d axisymmetry and pressure boundary conditions), a different benchmark problem was selected. Namely, a linear-elastic thick-walled cylinder is subjected to plane strain by application of an externally applied pressure, as described by Bower for traditional FEM [76]. This problem is illustrated in Fig. 6.6.

Volumetric locking occurs as material properties approach incompressibility, which is achieved in the limit as the Poisson ratio of a material approaches one half ($\nu \rightarrow 0.5$). The two material input parameters, bulk modulus (K) and shear modulus (G), were independently varied to achieve each desired Poisson ratio by means of

$$\nu = \frac{3K - 2G}{2(3K + G)} \tag{6.1}$$

Both elastic moduli were initially set to have values similar to aluminum ($K = 70.28$

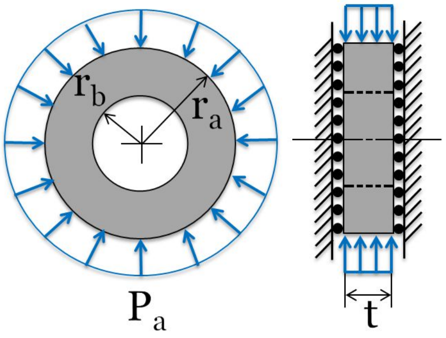

Parameter	Value
r_a	0.5 m
r_b	0.2 m
t	0.1 m
P_a	6.895 MPa (1.0 ksi)

Figure 6.6: Volumetric locking benchmark problem illustration. The pressure P_a is applied at the outer surface of the thick walled cylinder described by an outer radius r_a, inner radius r_b, and thickness t. The problem solved is plane strain using a linear elastic constitutive model.

MPa, $G = 26.23$ MPa, and $\nu = 0.334$). This baseline material specification was selected as it is well parameterized, in the middle of the range of ν's to be tested, and is expected to converge with mesh refinement. The specific material parameters tested are listed in Table 6.2.

Computed radial particle displacements were compared directly to the analytical displacements (δ_r). These analytical displacements were obtained using the circumferential-strain solution in Eqn. 6.2 and the strain-displacement relationship in Eqn. 6.3 as provided by Bower [76].

$$\epsilon_{\theta\theta}(r) = \frac{P_a r_a^2(\nu - 1)(r_b^2 + r^2(1 - 2\nu))}{3r^2K(1 - 2\nu)(r_a^2 - r_b^2)} \tag{6.2}$$

$$\delta_r(r) = r\epsilon_{\theta\theta} \tag{6.3}$$

The absolute L_2 error norm over the simulation domain was then computed as

$$L_2 = \sqrt{\frac{\sum\limits_{p=1}^{N} \left(\delta_s(r_p) - \delta_e(r_p)\right)^2}{N}} \tag{6.4}$$

where N is the number of particles in the simulation, r_p is the radius at particle p's center, and δ_s and δ_e are the simulation and analytical radial displacements, respectively. This

Table 6.2: Material properties for volumetric locking test. Table (a) varies the bulk modulus (K) to achieve different values for Poisson's ratio using Eqn. 6.1, while (b) achieves the same end by varying shear modulus (G).

(a) G =26.230 GPa

ν	K (GPa)
0.1000	24.044
0.1500	28.728
0.2000	34.973
0.2500	43.717
0.3000	56.832
0.3340	70.280
0.3500	78.690
0.4000	122.41
0.4500	253.56
0.4950	261.43
0.4990	1310.6

(b) K =70.280 GPa

ν	G (GPa)
0.1000	76.669
0.1500	64.169
0.2000	52.710
0.2500	42.168
0.3000	32.437
0.3340	26.230
0.3500	23.427
0.4000	15.060
0.4500	7.270
0.4950	0.727
0.4990	0.141

error norm was used to compare solution accuracy at a given mesh resolution, as well as to establish the presence of convergent behavior with increasing mesh refinement. According to ASME [33] the rate of convergence can be obtained by comparison of multiple computational solution results, each using different levels of discretization. For each Poisson's ratio, linear regression [79] was applied to fit the log of error versus the log of the number of particles. The fitted slope, m, is the rate of convergence. The correlation coefficient r^2 (is a measure of how well the linear fit represents the data) was also computed for each fit. Table 6.3 and Figures 6.7 and 6.8 are the results obtained by varying the bulk modulus. Table 6.4 and Figures 6.9 and 6.10 are the results as obtained by varying the shear modulus. While volumetric locking is typically associated with incompressibility by means of a large bulk modulus, these results indicate that a small shear modulus has a significantly greater influence on error across a greater range of ν's. Error increases at both ends of the spectrum when varying the bulk modulus, while by varying the shear modulus causes a nearly monotonic increase in error with increasing values of ν. On average, a rate of convergence of 0.30 was achieved by varying the bulk modulus; a much lower average of 0.07 was achieved by varying the shear modulus. In both cases, a number of poor linear fits were obtained, as seen by some low correlation coefficients in Table 6.3a and Table 6.4a.

The previously discussed basic strain regularization algorithm was also applied to the volumetric locking problem. In this instance, strain regularization was largely effective at counteracting the volumetric locking phenomena. All modified bulk modulus exhibited a decrease in error (Fig. 6.7b) and became convergent (Fig. 6.8b).

Table 6.3: Convergence rates (m) and corresponding correlation coefficients (r^2) for the 2-d volumetric locking problem varying Poisson's ratio (ν) by means of the bulk modulus (K).

(a) without strain regularization

ν	m	r^2
0.1000	$+4.6884 \times 10^{-3}$	0.9474
0.1500	$+2.7525 \times 10^{-2}$	0.9270
0.2000	$+2.2748 \times 10^{-2}$	0.0039
0.2500	-3.9798×10^{-1}	0.9972
0.3000	-1.1055×10^{-1}	0.8455
0.3340	-2.1325×10^{-1}	0.9669
0.3500	-1.3578×10^{-1}	0.9252
0.4000	-2.5741×10^{-1}	0.9843
0.4500	-5.4268×10^{-1}	0.9992
0.4950	-7.4141×10^{-1}	0.9352
0.4990	-8.6783×10^{-1}	0.9995

(b) with strain regularization

ν	m	r^2
0.1000	-1.4261×10^{-1}	0.9125
0.1500	-2.6914×10^{-1}	0.9599
0.2000	-5.1146×10^{-1}	0.9978
0.2500	-9.1558×10^{-1}	0.9730
0.3000	-9.5649×10^{-1}	0.9631
0.3340	-7.5995×10^{-1}	0.9862
0.3500	-6.7305×10^{-1}	0.9950
0.4000	-5.3119×10^{-1}	0.9999
0.4500	-5.0339×10^{-1}	0.9993
0.4950	-5.3690×10^{-1}	0.9999
0.4990	-5.3910×10^{-1}	1.0000

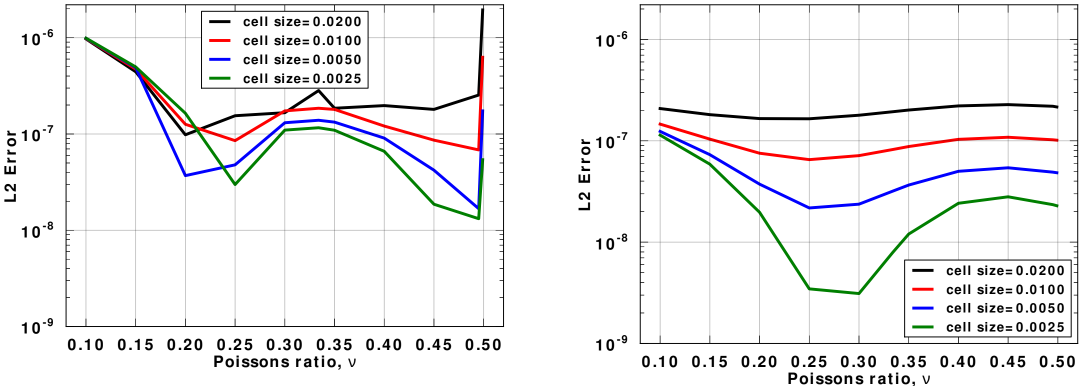

(a) without strain regularization

(b) with strain regularization

Figure 6.7: Error plots for 2-d volumetric locking problem varying Poisson's ratio (ν) by means of the bulk modulus (K).

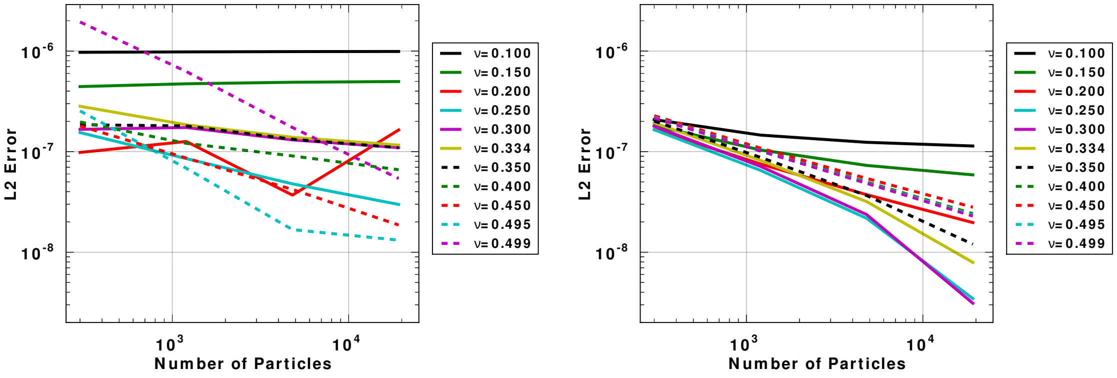

(a) without strain regularization

(b) with strain regularization

Figure 6.8: Convergence plots for 2-d volumetric locking problem varying Poisson's ratio (ν) by means of the bulk modulus (K).

Table 6.4: Convergence rates (m) and corresponding correlation coefficients (r^2) for 2-d volumetric locking problem varying Poisson's ratio (ν) by means of the shear modulus (G).

(a) without strain regularization

ν	m	r^2
0.1000	-6.4836×10^{-2}	0.1688
0.1500	-1.9781×10^{-3}	0.0002
0.2000	-9.1563×10^{-2}	0.0817
0.2500	-8.5804×10^{-1}	0.9838
0.3000	-1.8949×10^{-1}	0.9889
0.3340	-2.1325×10^{-1}	0.9669
0.3500	-1.5560×10^{-1}	0.9502
0.4000	$+1.2907 \times 10^{-1}$	0.8505
0.4500	$+7.8433 \times 10^{-1}$	0.6037
0.4950	$+6.1927 \times 10^{-2}$	0.7520
0.4990	$+1.2142 \times 10^{-2}$	0.7590

(b) with strain regularization

ν	m	r^2
0.1000	-6.5957×10^{-1}	0.9481
0.1500	-8.0607×10^{-1}	0.9901
0.2000	-5.2876×10^{-1}	0.9987
0.2500	-4.5464×10^{-1}	0.9954
0.3000	-5.3294×10^{-1}	0.9998
0.3340	-2.1325×10^{-1}	0.9669
0.3500	-8.7044×10^{-1}	0.9705
0.4000	-3.3151×10^{-1}	0.9839
0.4500	$+2.9348 \times 10^{-1}$	0.8491
0.4950	$+9.9767 \times 10^{-4}$	0.9216
0.4990	$+1.7599 \times 10^{-4}$	0.8827

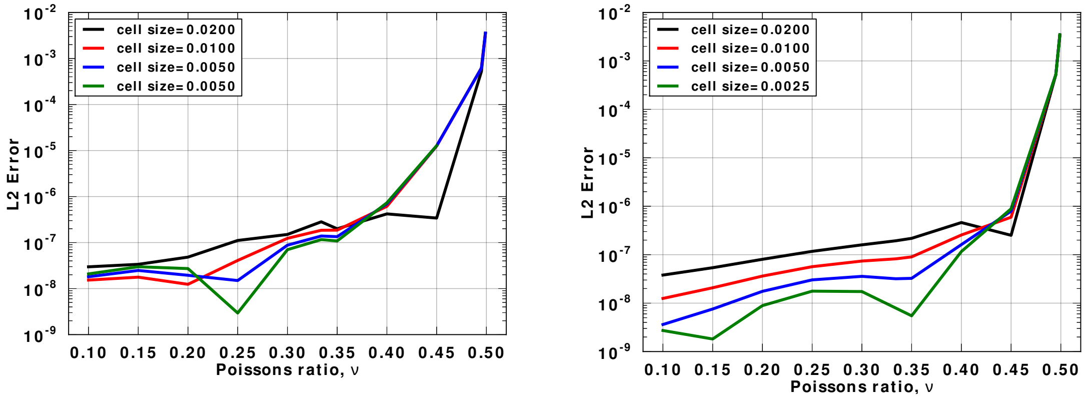

(a) without strain regularization

(b) with strain regularization

Figure 6.9: Error plots for 2-d volumetric locking problem varying Poisson's ratio (ν) by means of the shear modulus (G).

These same tests also had largely improved linearity (r^2), with an improved average rate of convergence of 0.5 (Table 6.3b). The modified shear modulus tests behaved similarly (Fig. 6.9b), though the three highest values of Poisson ratio remain borderline divergent (Fig. 6.10b). The modified shear modulus tests also exhibited improvment in linearity (r^2) with the average rate of convergence improving to a value of 0.49 (Table 6.4b).

To assess the axisymmetric implementation, these same tests were run again, this time in full 3-d. As a result of the significantly increased computational cost associated with

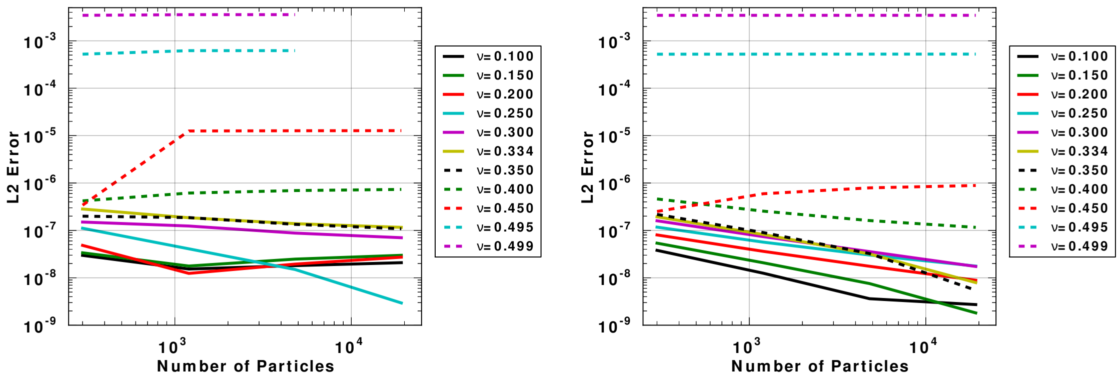

(a) without strain regularization

(b) with strain regularization

Figure 6.10: Convergence plots for 2-d volumetric locking problem varying Poisson's ratio (ν) by means of the shear modulus (G).

an increase in the dimensionality of the problem, fewer tests were executed. The results mimicked those as obtained using axisymmetry and are presented as Fig. 6.11 and Fig. 6.12 for modified bulk and shear modulus tests, respectively. It is not surprising that the error, while having the same profile when plotted against Poisson's ratio, is noticeably increased. This is believed to be due to the fact that the pressure boundary condition in the 3-d implementation is not exact, while it is in the 2-d formulation. Work is underway to take advantage of the particle domain information available when using the convected particle domain method [80] in order to improve the pressure boundary condition in 3-d.

While improvement for this particular benchmark problem is observed when using basic strain regularization, this is not universally true. In observing the effects of the basic strain regularization on manufactured solution problems, an overall increase in error is reported (Fig. 6.13). This is not surprising as a result of the accumulative averaging of a cell's strain performed at each step. For this reason, the basic strain regularization is recommended only when volumetric locking is expected to exist.

6.2 Residual Pressures

In simulations with preconfining stress high residual pressures were observed along the penetration channel walls (Fig. 6.14a). This pressure is the combined effect of large stresses in each of the principal directions (radial, axial, and circumferential), and does not reduce to zero at the cavity's edge. In particular, the normal component of stress is not zero. As the boundary of the penetration channel is effectively a free surface, this is not the expected

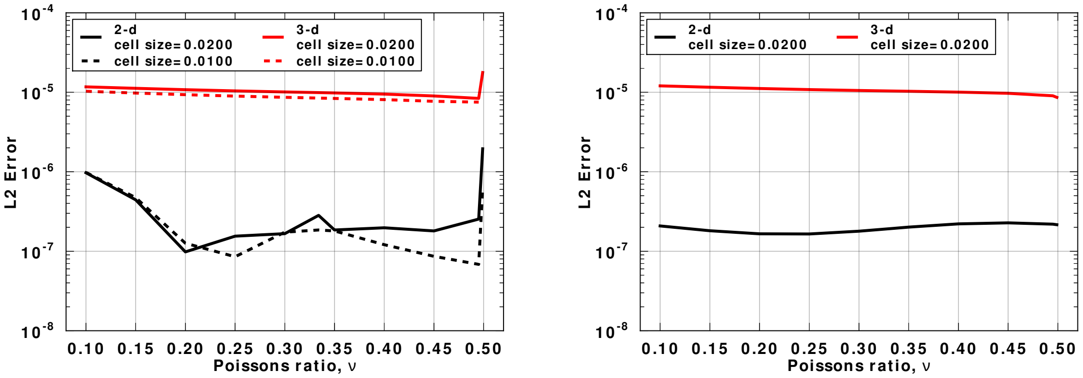

(a) without strain regularization

(b) with strain regularization

Figure 6.11: Error plots for 2-d volumetric locking problem varying Poisson's ratio (ν) by means of the bulk modulus (K).

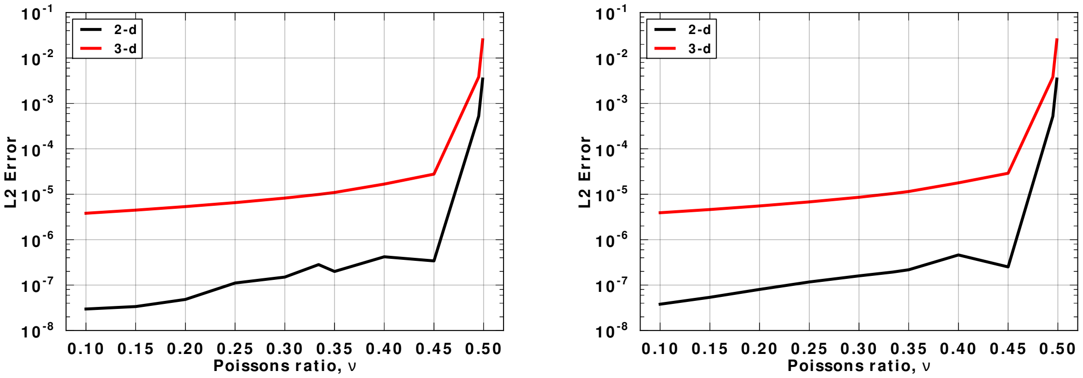

(a) without strain regularization

(b) with strain regularization

Figure 6.12: Error plots for 2-d and 3-d volumetric locking problem varying Poisson's ratio (ν) by means of the shear modulus (G).

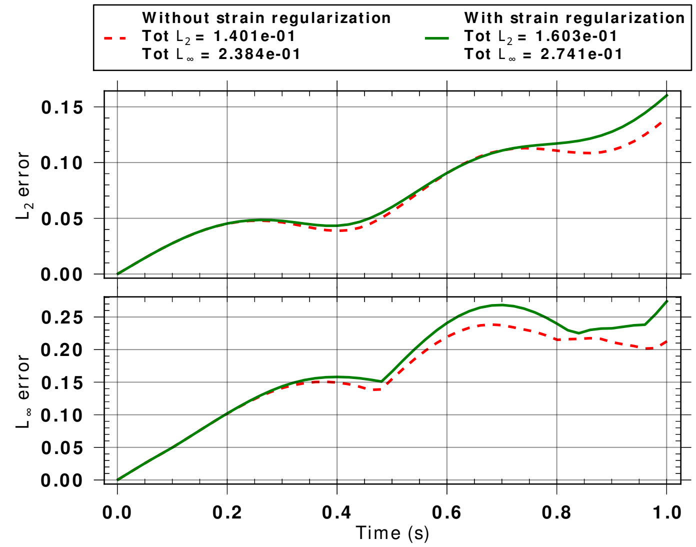

(a) Generalized vortex MMS problem of [27]

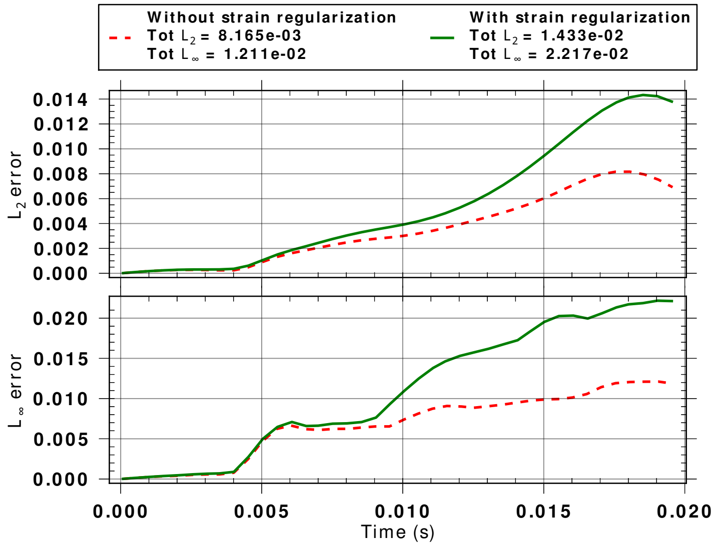

(b) Axis-aligned displacement MMS problem of [22]

Figure 6.13: Comparison of manufactured solution problems with and without basic strain regularization enabled.

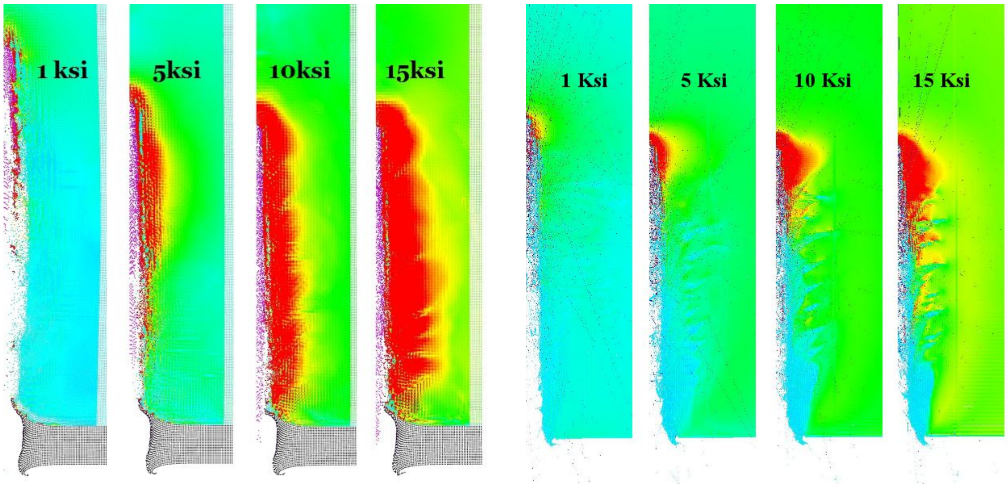

(a) Previous version of Arenisca

(b) Newest version of Arenisca

Figure 6.14: Residual pressure along the penetration cavity walls. Using the older version of Arenisca the discrete jet description was used, also the jet and steel material in this image are not colored by pressure. Using the newest version a long-rod penetrator was used and a small hole was placed in the pressure boundary condition as discussed above. In both instances an unspected residual pressure field results. Pressure legend in Fig. 5.16

result.

One possible explanation is that the jet material acts to clog the channel, thus making the penetration channel's surface in fact *not* a free surface and thereby preventing full elastic relaxation of the surrounding sandstone. If this were the case though, the pressure in the jet and sandstone at the interface would be expected to agree, which was found not to be the case. In further testing of this hypothesis, the jet material's strength was reduced by one – and then two – orders of magnitude. No significant decrease was observed in the residual pressure fields of simulations with preconfinement. Unexpectedly, a significant increase in the penetration depth of simulations without confinement did result. This observation, amongst others, led to the realization that the penetrator's properties have a more significant impact on the results than previously realized. Residual stresses have not been reported in the literature for the penetration of semibrittle geomaterials, and regardless of this fact, such residual stresses would be expected to have a gradient, for which normal component of stress reduces to zero at the free surface, or to that of the jet material at their interface.

It was also conjectured that the residual pressure might be a result of the way that the pressure boundary condition – used to simulate overburden – is enforced. This pressure boundary condition is enforced by applying point loads of appropriate magnitudes and directions to the particles at the boundary. These point loads were maintained throughout the duration of a simulation; this remained true even for the particles that were drawn into the penetration channel and hence no longer at the outer boundary. Accordingly, it was thought that the observed residual stresses might be attributable to boundary particles moving into the penetration channel in such a way to load the the inner surface of the penetration cavity. Subsequent simulations discredited this idea, first by turning off the pressure boundary condition at the time of jet impact, and second by placing a hole in the pressure boundary condition through which the jet was able to pass. In both cases no significant decrease in residual stresses was observed.

The nature of the residual stress profile has changed recently (Fig. 6.14b), as a result of extensive code modifications. These modification changed both the plastic-return algorithm and the curved-cap portion of the yield surface. Additionally, these simulations employed different treatments for the penetrator and the casing. While these changes affected the residual stress field, they did not eliminate it, thus leaving the causes of these stresses unclear. In short, these investigations have demonstrated that this phenomenon needs explanation.

6.3 Kinematic Anomalies

In visual postprocessing of early work, the presence of a kinematic anomaly was observed. Further review of other simulation results revealed similar anomalies. The aforementioned anomaly presents in the form of a small 'explosion' (Fig. 6.15) characterized by a sudden energy jump (Fig. 6.16). These events occur seemingly at random other than they tend to originate from highly deformed regions. Neither the cause nor resolution of these anomalies have yet to present themselves. Despite failing to resolve this problem, a number of code improvements were implemented, and potential causes ruled out.

Initially these events were thought to be the result of questionable nonphysical limits imposed on particle velocity, which were used temporarily during code development. These were removed in subsequent versions, yet the problem persisted. The anomaly then was thought to be the result of particle deletion algorithms, which are used to remove a problematic (primarily inverted domain) particle during a simulation. This also proved not the be the cause of the anomaly; after altering the deletion criteria – and even disabling deletion all together – failed to prevent these event.

The continued investigation of this problem has revealed issues associated with the use of a certain erosion algorithm. An investigation into the physics behind this algorithm revealed it to be apparently an incomplete and inadequately tested option, so it was removed from the code. This same work also led to the conclusion that massively deformed

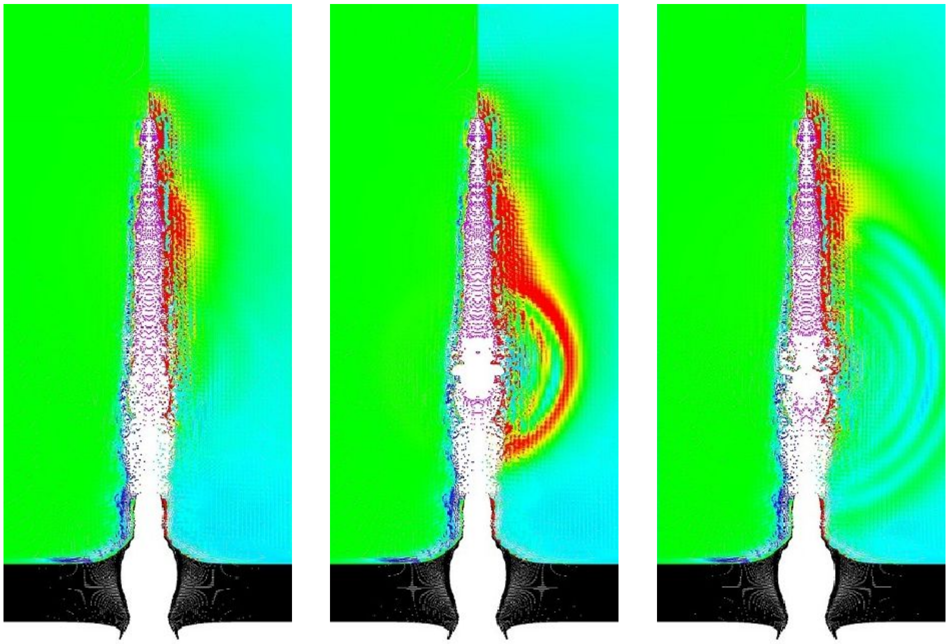

(a) 222 µs (b) 227 µs (c) 232 µs

Figure 6.15: Kinematic anomaly over 10 µs. Each image is a plot of volumetric plastic strain on the left and pressure on the right. Legend in Fig. 5.16. This event occurred during elastic relaxation long after the primary penetration event had completed (maximum penetration was achieved by 80 µs).

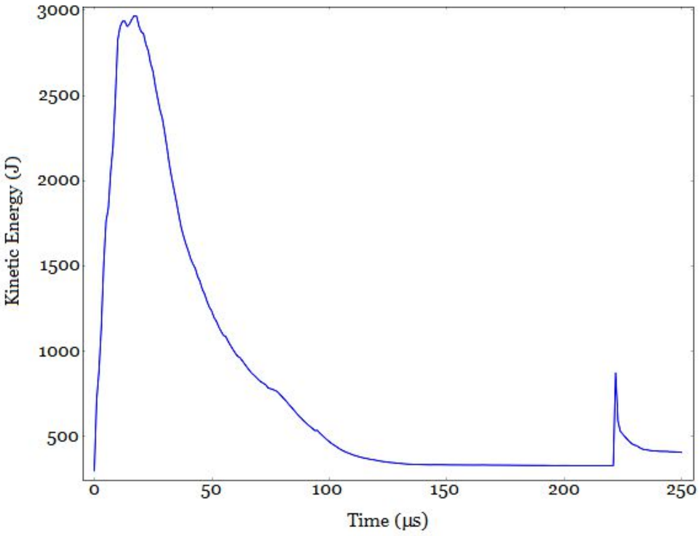

Figure 6.16: Total kinetic energy of jet material, demonstrating energy spike associated with a kinematic anomaly event.

particles (highly stretched and sheared – beyond what would be physically realistic of any geomaterial), appear to coincide with the occurrence of this issue. Further, it was found that currently used algorithms for updating position, velocity, and acceleration can result in an effective decoupling of these quantities, resulting in particle motion and velocity becoming tangential or even opposed to one another. The exact cause of this problem is not currently well understood and has led to the discovery of issues associated with the enforcement of boundary conditions that are used with the general interpolative method. None of the above observations have led to resolution the kinematic anomaly problem.

Error attributed to computation of the velocity gradient as reported by Wallstedt and Guilkey [20] was also investigated as a potential cause of kinematic anomalies. Movement of all kinematics from each constitutive model to a centralized algorithm within the Uintah framework, and the subsequent revision of the velocity gradient algorithm, resulted in a reduction in error for simple manufactured solution problems (such as for the generalized vortex [27] and axis-aligned displacement [22] problems Fig. 6.17). Despite this improvement, these changes ultimately led to earlier and more frequently occurring kinematic anomalies. The reason for this behavior is not well understood.

Throughout the course of this investigation kinematic anomalies were also observed in penetration simulations not using the Arenisca material model (such as the steel penetration problem discussed later – legend in Fig. 6.18 and kinematic anomaly in Fig. 6.19), as well as in the simulation of other phenomena all together (such as the water dam problem of [75] Fig. 6.20). This observation indicates that the kinematic anomaly problem is not associated with any particular constitutive model, which prompted the previously mentioned investigation

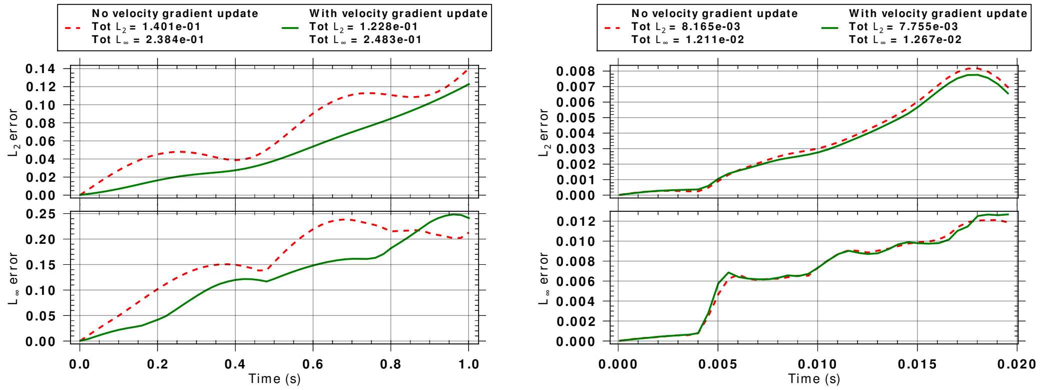

(a) Generalized vortex [27]

(b) Axis-aligned displacement [22]

Figure 6.17: Comparison of manufactured solution problems with and without enhancements to computation of the velocity gradient as proposed in [20].

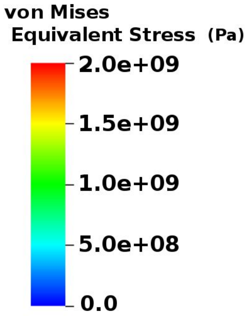

Figure 6.18: Von Mises equivalent stress legend for tungsten penetration of steel simulations

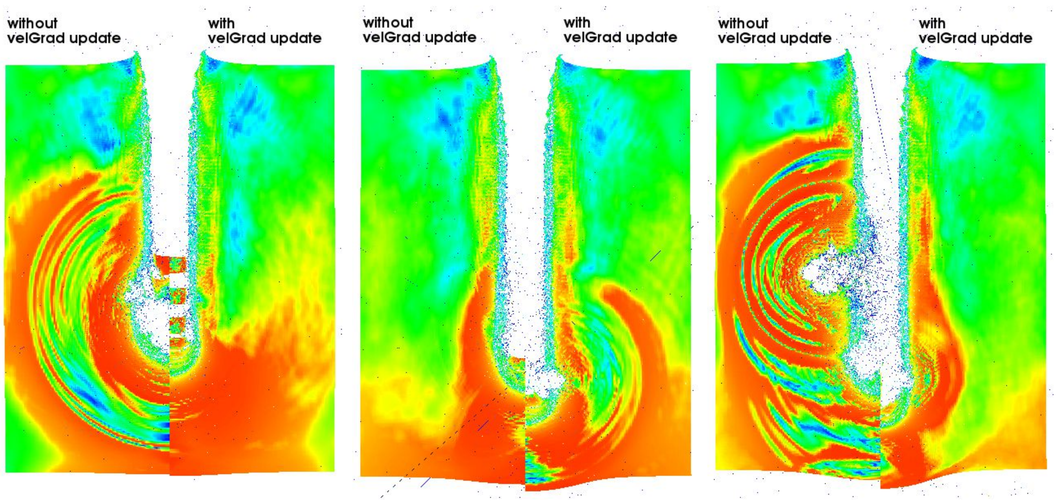

(a) Minimum 1 subcycles (b) Minimum 4 subcycles (c) Minimum 6 subcycles

Figure 6.19: Kinematic anomaly without using Arenisca in simulating perforation of a thick steel plate by a segmented rod tungsten penetrator. In each, equivalent stress is plotted (legend in Fig. 6.18). The right side of each corresponds to use of velocity gradient code enhancements, while the left was does not use these modifications. In both cases, only Uintah's *ElasticPlastic* material model was used without material strength erosion (*i.e.,* using option *none*). In each a different minimum number of subcycles is used to compute the deformation gradient tensor $\underset{\approx}{\mathbf{F}}$. The expected behavior would be more realistic deformations for an increasnig number of subcycles, up until the solution converges after a sufficiently high number is used. This is not what is observed in these results.

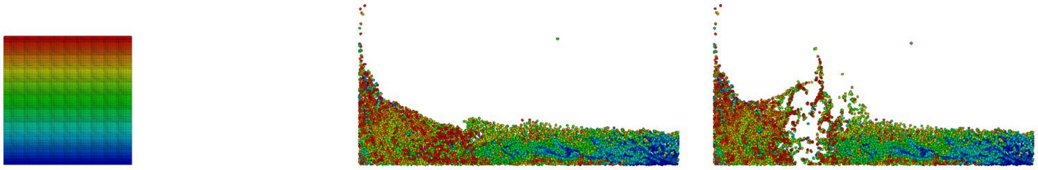
(a) Initial configuration (b) 12000 steps (c) 12500 steps

Figure 6.20: Kinematic anomaly breaking dam problem of [75]. Particles are color by particle number, which is meant to demonstrate the large mixing that occurs. The dynamic event is largely over by (b). A large kinematic anomaly is first observed in (c), this event was proceeded by many small 'pops'.

of velocity gradient enhancement, as well as the effect of subcycling. As seen in Fig. 6.19, however, there is no consistent correlation of these options with reduction in the likelihood of an anomaly. Therefore, because this unexplained and nonnegligible problem is so prevalent across many models, it is reccommended that further work should focus on the enforcement of fundemental governing equations within the host code.

Despite an earlier warning regarding the use of strain regularization, simulations meant to determine the effect of this feature in penetration simulations suffering from kinematic anomalies were carried out. The steel-billet penetration problem – discussed later in detail – was selected as it has a relatively low computational overhead. As a result of using strain regularization, small time-step issues prevented these simulations from reaching a point where kinematic anomalies were previously observed. The combined effects of strain regularization and the velocity gradient update were also evaluated, and the small timestep problem remained an issue. The results of these simulations are presented in Fig. 6.21. Initially up to 37 µs the results of both simulations are very similar to one another, and the previously executed steel penetration simulations. At approximately 50 µs into the simulation with only strain regularization enabled, the penetrator, as a result of interacting with the penetration debris, begins to come apart. This simulation ran 2 µs further, before small timesteps prevented further progress and the simulation was manually terminated.

In the simulation with both strain regularization and velocity gradient enhancements behavior more similar to previous simulations without these features was displayed, until being manually terminated at 79 µs. This was done as a result of the aforementioned small timestep problem.

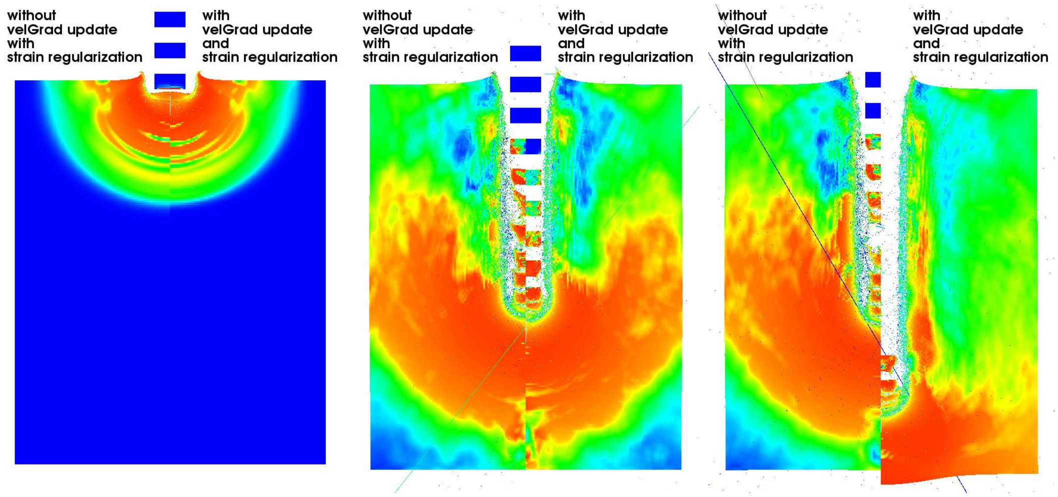

(a) 3 μs (b) 55 μs (c) 57 and 79 μs, respectively

Figure 6.21: Simulating perforation of a thick steel plate by a segmented rod tungsten penetrator to evaluate the effects of basic strain regularization. In each image, equivalent stress is plotted (legend in Fig. 6.18). The right side of each corresponds to use of only strain regularization, while the left deomonstrates the combined effects of strain regularization and enhancments to computation of the velocity gradient. In both cases, only Uintah's *ElasticPlastic* material model was used without material strength erosion (*i.e.,* using option *none*). In each case the simulation had to be manually terminated as a result of small timestep issues and is shown in the last frame at its final state.

6.4 Erosion Algorithm

In investigating the cause of both the previously discussed kinematic anomaly phenomena, and the problem of residual stresses, it was found that the erosion algorithm used at the time (*RemoveMass*) had been at one point partially removed from the elastic plastic material model. Further inspection led to the conclusion that this was causing spurious results in the materials using the *ElasticPlastic* material model. As a result, this option was subsequently removed in its entirety. After which, the effects of each erosion algorithm were compared in penetration simulations. The primary oberservation of which being that simulation results are highly dependent on erosion algorithm selection. This influence is especially apparent when using a segmented jet penetrator. Long-rod penetration, while less sensitive to erosion algorithm selection, is also noticably influenced.

Erosion algorithms are used to describe the way a material loses strength after satisfying a predefined failure criterion. Once triggered, the selected algorithm plays a critical role in the simulated material response under continued loading. A number of failure modes are supported within Uintah, as follows:

- Accumulation of material damage (d) by the Johnson-Cook damage model [81]. The constant damage rate over a step is

  $$\dot{d} = \frac{\dot{\epsilon}^p}{\left[D_1 + D_2 \exp\left(\frac{D_3 Tr(\underset{\approx}{\sigma})}{3\sigma_{\text{eq}}}\right)\right]\left[1 + D_4 \ln(\frac{\dot{\epsilon}^p}{\dot{\epsilon}^p_0})\right]\left[1 + D_5\left(\frac{T-T_0}{T_m-T_0}\right)\right]} \tag{6.5}$$

  where the numerator is the equivalent plastic strain at fracture (ϵ^p_f), $\dot{\epsilon}^p = (\frac{2}{3}\underset{\approx}{\dot{\epsilon}} : \underset{\approx}{\dot{\epsilon}})^{\frac{1}{2}}$ is the equivalent plastic strain rate, $\underset{\approx}{\sigma}$ is the Cauchy stress, $\dot{\epsilon}^p_0$ is a user-defined characteristic strain rate , T is the material temperature, T_m is the melt temperature, T_0 is the reference temperature, and D_1, D_2, D_3,D_4, and D_5 are material constants. A particle has fully damaged, and fails suddenly, after accumulating a damage value of one or greater.

- Softening as a result of material melting.

  $$T \geq T_m \tag{6.6}$$

  As a metal deforms plastically, heat is generated. In shock loading of metals, adiabatic heating is frequently assumed to occur, as there is not sufficient time for the conduction of this heat away from the highly localized shock front [82, 83, 84]. Accordingly, a portion of the plastic work is converted to heat. This heat is then used to increment material temperature (ΔT) at each step by

  $$\Delta T = \frac{\chi \sigma_y}{\rho C_p} \Delta \epsilon^p \tag{6.7}$$

  where, χ is the Taylor-Quinney coefficient, C_p is the material's specific heat, and σ_y is the current material yield/flow stress.

- Material fracture by the TEPLA-F fracture condition [85], which is satisfied when

  $$\left(\frac{f}{f_c}\right)^2 + \left(\frac{\epsilon_p}{\epsilon_p^f}\right)^2 = 1 \tag{6.8}$$

  where f is the current porosity, and f_c is the maximum allowable porosity. Once the above equation is satisfied, fracture within the material is said to have occurred.

- Material instability, which leads to bifurcation by the Drucker stability postulate [86],

  $$\underset{\approx}{\dot{\sigma}} : \underset{\approx}{\mathbf{D}}^p > 0 \tag{6.9}$$

where $\underset{\approx}{\dot{\sigma}}$ is the time rate of Cauchy stress and $\underset{\approx}{\mathbf{D}}^p$ is the rate of plastic deformation. Once the above inequality is violated, material bifurcation occurs.

- Exceeding the material's maximum critical stress.

$$\sigma_{\text{max}} > \sigma_{\text{eqv}} \tag{6.10}$$

where σ_{max} is the maximum critical stress, and $\sigma_{\text{eqv}} = (\frac{3}{2}\underset{\approx}{\sigma} : \underset{\approx}{\sigma})^{\frac{1}{2}}$ is the equivalent stress.

Once any of the above criteria have been satisfied, the erorsion algorithm modifies the material's ability to carry a load through modification of the material stress and, in the case of the *ZeroStress* criterion, the deformation gradient to the new values of $\underset{\approx}{\sigma}^*$ and $\underset{\approx}{\mathbf{F}}^*$, respectively. The following erosion algorithms are largely unvalidated and meant only to approximately mimic physically observed behavior of different materials [87]. The available erosion algorithms are:

- *none*: eroded particle strength remains unchanged. For this option, the damage state is still evolved, but the aforementioned revisions of stress is not applied, which is equivalent to turning off material strength erosion, and is the default.
- *RemoveMass*: eroded particle mass is reduced. The intended result is a reduced weighting of damaged particles in equations involving mass integrals. The algorithmic implementation of this method was not entirely clear even to some of the original developers [87]. As a result of this work, this erosion algorithm (which was erroneously left partially available) has been removed.
- *AllowNoTension*: particle supports no stress if there is a tensile hydrostatic component. Otherwise particle stress becomes hydrostatic.

$$\underset{\approx}{\sigma}* = \begin{cases} \frac{I_1}{3}\underset{\approx}{\mathbf{I}} & , I_1 \leq 0 \\ \underset{\approx}{\mathbf{0}} & , I_1 > 0 \end{cases} \tag{6.11}$$

- *AllowNoShear*: eroded particle supports only hydrostatic stresses.

$$\underset{\approx}{\sigma}* = \frac{I_1}{3}\underset{\approx}{\mathbf{I}} \tag{6.12}$$

- *ZeroStress*: eroded particle cannot support stress, and its deformation is frozen.

$$\underset{\approx}{\sigma}* = \underset{\approx}{\mathbf{0}} \tag{6.13}$$

$$\underset{\approx}{\mathbf{F}}^{*} = \underset{\approx}{\mathbf{F}}^{n} \tag{6.14}$$

where $\underset{\approx}{\mathbf{F}}^{n}$ is the deformation gradient at the beginning of the step.

Figures 6.22 through 6.26 show snapshots at different points in time of simulations using the discrete jet description for each of the above erosion algorithms. The left side of each frame is a plot of plastic volumetric strain, while the right side is of pressure (legend – Fig. 5.16). Figure 6.27 is a plot of penetration depth through time for the same same simulations. The first 30 μs of each simulation are very similar, exhibiting only minor differences in deformation of the steel liner. After which, the results cluster into two groups: the first being composed of *AllowNoTension* and *ZeroStress*, and the second being composed of *none*, *AllowNoShear*, and *RemoveMass*.

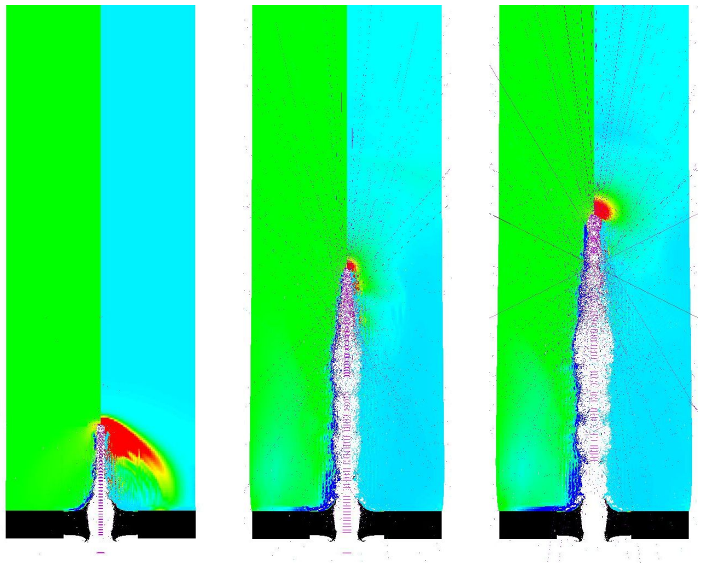

(a) 18 μs (b) 75 μs (c) 107 μs

Figure 6.22: Simulated liner perforation and penetration into sandstone using the erosion option *none*. The left and right are plots of volumetric plastic strain and pressure, respectively (legend in Fig. 5.16). (c) is the final state at 107 μs where the simulation was terminated by the host code as a result of a negative Jacobian error.

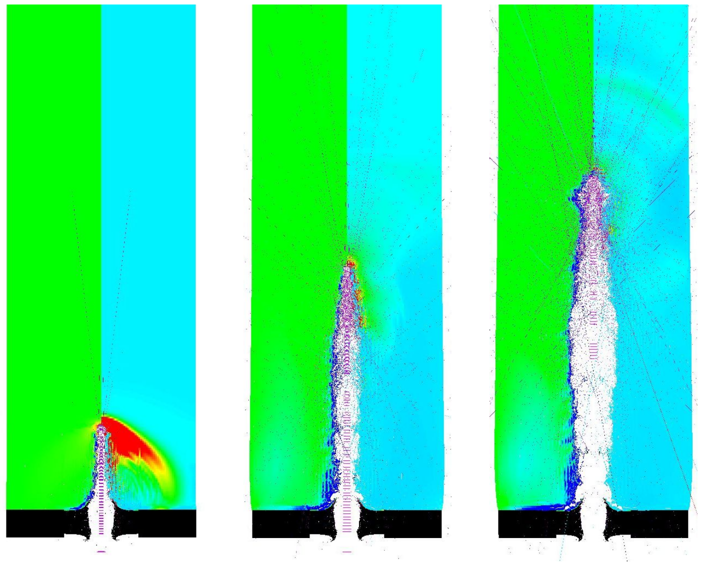

(a) 18 μs (b) 75 μs (c) 150 μs

Figure 6.23: Simulated well-liner perforation and penetration into sandstone using the erosion option *RemoveMass*. The left and right are plots of volumetric plastic strain and pressure, respectively (legend in Fig. 5.16). This simulation ran successfully to a final time of 350 μs, and penetration depth of 0.22 m.

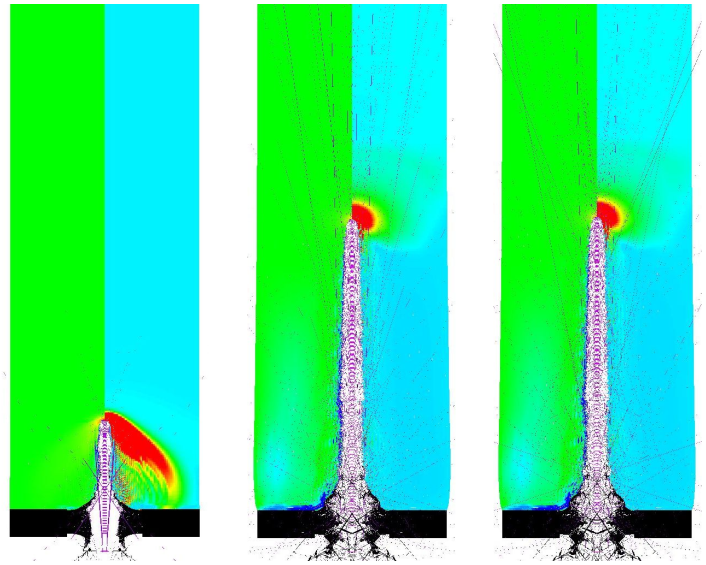

(a) 18 μs (b) 75 μs (c) 76 μs

Figure 6.24: Simulated well-liner perforation and penetration into sandstone using the erosion option *AllowNoTension*. The left and right are plots of volumetric plastic strain and pressure, respectively (legend in Fig. 5.16). (c) is the final state at 76 μs where the simulation was terminated manually as a result of having an intractably small timestep.

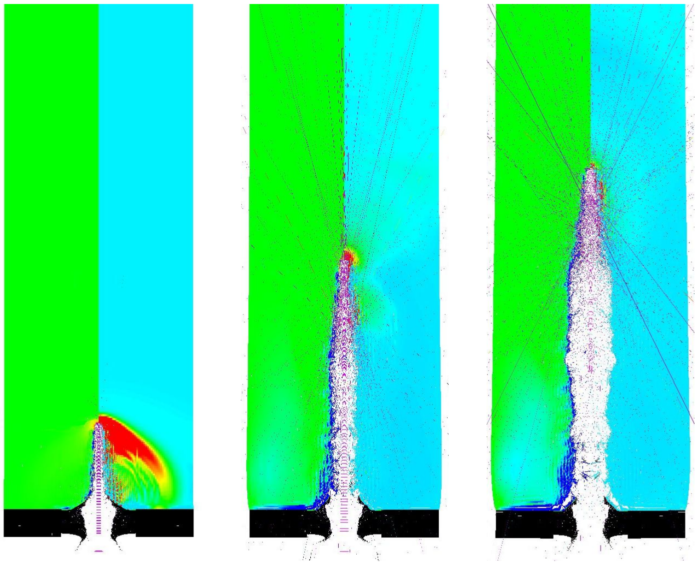

(a) 18 µs (b) 75 µs (c) 150 µs

Figure 6.25: Simulated well-liner perforation and penetration into sandstone using the erosion option *RemoveMass*. The left and right are plots of volumetric plastic strain and pressure, respectively (legend in Fig. 5.16). This simulation would later encounter multiple kinematic anomalies, and terminate as a result of a negative Jacobian error at 260 µs.

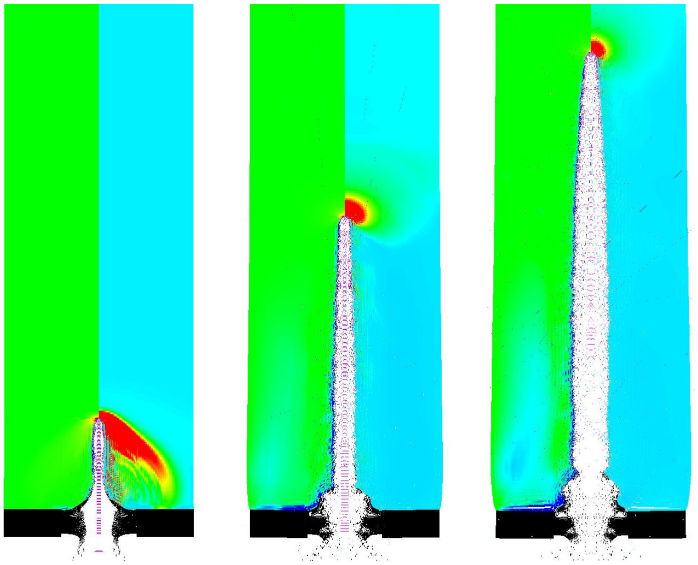

(a) 18 µs (b) 75 µs (c) 150 µs

Figure 6.26: Simulated well-liner perforation and penetration into sandstone using the erosion option *ZeroStress*. The left and right are plots of volumetric plastic strain and pressure, respectively (legend in Fig. 5.16). This simulation ran successfully to a final time of 350 µs, and penetration depth of 0.35 m, though the rate of penetration had not yet reached zero.

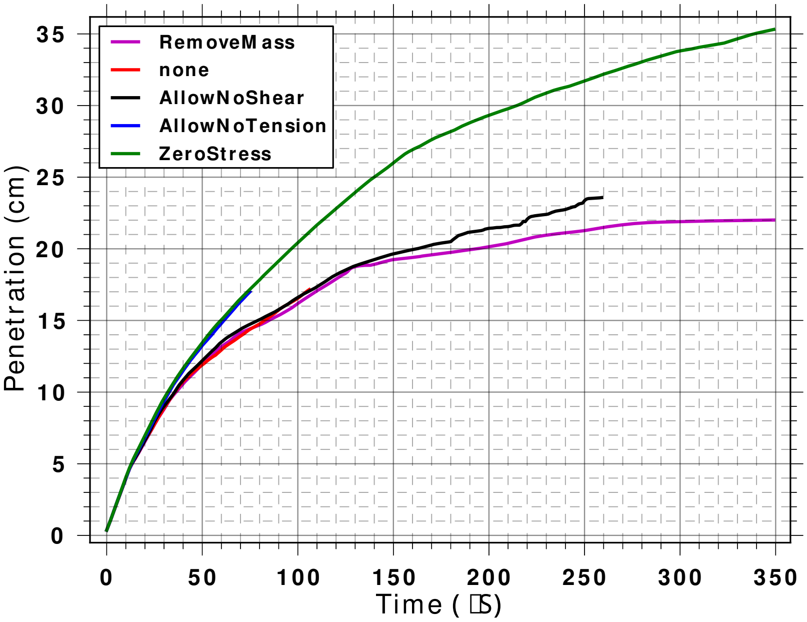

Figure 6.27: Comparison of penetration though time for different erosion algorithms solving perforation of a well liner followed by penetration into sandstone.

In the first group, the penetration channel walls are smoother, and the region of highly distended sandstone particles (blue particles on the left half of each) is considerably smaller; also the steel liner (black at the bottom on both sides of each frame) tends to come apart, which results in a larger diameter entry into into the sandstone. In contrast, the second group has a smaller diameter entry through the steel, which then opens to a wider diameter channel having greater, and more abrupt, variations in diameter in the sandstone. The second group also appears to focus the jet more abruptly into a point at the tip of the penetration channel, this is particularly noticeable in both the results for *AllowNoShear* and *none*. *AllowNoShear* and *RemoveMass* both exhibited kinematic anomalies, with *AllowNoShear* having repeated events prior to failing at 260 μs because of a negative Jacobian. The simulation for *none* also terminated abruptly at 107 μs for the same reason but did not suffer from the occurrence of kinematic events. *AllowNoTension* failed even earlier at 76 μs, and also did not exhibit kinematic anomalies. Of the five simulations, only *RemoveMass* and *ZeroStress* ran to completion at 350 μs. These also, in terms of both penetration history, and the nature of the resultant channel, are the the most different. Further, *RemoveMass* exhibited a large single kinematic anomaly at 129 μs, accounting for the unusual shape of the penetration channel at its tip.

Other simulations were run comparing the two most promising, and different, erosion algorithms, *none* and, *ZeroStress*. Both long-rod and segmented penetrators were used to penetrate a 0.0495 m thick, 0.040 m diameter, 4130 armor-steel billet using the material properties of [88]. In each instance, the penetrator had a constant velocity of 1700 m/s, mass of 0.0111 kg, length of 0.05 m, and diameter of 0.0040 m. For the case of a segmented penetrator, the long-rod penetrator was cut into sections each having a length of one half the rods diameter, each of which was then separated by a void of the same length. The segments of the segmented rod are expected to exhibit an increase in penetration efficiency (penetration of an individual segment divided by its length) as a result of their length (L_{seg}) to diameter ratio ($L_{\mathrm{seg}}/D = 1/2$) [89, 90]. Further, because of this effect, the total penetration of the segmented-rod penetrator should be greater than its solid rod counterpart [91, 48, 92, 49, 93]. Figures 6.28 and 6.29 are plots of von Mises equivalent stress (σ_{eqv}) for long-rod and discrete penetrators, respectively. The left half of each corresponds to using option *none*, while the right corresponds to using *ZeroStress*.

In comparing the results for both long-rod and segmented penetrators (Table 6.5), the penetration depth and cavity radius increased when using the *ZeroStress* option. As reported in the literature for segmented penetrators of the same aspect ratio as the segmented penentrator being used herein, the desired trend of increased penetration is produced by

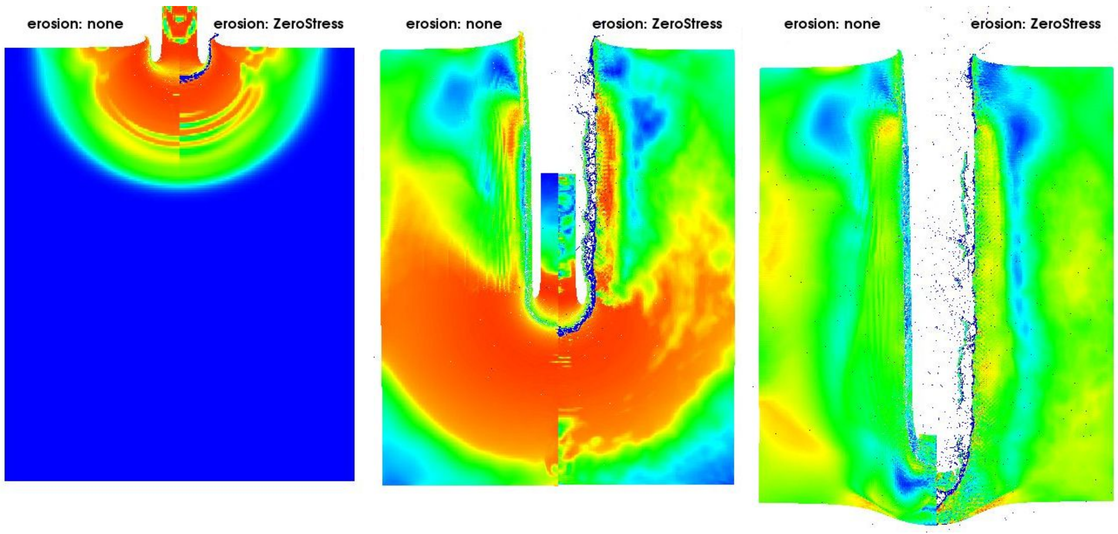

(a) 3 μs (b) 39 μs (c) 100 μs

Figure 6.28: Comparison of von Mises equivalent stress, using the erosion algorithms *none* (left) and *ZeroStress* (right), for tungsten long-rod penetration of a steel billet (legend in Fig. 6.18).

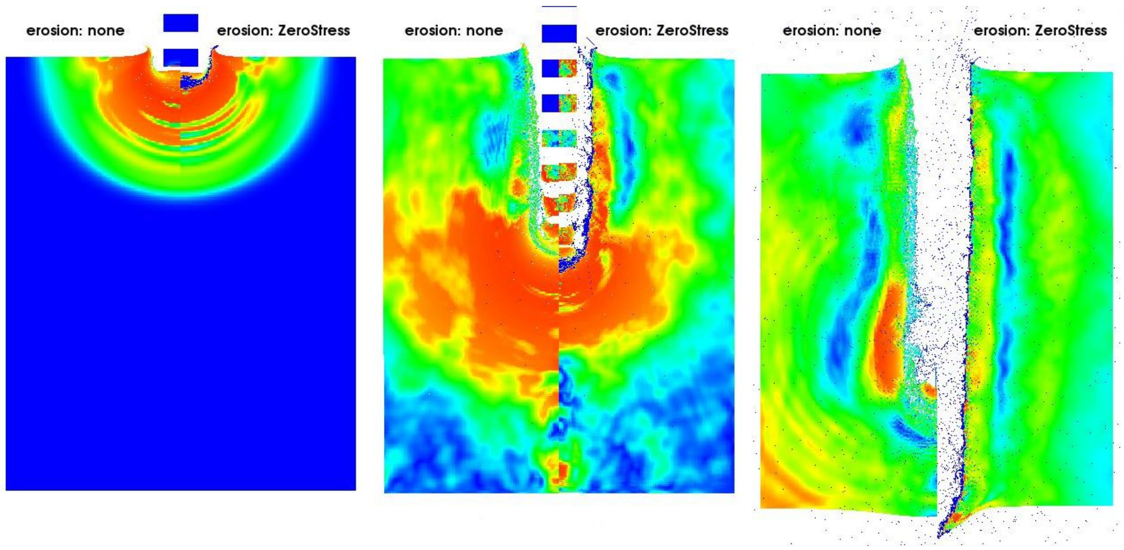

(a) 3 µs (b) 39 µs (c) 100 µs

Figure 6.29: Comparison of von Mises equivalent stress, using the erosion algorithms *none* (left) and *ZeroStress* (right), for tungsten segmented-rod penetration of a steel billet (legend in Fig. 6.18).

Table 6.5: Comparing erosion algorithm effects on depth of penetration, for tungsten into a steel billet.

Simulation	**Penetration** (mm)	**Average channel radius** (mm)
Solid Rod - *none*	47.59	3.65
Solid Rod - *ZeroStress*	52.27	4.21
Segmented Rod - *none*	41.12	3.13
Segmented Rod - *ZeroStress*	54.75	3.50

the *ZeroStress* option.

Viewed from the perspective of Pack and Evans [39], to account for both strength effects and secondary penetration Eqn. 3.5 can solved for the unknown coefficient α

$$\alpha = \frac{\rho_p V^2}{\sigma_y}\left[1 - \sqrt{\frac{\rho_t}{\rho_p}}\left(\frac{P-r}{L}\right)\right] \tag{6.15}$$

The rod and target's material paramters ($\sigma_y = 1.5$ GPa and $\lambda = 1$) are then plugged into the above equation, the value returned is then subsequently used to obtain the reported values of $\alpha\sigma_y/\rho_p V^2$ in Table 6.6. Equation. 3.5 then must be further manipulated in order to solve for the segmentation parameter of the segmented penetrator as

Table 6.6: Comparing erosion algorithm effects on the dimensionless penalty parameter, for tungsten into a steel billet.

Erosion algorithm	**Dimensionless penalty parameter ($\alpha\sigma_y/\rho_p V^2$)**
none	0.413
ZeroStress	0.358

$$\lambda = \frac{\rho_t}{\rho_p}\left[\frac{P-r}{L\left(1-\frac{\alpha\sigma_y}{\rho_p V^2}\right)}\right]^2 \tag{6.16}$$

Using the the previously determined dimensionless penalty parameter (which should be constant for a particular material pairing) and the above equation the segmentation paramters reported in Table 6.7 were obtained. It is reported that better agreement with this theory is produced for both penetrators when using the *ZeroStress* option. This is true both for the nondimensional quantity $\alpha\sigma_y/\rho_p V^2$ and the segmentation parameter λ.

On the other hand, use of *none* for the long-rod penetrator appears to aggree better with the work of Anderson *et al.* [88], in terms of penetration depth, cavity radius, and the resulting bulge at the bottom of the penetrator as observed in Fig. 6.28c. For reference, the predicted hydrodynamic penetration would be in each case 0.0749 m, which represents a full perforation of the billet, something that was only just barely achieved for the segemented penetrator (Fig. 6.29c).

Other differences are observed in the nature of the resulting debris, as demonstrated for long rods in Fig. 6.28c. Using *none* the penetrator inverts to smoothly coat the penetration channel, something frequently observed in hypervelocity penetration by high-density ductile metals penetrating low density targets of sufficient depth [94]. Using *ZeroStress*, the penetrator's remains broke into three largely coherent clusters (seen clearly separated from

Table 6.7: comparing erosion algorithm effects on the dimensionless segmentation parameter, for tungsten into a steel billet.

Erosion algorithm	**Dimensionless segmentation parameter (λ)**
none	0.747
ZeroStress	1.137

the target material in Fig. 6.28c), which do not cling to the channel walls. This difference is thought to result from the combined effects of zeroing the stress, and freezing the deformation gradient of damaged particles by the *ZeroStress* option. In comparing the results for a segmented penetrator, these differences become more apparent. For *ZeroStress*, the debris is more dispersed, and observed interacting to a greater degree with the incoming segments of the penetrator. The influence of crater ejecta on the penetration of individual segments, and ultimately final depth of penetration, plays a critical role, though how, and to what degree, is currently not well understood [95]. For both long-rod and segmented penetrators using *ZeroStress*, the resultant target stress field is generally lower in magnitude in comparison to *none*, as seen in the figures by the smaller size of the red areas. When using a segmented penetrator with the erosion algorithm option *none*, a kinematic anomaly occured. This was the first instance of such an anomaly observed in Uintah simulations not using the Arenisca model, which led to the use of this simulation in exploring that problem as previously discussed above.

Now simulations are presented comparing the effects of erosion algorithm selection in long-rod and discretized jet penetration. In each, Arenisca was used to simulate a sandstone target ($\rho_t = 2300 kg/m^3$) without the steel liner. Further, the discrete jet description representing a shaped-charge jet was used in a role similar to the previous segmented-rod penetrator (refer to Figures 5.3 and 5.4). In order for the results to be directly comparable, the segments of the discrete jet were prescribed a constant velocity (see Fig. 6.30). The velocity of both the discrete jet and rod penetrators was set to 3266 m/s, as this velocity is roughly the mass-weighted average of the variable-velocity shaped-charge jet description. In both instances, the penetrators have a total mass of 0.0101 kg, total momentum of 33 N·S, and total kinetic energy of 54 kJ. Further, both the collapsed length of the discrete-jet penetrator (sum of the lengths of the individual segments), and length of the rod, are the same at 0.0795 m. The diameter of the rod was selected to be 2.9 mm in order to enforce the preceding relationships; this value is nearly the average diameter of the discrete jet which is 3.1 mm.

The results for this sandstone problem specification are somewhat different from those previously discussed for the penetration of a steel billet. Referring to Fig. 6.31, the following observations may be made about the influence of the type of penetrator and choice of erosion algorithm:

- Not all simulations reached their final penetration depth (where the slope asymptotes to zero). The values cited in Table 6.8 are the peak values reached in each simulation. The rod simulation with option *none* was terminated normally by reaching

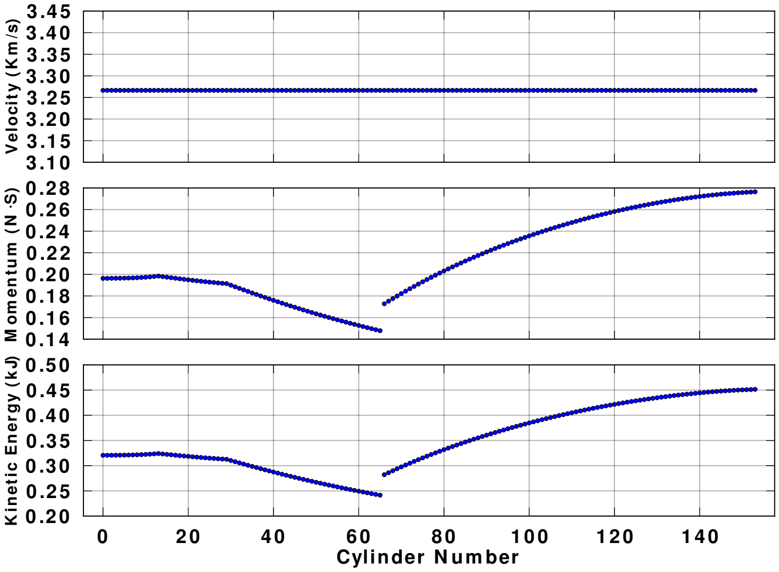

(a)

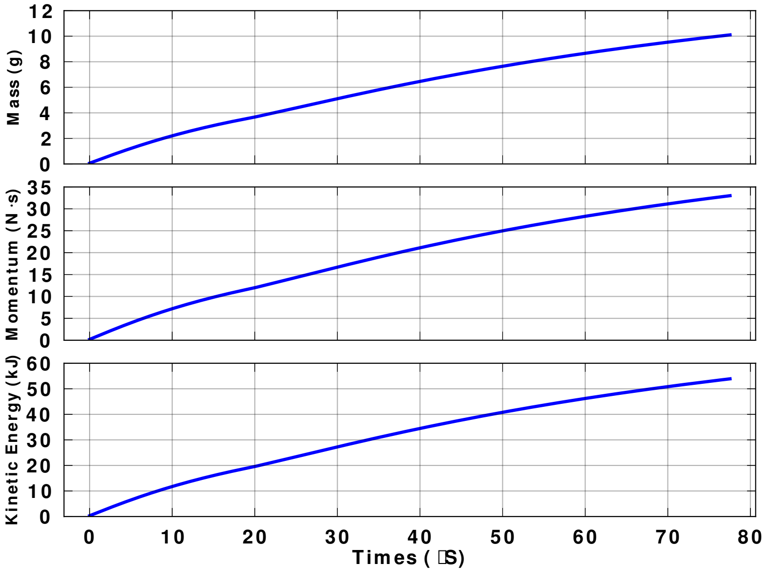

(b)

Figure 6.30: Constant velocity (3266 m/s) discrete jet penetrator description. (a) contains plots of individual cylinder properties, and (b) contains plots of the cumulative mass, momentum, and energy, entering the simulation domain over time. Figures 5.3 through 5.4 are the same plots for the discrete segmented penetrator, which was formulated to match a shaped-charge jet.

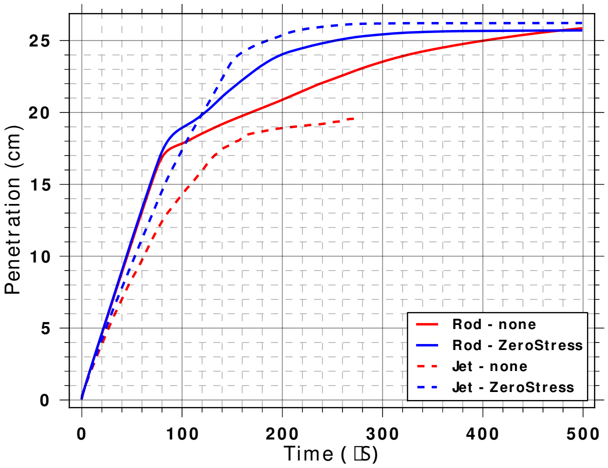

Figure 6.31: Comparing erosion algorithm effects on depth of penetration through time, for tungsten into sandstone.

Table 6.8: Comparing erosion algorithm effects on depth of penetration, for tungsten into sandstone.

Simulation	**Penetration (cm)**
Solid Rod - *none*	25.85
Solid Rod - *ZeroStress*	25.71
Discrete Jet - *none*	19.68
Discrete Jet - *ZeroStress*	26.22

its preselected end time, but it is clear from the positive slope at the stop time in the figure that the penetration depth for that simulation was still increasing and was thus expected to ultimately match or exceed the reported penetration depth for the other simulations. The jet with option *none* terminated prematurely because the particle deletion algorithm suddenly removed the majority of particles in the simulation. Because output is only generated at prdefined intervals the cause of this is not known but it is suspected to be a chain reaction of kinematic anomalies. For reference the hydrodynamic depth of penetration predicted for both penetrators is 0.23 m.

- For jet segments all having a length-to-diameter ratio significantly smaller than unity, it is expected that the final penetration depth would be deeper than its solid-rod counterpart, and this behavior is seen in comparing the zero-slope portions of the dashed and solid blue lines.

- The steady-state phase of the penetration process, defined by the nearly linear initial portion of each line, is similar for both rod simulations, neither exhibiting sensitivity to the erosion option. However, the erosion option does show strong influence on the steady-state phase of penetration for the jet.
- The secondary penetration phase, defined to occur after the initial nearly linear portion, is influenced by the erosion option to varying degrees in all simulations. The changes in slope during the secondary penetration might also be attributable to boundary effects. In particular, the simulated target appears to have had too small a diameter (0.0508 m) for use with a free surface condition and such highly energetic penetrators, especially when combined with the use of a solid-rod penetrator. This conclusion is based on the significant radial crater growth, and associated bulging observed in the figures to follow. The cause of the difference between the rod and jet penetrations is suspected to be a combination of this boundary effect, and too small a computational domain, which combinecd to allow mass to flux out of the computational domain. This in turn produced reducing resistance to deformation, allowing unchecked radial expansion, and increased axial penetration.

The development of the penetration channel for both the rod and segmented penetrators using each erosion option is illustrated by a sequence of plots. Each plot is of the Jacobian of the deformation gradient (indicating volumetric expansion/contraction) on the left, and von Mises equivalent stress on the right, with the legend for each found in Fig. 6.32. Rod simulation results are found in Figures 6.33 and 6.34, while the discrete jet results are found in Figures 6.35 and 6.36.

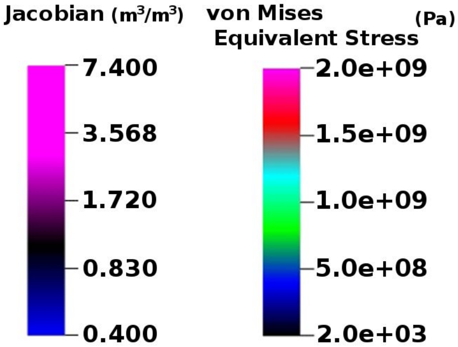

Figure 6.32: Combined legend for Jacobian and von Mises equivalent stress.

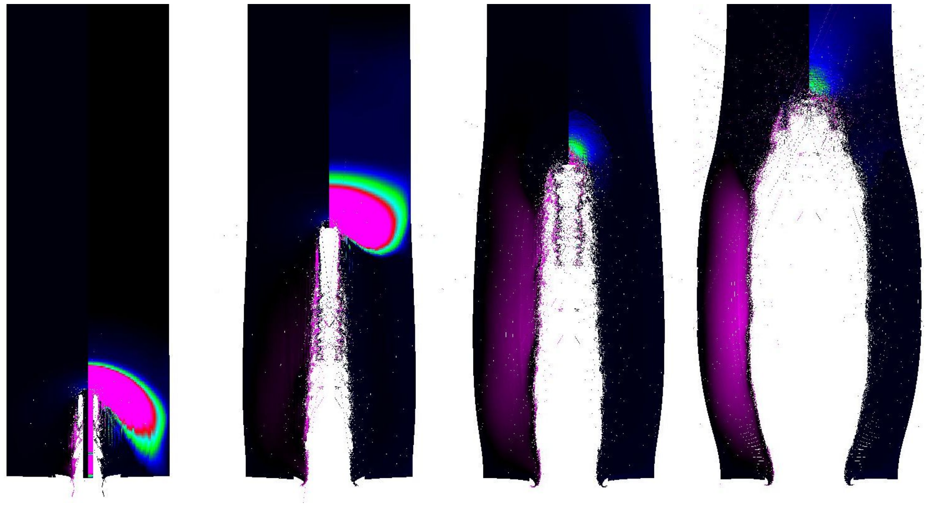

(a) 25 μs (b) 75 μs (c) 150 μs (d) 300 μs

Figure 6.33: Plots of Jacobian (left) and equivalent stress (right) for tungsten long-rod penetrator using erosion algorithm *none* to penetrate into sandstone without a steel liner (legend in Fig. 6.32). This simulation went on to successfully terminate at 500 μs.

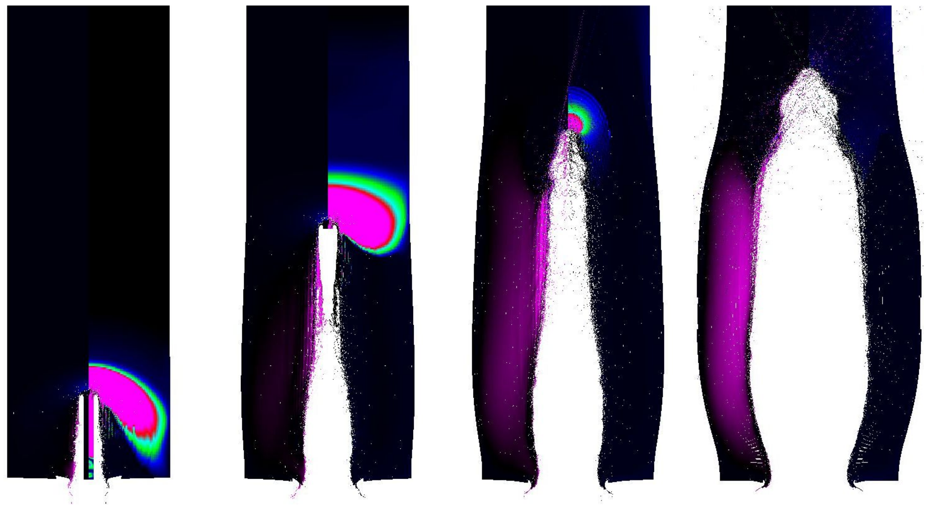

(a) 25 μs (b) 75 μs (c) 150 μs (d) 300 μs

Figure 6.34: Plots of Jacobian and equivalent stress for tungsten long-rod penetrator using erosion algorithm *ZeroStress* to penetrate into sandstone without a steel liner (legend in Fig. 6.32). This simulation went on to successfully terminate at 500 μs.

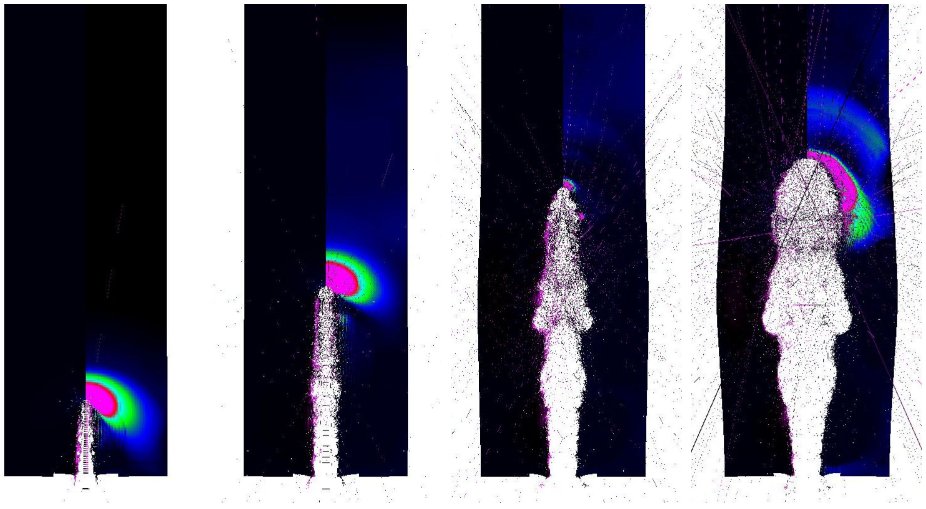
(a) 25 μs (b) 75 μs (c) 150 μs (d) 278 μs

Figure 6.35: Plots of Jacobian (left) and equivalent stress (right) for a tungsten discrete jet penetrator having a constant velocity and using erosion algorithm *none* to penetrate into sandstone without a steel liner (legend in Fig. 6.32). This simulation ran to the full time of 500 μs, but encountered numerous kinematic anomalies, and ultimately deleted the majority of its particles between 278 and 279 μs.

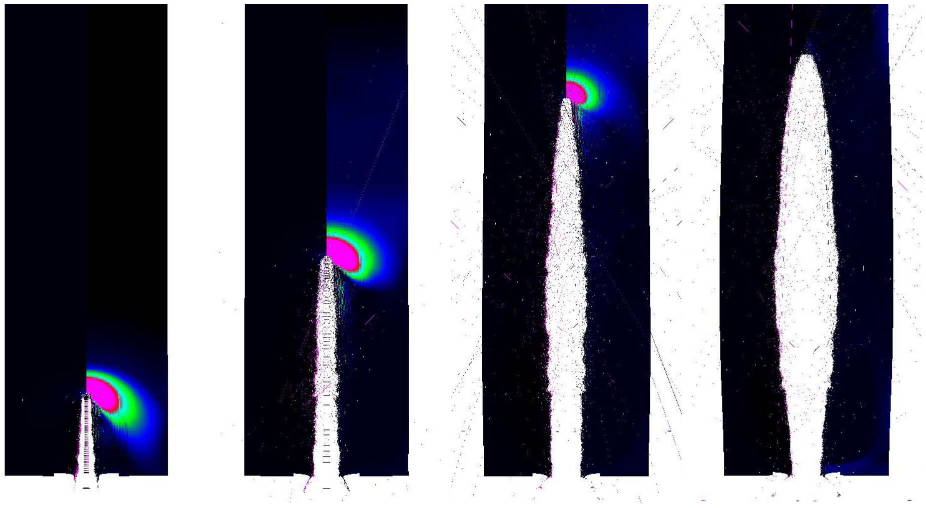
(a) 25 μs (b) 75 μs (c) 150 μs (d) 300 μs

Figure 6.36: Plots of Jacobian (left) and equivalent stress (right) for a tungsten discrete jet penetrator having a constant velocity and using erosion algorithm *ZeroStress* to penetrate into sandstone without a steel liner (legend in Fig. 6.32). This simulation went on to successfully terminate at 500 μs.

For both the rod penetrator simulations, primary penetration, defined by the penetration depth at which the intial rod is fully consumed, is nearly complete by 75 μs. This is evidenced both by the abrupt change in the slope of the penetration history of these simulation at this point (in Fig. 6.31), and also by observing the nearly complete consumption of each rod in Figures 6.33b and 6.34b. The penetration occuring in each of these simulations after this point is secondary penetration and a result of the large amount of energy still in the penetrators debris. In Figures 6.33b and 6.34b it is observed that this debris is heavily influenced by erosion algorithm selection. The debris field using *none* is longer, more broken up, and has both large and small particles as indicated on the left of the figure (Fig. 6.33b) by the debri being both pink and black. Conversely, using option *ZeroStress* (Fig. 6.34b) the debris is largely coherent, slightly shorter, and as indicated on the left of the plot is largely dilatated as indicated by the pink particles which denote volumetric expansion by a factor of approximately two or greater (Fig. 6.32).

The effects these differences have on secondary penetration are illustrated in Figures 6.33c and 6.34c, where for *none* (Fig. 6.33c) the magnitude of the equivalent stress (on the right side) at the forefront of the penetration channel is low in comparison to *ZeroStress* (Fig. 6.34c). This is despite the fact that *none* has significantly more penetration debris left still acting to penetrate, serving also to indicate that the residual velocity of the debris using *none* is likely considerably lower. Further, the debris of *none* at this point is radially some distance from the centerline, while that of *ZeroStress* is focused along the axial centerline; this is likely responsible for the rounded channels end obtained using *none* (Fig. 6.33d), compared to the more pointed tip of *ZeroStress* (Fig. 6.34d), as viewed 150 μs later.

It is difficult to make simillar observations for the discrete penetrator on account of the simulation using erosion option *none* exhibiting multiple kinematic events. These events caused the unusual penetration channel observed in Figures 6.35c and 6.35d. Alternatively, using option *ZeroStress* formed a bulbous but otherwise not unusual penetration channel (Fig. 6.36d). One significant difference in comparing the discrete penetration simulation direction to their long-rod counterparts is that the discrete penetrator simulations present very few highly dilatated particles as indicated by the absence of pink on the left side of the plots in Figures 6.35 and 6.36. The reason for this is not well understood, though it is suspected that it may be related to the aforementioned boundary problem in the rod simulations.

It is also possible that the erosion algorithm only being active in the penetrator, not both the penetrator and target, may have played a role in producing the different responses observed here in comparison to the above steel billet problem used to investigate erosion option effects. It is reccomended that simulations such as these be used to further investigate the effects of the discrete penetrator and erosion algorithm in the future, though a more structured approach should be used, starting with a segmented penetrator like that used above in the steel billet problem and progressing incrementally towards the discrete description of a shaped charge jet as described in Chapter 5.

CHAPTER 7

POSTPROCESSING SIMULATION RESULTS

In tandem to the execution of a large number of full-scale simulations, both data decimation and visualization methods were improved. This was necessitated by the large amounts of data produced by a single simulation, which can regularly range from 10-100 GB, and in some instances be over 500 GB. In order to make the best use of high-speed computing resources, this data needed to be quickly processed, archived, and then deleted. To this end, automated Python scripts were developed to satisfy the problem-specific needs of the research group. Further, both generalized and automated visualization tools were developed, again using Python, both to improve the content and fidelity of these visualizations.

7.1 Improved Visualization Techniques

The open source visualization tool VisIt [96] is used to perform postprocessing of simulation data. VisIt was selected because it is open source, designed to take advantage of multiple processors, and also compatible with massive data sets. Working with the university's scientific computing and imaging institute (SCI), as well as the developers of VisIt, previous work to represent the physical deformation in particle simulations was debugged and improved. Doing this required development of small tests, which were used by the developers in resolving issues, in order to replicate problematic phenomena.

A bug was resolved which caused plot colors to be drawn from garbage numbers, as well as a bug which caused particle glyphs to dissapear at random during rendering. Further, as a direct result of fixing these problems, and as well as interactions with both SCI, and VisIt's developers, deforming glyph features were incorporated into the standard VisIt release. According to Neeman [97], glyphs can be defined as 'a graphical icon that uses color and shape to illustrate features of the object it represents'. There exist a number of different glyphs which can be used to represent different dimensionalities of data. The most basic type of glyph uses scalar fields to represent both color and shape. These were initially used to visualize penetration simulations, but have fundemental shortcomings when used in this way. A variety of shapes are frequently used as glyphs, amongst them, the cube, sphere, and icosahedron are the most prevalent, each of which suffer from the same shortcoming when used with scalar measures of shape in large-deformation problems. In MPM simulations, a finite particle domain is assumed, which changes throughout a simulation as a result of deformation. The aforementioned glyphs suffer from failing to account for these changes in the domain's shape and size.

The sphere and icosahedron capture neither a particle's deformed domain nor the continuum nature of a material prior to deformation (*i.e.,* they do not fill space, and thus may have gaps and/or overlaps, either of which masks the data of visualizations). The cube, while able to represent the initial continuum (under circumstances where initial particle domains coincide with this description) suffers from the same masking problem during deformation. While the Jacobian of the deformation gradient and other measures of deformation can be used to scale these descriptions, they only serve to mitigate and not eliminate this problem. To overcome these deficiencies, a superior method proposed by Choudhury *et al.* is used [98], whereby particle domains are represented by parallelepipeds (providing support for nonuniform cuboids), which are then deformed by the tensor field of particle deformation gradients ($\underset{\approx}{\mathbf{F}}$). This method is able to provide 3-d insight throughout the deformation process into the deformation of materials at multiple scales. More importantly this method is able to faithfully represent extreme deformations, as in hypervelocity penetration processes. Further, as the deformation gradient itself is at the foundation of the algorithms used in any solid mechanics code, use of this deformed glyph method can be a valuable V&V tool in assesssing code qaulity.

Figures 7.1 and 7.2 represent the use of different glyhs in visualizing penetration simulation data. For both sphere and cube glyphs, significant overlapping occurs. This is markedly prevalent in the crushed zone at the free surface of the penetration channel. This area, and its surroundings, are particularly important in studying the effects of penetration on rock properties such as porosity and permeability. When using deformed parallelepiped glyphs, the continuum of the material being represented by discrete particles is better expressed. Further, the exact deformation of each particle is accurately represented. While overlapping also occurs when using this glyph, it is minimal and real, only serving to highlight the need for methods to deal with particle failure, as it is unlikely a material element would in reality be able to withstand such extreme stretches and shearing. These features are especially well demonstrated in Fig. 7.2c. During this simulation a number of kinematic events occured, which resulted in the unusual cavity, and the extreme deformation of particles. The 'x' that

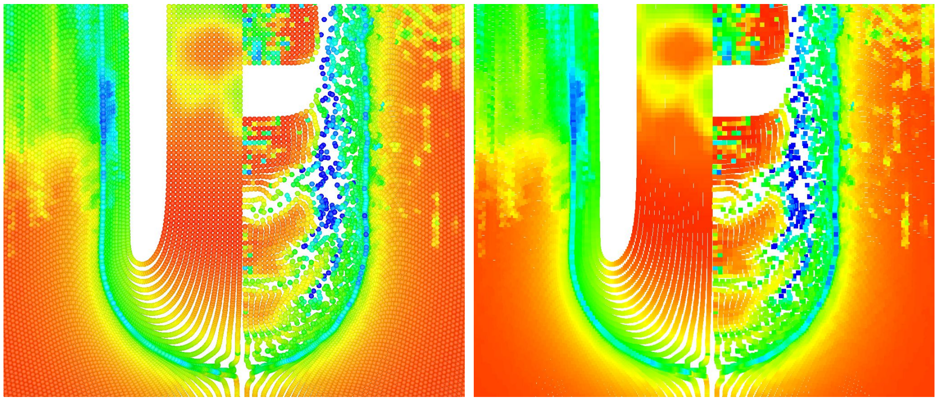

(a) sphere (b) cube

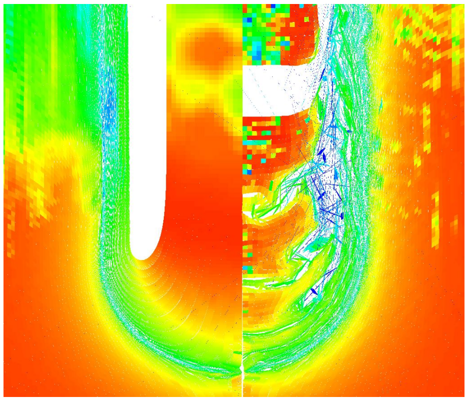

(c) deformed parallelepiped

Figure 7.1: Comparison of sphere, cube, and deformed parallelepiped glyphs to visualize particle data. Each plot is of equivalent stress (legend in Fig. 6.18), for two different tungsten penetrators (long-rod left and segmented-rod right) penetrating a cylinderdrical armor steel billet from above. (a) uses spherical glyphs to represent each particle and despite there being small gaps in the intial configuration significant overlapping occurs in the debris of the penetrator. (b) uses cube glyphs and faithfully represents the initial configuration, but suffers from more sever overlapping of the glyphs in the debris field. (c) uses deformed parallelepiped glyphs which are able to accurately portray both the intitial, and current configuration of particle domains, providing greater clarity with regard to the deformation of the penetrator, and to particle-particle interactions.

crosses the center of the figure is in fact a stretched and sheared particle, which has been reflected in the process of generating this image from axisymmetric simulation data. Such observations of extreme material deformation, inconsistent with the overall deformation of the particles as a group, has led new research to focus on better coupling the updates of particle deformations with particle positions uncovering opportunities for improvement through boundary enrichment.

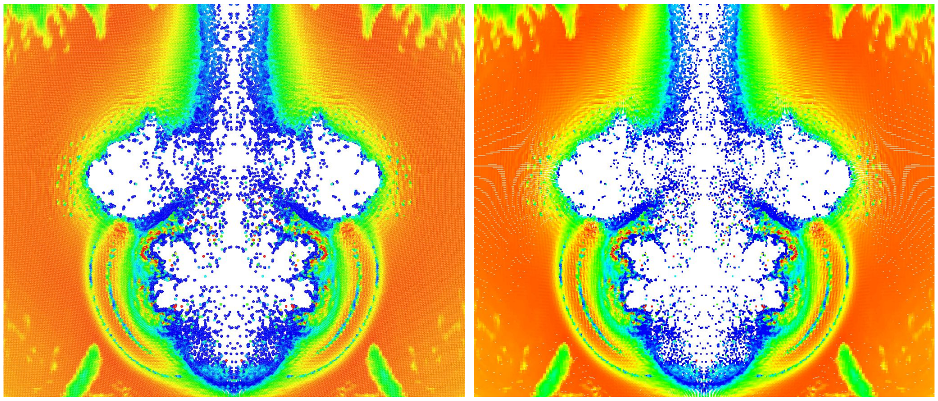

(a) sphere (b) cube

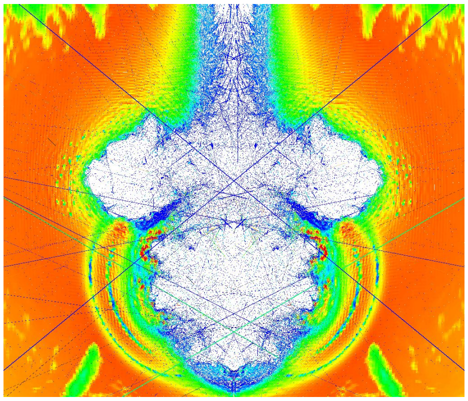

(c) deformed parallelepiped

Figure 7.2: Comparison of sphere, cube, and deformed parallelepiped glyphs to visualize particle data. Each plot is of equivalent stress (legend in Fig. 6.18), for penetration of a cylinderdrical armor steel billet from above by a tungsten long-rod penetrator. This simulation suffered from multiple erroneous kinematic events causing the unusual nature of the penetration channel and extreme deformation particles. (a) using spherical glyphs, and (b) using cube glyphs, suffer from the same problem of overlapping which serves to mask information. (c) alternately uses deformed parallelepiped glyphs which are able to accurately portray the massively deformed particle domains, including those which are physically unrealistic, such as the 'x' at the center of the screen, which is a single extremely stretched and sheared particle..

7.2 Automated Data Decimation and Visualization

A large Python script was developed to automate the visualization of penetration simulation results. This tool was further extended to be more generally applicable to other large solid mechanics Uintah data-sets. This script takes advantage of VisIt's Python scripting features and the increased efficiency gained by using VisIt from the command line. This was neccesitated by the size of each simulation data set and the delay that results from using VisIt remotely while making use of the university's high speed computing resources. This tool has the ability to indicate the depth of penetration on each frame (horizontal lines and text in Fig. 7.3) of a video and can easily be modified in order to highlight other quantities/features of interest. Using Python, scripts were also developed to generate plots of other useful information, such as depth of penetration through time (Fig. 7.4); rate of penetration through time (Fig. 7.5); penetrator total kinetic energy content through time (Fig. 7.6); discrete-penetrator individual segment kinetic energy content through time (Fig. 7.7); penetrator particle positions through time (Fig. 7.8); discrete jet segment radius, length, and mass profiles (Fig. 5.3) with associated velocity, momentum and kinetic energy

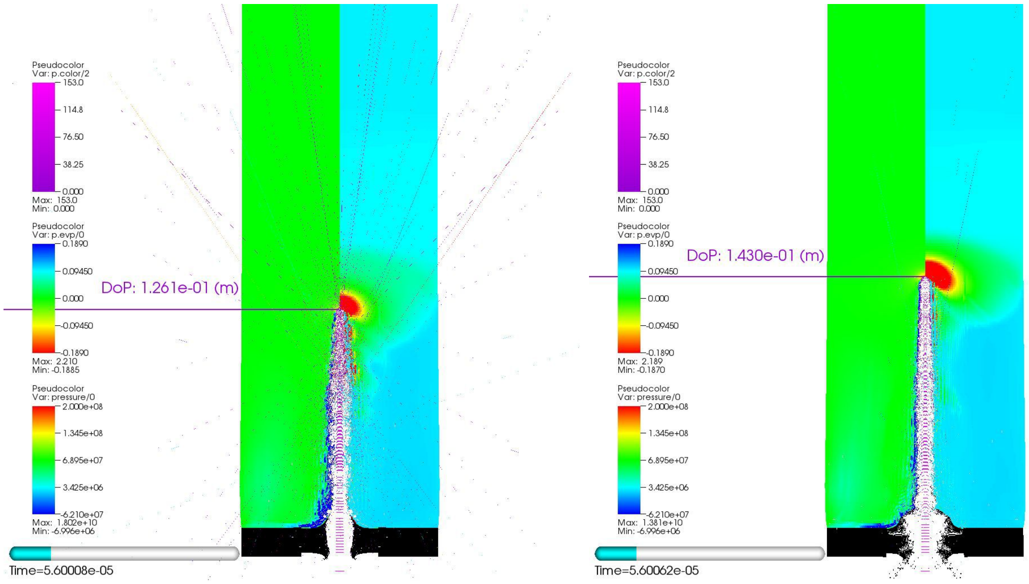

(a) *RemoveMass* (b) *ZeroStress*

Figure 7.3: Example video frame generated using automated visualization methods, demonstrating the ability to mark and label quantities of interest such as depth of penetration (DoP). (a) uses erosion algorithm *RemoveMass* while (b) uses erosion algorithm *ZeroStress*. Each is displayed at 56 μs, with the left half corresponding to plastic volumetric strain (center legend), and the right half corresponding to pressure (bottom legend), having the jet particles colors according to cylinder number (top legend).

.

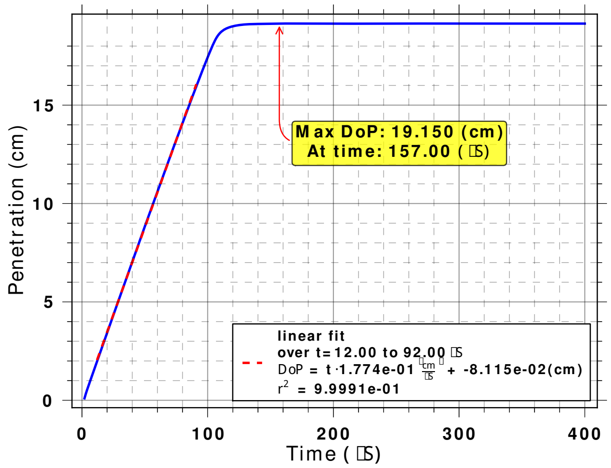

(a) ρ_p =9.618 g/cm^3 and L =147.08 mm

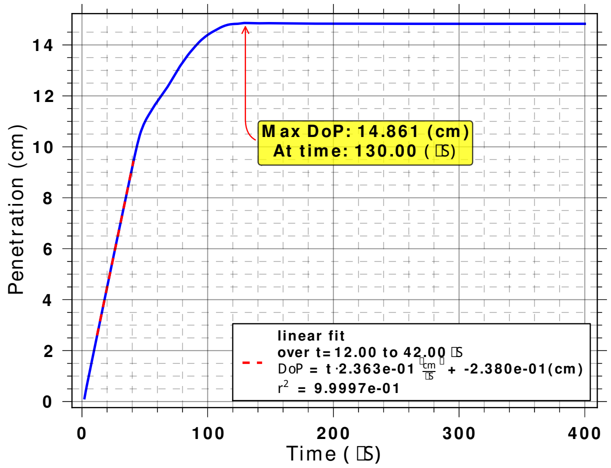

(b) ρ_p =38.470 g/cm^3 and L =36.78 mm

Figure 7.4: Example depth of penetration plots generated using automated visualization methods. A linear fit to steady state penetration, like that of Orphal and Anderson [71], is shown by the dashed red line and indicated in the legend. These plots demonstrate the combined effects of varying the penetrators density and length. In each case, the penetrator and target properties where otherwise the same.

deposition through time (Fig. 5.4); animations of particle/cell velocity, acceleration, and position through time including the same content for other particles within the same sphere of influence (Fig. 7.9), each of which has proved useful as a verification tool. The labels appearing in some of these plots were generated as part of the python script, not added in a photo editor after the fact. The source code used to achieve each of these different plots is available in the Appendix.

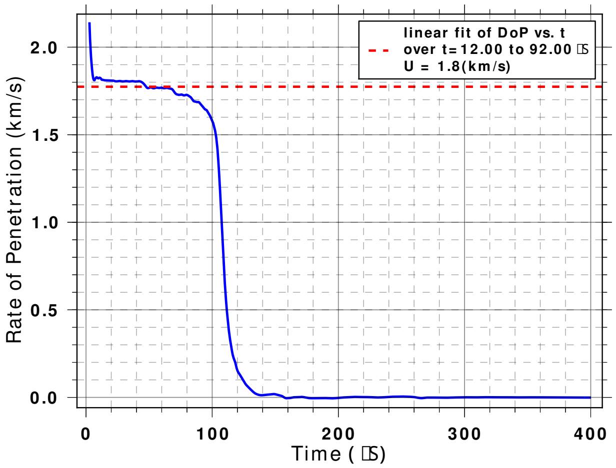

(a) ρ_p=9.618 g/cm^3 and L=147.08 mm

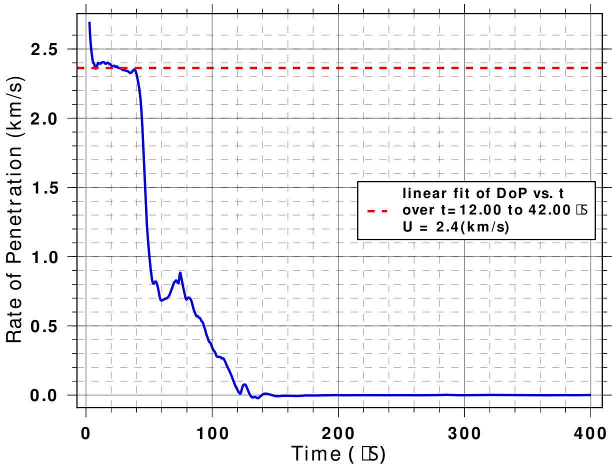

(b) ρ_p=38.470 g/cm^3 and L=36.78 mm

Figure 7.5: Example depth of penetration plots generated using automated visualization methods, demonstrating numerical differentiation by means of a Lagrange interpolating polynomial. In both cases, the steady-state penetration velocity of Fig. 7.4 is indicated by the dashed red line. Different information and plot formats can easily be specified by different argumentation or by setting default flags.

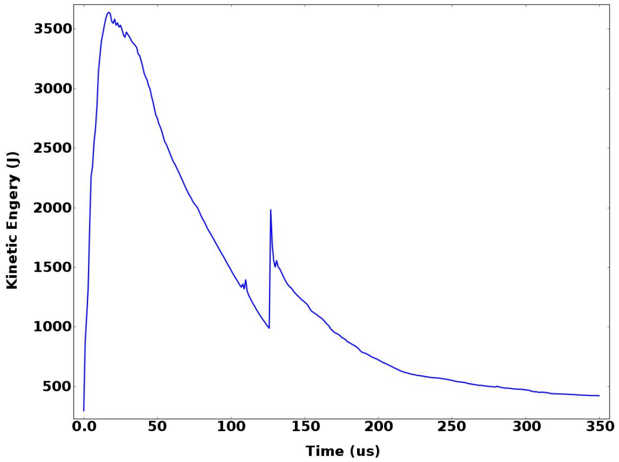

(a) *RemoveMass*

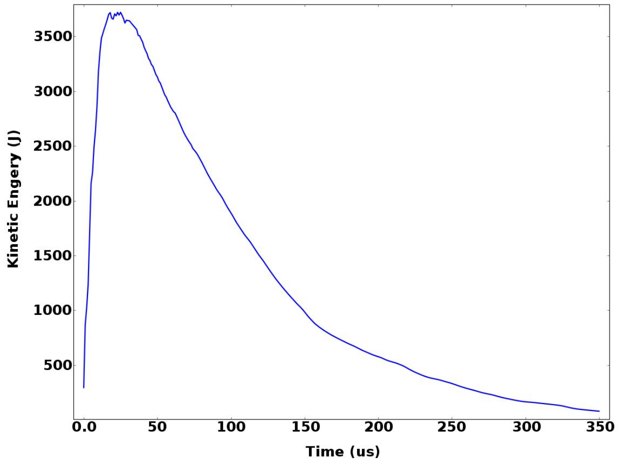

(b) *ZeroStress*

Figure 7.6: Example penetrator total kinetic energy plots generated using automated visualization methods. (a) corresponds to Fig. 7.3a, while (b) corresponds to Fig. 7.3b

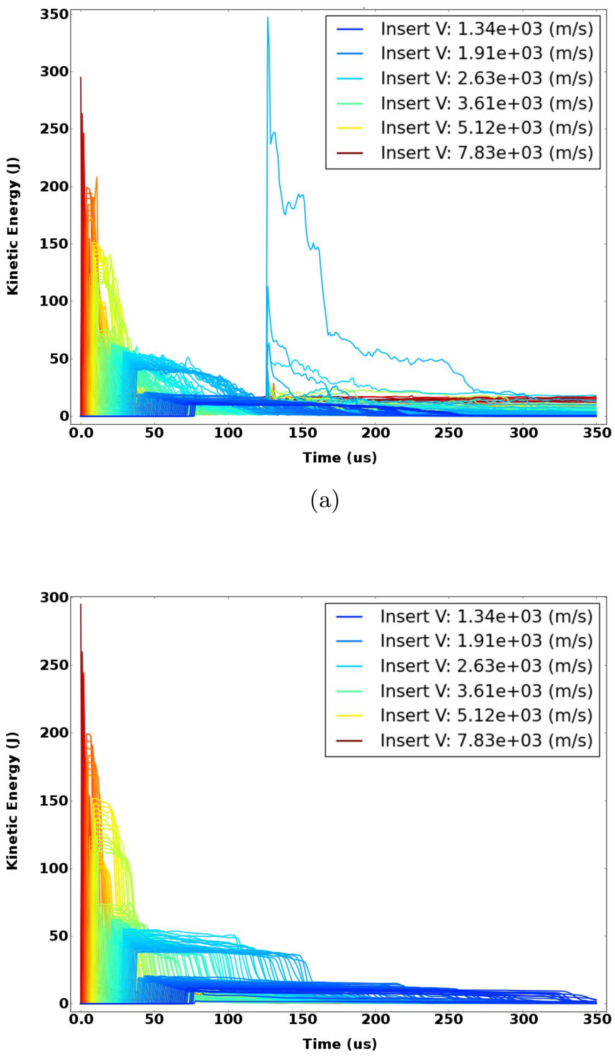

(a)

(b)

Figure 7.7: Example penetrator segment total kinetic energy plots generated using automated visualization methods. (a) corresponds to Fig. 7.3a, while (b) corresponds to Fig. 7.3b. Each is colored according to intial velocity as indicated in the legend.

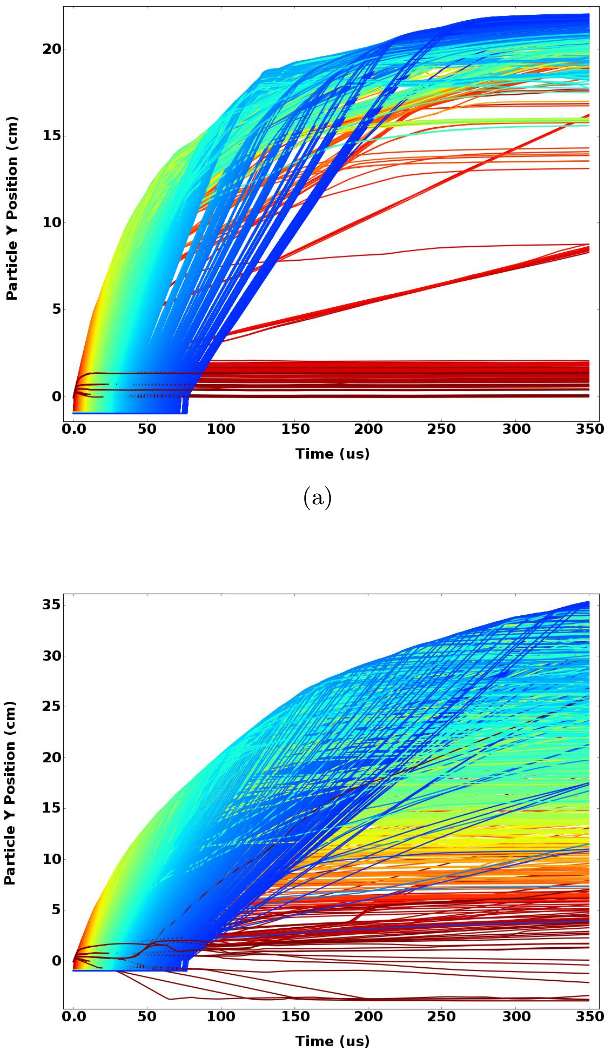

(a)

(b)

Figure 7.8: Example penetration histories of individual penetrator particles. (a) corresponds to Fig. 7.3a, while (b) corresponds to Fig. 7.3b. Each is colored according to intial velocity as indicated in the legend of Fig. 7.7, demonstrating the different behavior of both low and high speed jet particles, as they contribute to total penetration.

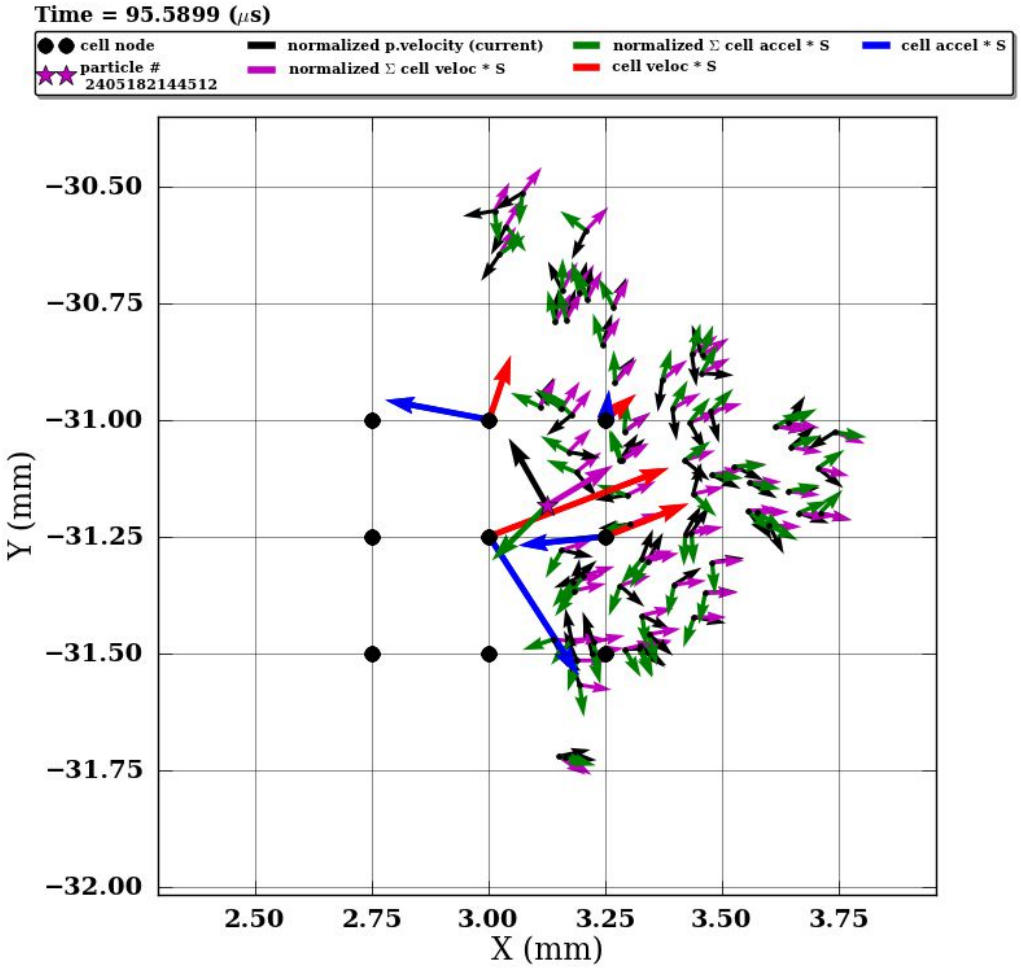

Figure 7.9: Example frame from an animated history of particle velocity, acceleration, and position. Black circles indiate the cell nodes that the particle represented by a magenta star interacts with. Other particles with the potential to influence these same grid nodes are drawn as small black dots. The large blue and red arrows, respectively, indicate the contribution of a node to the velocity and acceleration of the particle of interest. The black vectors represent the velocity of a particle, while the magenta and green vectors indicate the particle's velocity and acceleration mapped from the background grid. This animation demonstrated that, because particle position is updated by the cell velocity (magenta) while particle velocity (black) is updated by cell acceleration (green), there can be an effective decoupling of these quantities. The symptom is markedly different velocities reported by the code (black) and actual velocities (magenta). Vectors are not drawn to scale.

CHAPTER 8

SUMMARY AND FUTURE WORK

This research has provided a solid foundation for the application of V&V principles in the continued development of the material model Arenisca, as well as the MPM component of the Uintah computational framework. This foundation is built on tools that provide non-disruptive – often time-saving – verification testing as well as information-rich visualization of verification tests and larger validating simulations. Beyond contribution in the form of V&V tools, a strong dependence of simulation results on material parametrization and model options has been demonstrated. This is particularly evidenced by the discussion surrounding erosion algorithm selection. This calls in to question the use of larger simulations in validating the material model without first gaining credibility through the use of smaller verification tests, and further should serve as a warning to others concerning the use of features that have not been fully validated or documented. A large number of software bugs and algorithmic shortcomings were exposed and solved as a result of V&V, but many of these problems remain unsolved and thus represent avenues for future work with the potential for broad impact. These avenues, summarized below, relate both to the continued development of Arenisca, as well as to the larger host code framework Uintah.

8.1 Future Work

8.1.1 Resolution of the kinematic anomaly

This work has shown that the observed kinematic anomaly phenomenon is inherent to the implementation of kinematics within the host code Uintah. The cause and resolution of this issue should be first and foremost prior to approaching the other suggested items on this list, for the reason that without understanding the cause of such unusual and clearly nonphysical behavior, the accuracy of all unvalidated results have to be called into question. It is suspected that this issue is a problem associated with accumulative error, similar in nature to that produced when overdriving the integrator algorithms. While not covered in detail herein this suspicion is the result of probing simulations using the water dam problem of Mast *et al.* [75], which showed that the kinematic anomaly could be brought about earlier and more dramatically, or prevented altogether, by forcing the timestep to be larger or smaller than the stable CFL timestep.

8.1.2 Implementation of More Effective Anti-Locking Methods

It was shown that shear locking is prevalent within the host code Uintah, but without a better understanding of its cause or a validated resolution of this phenomena it cannot be determined how much this may be adversely affecting the predictive capabilities of simulations using Arenisca. Further, the development of a resolution different than that of Mast *et al.* [75] or a better understanding of the underlying mechanics of this phenomena has the potential for broad impact within the MPM and numerical methods communities.

8.1.3 Accurate Computation of the Strain Rate

Some points in simulations of hypervelocity impact are exhibiting very high shear and hence large rotation of the principal directions of reference stretch, possibly resulting in large errors in the constitutive model's approximation of Hencky strain rate by the symmetric part of the velocity gradient. Accordingly, one avenue for improvement might be to accurately compute the Hencky strain. To validate such an improvement, controlled experimental data at large shear would be advisable.

8.1.4 Splitting/Deletion/Freezing of Damaged/Failed Particles

If the previous method is deemed to cost to much computationally or be ineffective at preventing massively sheared and stretched particles it is suggested that alternative means of preventing these particles states from occurring be sought out as is not entirely clear what affect such deformations might have the underlying kinematics algorithms. It was shown that use of the erosion option *ZeroStress*, which acts to freeze the deformation of damaged particles produced more robust, albeit unvalidated results, demonstrating that particle domain freezing, and the modification of a particles state in other ways may be an effective solution. Alternatively, particle deletion has been explored, though this has the unintended consequence of failing to conserve mass, and depending on implementation, momentum. Yet another alternative is particle splitting, which has shown some promise in the SPH community. This method though, is not without its drawbacks. As a result of the way the stable timestep is computed within Uintah, the splitting of a particle results in a decrease of the stable time step. As small timesteps are already an issue this is a troubling side effect.

In this same category, it is also noted that the ability of the convected particle domain interpolation (CPDI) method to accommodate fractional particles [24] makes this method a good candidate to use fractional particles (*i.e.,* particles spanning over multiple cells) in regions like the outer boundaries, which are of low interest and subjected to small deformations. Doing this could significantly reduce the computational cost of these regions without a loss in the accuracy of simulation results.

8.1.5 Continued Validation Through Comparison Against Analytical Theory and Experimental Observations using Simplified Tests

It has been shown that simulations of hypervelocity penetration produce a linear relationship between penetration velocity and penetrator velocity as pointed out by Orphal Anderson [71]. Further validation could be produced through use of the Eichelberger/Alekseevskii-Tate governing equations and this relationship by first establishing the values of a and b used to compute $R-Y$. This equation for $R-Y$ could then be used to produce a situation where $\rho_t(V-U)^2 = 2(R-Y)$, for which the penetration should reduce to that of hydrodynamic Bernoulli theory.

8.1.6 Development of a plastic strain and Damage/Permeability Correlation

In its present form, the Arenisca model supports softening only in the limited form that allows the cap to retract, representing an increase in porosity. However, softening ought to also degrade the shear strength of the material by collapsing the limit surface, and this effect is not yet supported in Arenisca. Basic formulations of softening have proved to significantly improve predictions of the more complicated Kayenta model, but incorporation of softening generally also requires explicitly including Aleatory uncertainty and its associated scale effects. Moreover, the tendency of softening to induce strongly mesh dependent predictions remains as an active area of research in the Literature.

8.1.7 Nonlinear Non-Drucker-Prager Limit Surface

The constitutive model currently predicts an ever-increasing shear strength with confinement pressures. However, at the extremely high pressures expected in the vicinity of a penetrator, it is reasonable to assume the the shear strength should eventually become pressure-independent. This behavior might be accommodated by revising the current linear

Drucker-Prager limit surface to become a nonlinear Drucker-Prager surface (*c.f.* [35]) or such a response might even be achieved by allowing the CR ratio of the cap to evolve appropriately.

At low pressures, on the other hand, pressure-sensitivity of strength not only tends to be pronounced (*e.g.,* from frictional effects at sliding microscale flaws), but the limit surface should also include third-invariant dependence, generally giving the cross-section a triangular (non-Drucker-Prager) shape at low pressures.

8.1.8 Texture, Both Intrinsic and Induced

Natural geological formations are layered and thus tend to be at least transversely isotropic, which is not included in the Arenisca model. Some support for rock jointing is included in the more sophisticated Kayenta model, but even that model has no means of predicting the texturing that results from deformation itself. Although ample evidence exists to show that rock is textured, very little progress has been made to model it. In addition to difficulties in constitutive model development, many host codes inadvertently include assumptions of isotropy. These codes, for example, often use a Courant timestep condition based on a single wave velocity that is the same in all directions, which does not apply to textured media. Transmitting boundary conditions likewise rarely work correctly for anisotropic media, since these also are typically written only for linear-elastic media.

8.1.9 Development of Path Dependent Plasticity Verification Tests

As simulated phenomenon become increasingly complex, the existence of models against which to validate results will become increasingly scarce. For this reason, the existence of well-formulated model-specific verification problems becomes more important as part of the V&V process. The method of manufactured solutions [27] appears to be a good candidate for developing nontrivial path-dependent verification tests.

8.2 Summary

This research has addressed the incorporation of basic V&V methods into the continued development of the Arenisca plasticity model. As part of this effort, tools that are also generally applicable to other solid mechanics problems have been made available to users of the research code Uintah and visualization tool VisIt. Further, a large number of avenues for future work have been identified, both within the host code Uintah and material model Arenisca. Many of which may represent fundamental problems, which will need to be addressed, prior to the wellbore completions process being simulated within this framework with high confidence. The deliverables of this research are:

- **Literature review** This focused review will help others attempting to simulate the wellbore completions process as it highlights the strengths and weaknesses of current analytical formulations, which might serve as verification or validation. This will be particularly valuable to researchers continuing the development of Arenisca whom will need a way to validate this model in the future.
- **Automation of existing V&V testing** A testing suite was devised, which meets the needs of model developers. This suite makes verification fast and simple, providing quick and painless confirmation that features have been correctly implemented, or in the event of an error, an information rich way to visually debug a problem. The framework is easy to modify and has already been extended to use outside this project by other developers.
- **Improvement and extension of single element testing abilities** The ability to faithfully repeat a single particles deformation history in the form a single element test was added to the list of Uintah's features. This is, to the this author's knowledge, a first for a code of this type and/or on this scale. So that users might better take advantage of this feature a number of tools were developed, which provide users with a way to modify and compare these particle histories.
- **Improvement of postprocessing methods** Data visualization methods were significantly improved to provide high fidelity representations of actual particle deformation throughout a simulation. This is particularly important as these deformations serve as input to the constitutive model at the most fundamental level making an understanding of their development crucial to an understanding of a models response. Other visualization tools were also developed, which will serve researchers as they continue to predictively model hypervelocity impact and penetration phenomena with Uintah and its associated material models.
- **Execution of a large number of simulations meant to serve as validation** A large number of simulations were executed and their results compared quantitatively against analytical theory as well as qualitatively against expected trends. These comparisons indicate both that significant progress has been made in the development of Arensica as well as that certain issues remain unresolved.
- **Investigation of unexpected results** The simulations above highlighted a number of fundamental problems with the Uintah host code and Arenisca. These problems

were explored at length and a number of possible causes ruled out. Resolution of these problems has the potential to greatly impact all users of the Uintah MPM framework and even provide fundamental insight to the greater MPM community at large.

APPENDIX

SIMULATION INPUTS AND SOURCE CODE

Simulation input decks (a term originating from when punch cards where still used in computer science) used with Uintah to obtain the results herein as well as the various scripts written to postprocess the results are available on the ‘csm-users’ subversion repository. Speak with Dr. Brannon or her lab manager to obtain access to this resource.

A.1 Simulation Inputs

Input decks can be found at the path ‘.../csm-users/Dave/thesis/inputs/’. The text file at the same path named ’readme.txt’ gives a brief explanation of each simulation. Where available, results (such as a the jet history ‘jetHistory.dat’) for use with the penetration postprocessor, can be found within the sub folder ‘results’ for each simulation.

A.2 Source Code

The automated visualization script (and associated files“) for use with the visualization tool VisIt can be found at the path ‘.../csm-users/Dave/thesis/code/autoVis/’ with a read-me file documenting methods and use found at the same path by the name ’readme.txt’.

Penetration postprocessing scripts (past and present including some helpful misc utilities) can be found at the path ‘.../csm-users/Dave/thesis/code/postProc/’ with a read-me file documenting methods and use for each found at the same path by the name ’readme.txt’.

REFERENCES

[1] Kennedy, D. R., 1983. "History of the shaped charge effect - the first 100 years," Tech. Rep. ADA220095, Los Alamos National Laboratories, Alamos, New Mexico, 20-22 September.

[2] Walters, W. "An overview of the shaped charge concept," pdf, October.

[3] Birkoff, G., MacDougall, D., Pugh, E., and Taylor, G., 1948. "Explosives with lined cavities," Journal of Applied Physics, **19**, pp. 563–582.

[4] Walters, W., 2008. "A brief history of shaped charges," in Reprint 24th International Symposium on Ballistics, Vol. 1, pp. 3–10.

[5] Poole, C., 2005. "Penetration of a shaped charge," PhD thesis, Corpus Christi College University of Oxford.

[6] Walters, W. P., Flis, W., and Chou, P., 1988. "A survey of shaped-charge jet penetration models," Journal of Impact Engineering, **7**, pp. 307–325.

[7] Gladkikh, M., Harvey, W., Hughes, B., and Halleck, P., 2009. "Predicting depth of penetration of downhole perforators," in Annual Technical Conference and Exhibition, Society of Petroleum Engineers.

[8] Alekseevski, V., 1966. "Penetration of a rod into a target at high velocity," Combustion Explosion and Shock Waves, **2**, pp. 63–66.

[9] Tate, A., 1967. "A theory for the deceleration of long rods after impact," Journal of Mechanics and Physics of Solids, **15**, pp. 387–399.

[10] Walters, W. P., and Segletes, S. B., 1991. "An exact solution of the long rod penetration equations," International Journal of Impact Engineering, **11**(2), pp. 225–231.

[11] Walters, W. P., and Williams, C. L., 2006. "The influence of armor material parameters on the penetration by long-rod projectiles," in ASME Pressure Vessels and Piping Conference Proceedings.

[12] S. B. Segeletes, W. P. W., 2002. ""Efficient solution of the long-rod penetration equations of alekseevskii-tate," Tech. Rep. ARL-TR-2855, Army Research Laboratory, Aberdeen Proving Ground, MD, September.

[13] Sadeghirad, A., and Brannon, R., 2012. *Development and Implementation of Arenisca, a Simplified Geomodel, in Uintah,* University of Utah Computational Solid Mechanics Group, June.

[14] Brannon, R., and Leelavanichkul, S., 2010. "A multistage return algorithm for solving the classical damage component of constitutive models for rocks, ceramics, and other rock-like media," International Journal of Fracture, **163**, pp. 133–149.

[15] Guilkey, J., Harman, T., Luitjens, J., Schmidt, J., Thornock, J., de St. Germain, J. D., Shankar, S., and Joseph Peterson, C. B., 2009. "Uintah user guide," Tech. Rep. UUSCI-2009-007, Scientific Computing and Imaging Institute University of Utah, September.

[16] Sulsky, D., Chen, A., and Schreyer, H., 1994. "A particle method for history-dependent materials," Computer Methods in Applied Mechanics and Engineering, **118**, pp. 179–196.

[17] Sulsky, D., Zhou, S.-J., and Schreyer, H. L., 1995. "Application of a particle-in-cell method to solid mechanics," Computer Physics Communications, **87**(12), pp. 236 – 252.

[18] McCorquodale, J., de St. Germain, J., Parker, S., and Johnson, C., 2001. "The Uintah parallelism infastructure: A performance evaluation," in Proceedings of the 5th International Conference on High-Performance Computing.

[19] de St. Germain, J., McCorquodale, J., Parker, S., and Johnson, C., 2000. "Uintah: A massively parallel problem solving environment," in Ninth IEEE International Symposium on High Performance and Distributed Computing, IEEE, Piscataway, NJ, pp. 33–41.

[20] Wallstedt, P., and Guilkey, J., 2007. "Improved velocity projection for the material point method," CMES - Computer Modeling in Engineering and Sciences, **19**(3), pp. 223–232.

[21] Bardenhagen, S., and Kober, E., 2004. "The generalized interpolation material point method," CMES - Computer Modeling in Engineering and Science, **5**(6), pp. 477–495.

[22] Wallstedt, P., and Guilkey, J., 2008. "An evaluation of explicit time integration schemes for use with the generalized interpolation material point method," Journal of Computational Physics, **227**(22), pp. 9628 – 42.

[23] Sadeghirad, A., Burghardt, J., and Brannon, R., 19-23, July, 2010. "An algorithm for improving the accuracy and stability of the generalized interpolation material point method," 9th World Congress on Computational Mechanics and 4th Asian Pacific Congress on Computational Mechanics (WCCM/APCOM2010), Sydney, Australia.

[24] Sadeghirad, A., Brannon, R. M., and Burghardt, J., 2011. "A convected particle domain interpolation technique to extend applicability of the material point method for problems involving massive deformations," International Journal for Numerical Methods in Engineering, **86**(12), pp. 1435–1456.

[25] Brannon, R., 2011. "Verification and validation of computational models for shaped charge jet completion of well bores in fluid saturated sandstone", in APS Shock Compression of Condensed Matter Meeting Abstracts, p. L6001.

[26] Kamojjalam, K., and Brannon, R. M., 2011. "Verification of frame indifference for complicated numerical constitutive models," in ECTC Proceedings ASME Early Career Technical Conference, ASME District E and University of Arkansas.

[27] Brannon, R. M., Kamojjala, K., and Sadeghirad, A., 2011. "Establishing credibility of particle methods through verification testing," in II International Conference on Particle-based Methods - Fundamentals and Applications.

[28] Brannon, R., and et. al., 2009. "University of Utah computational solid mechanics (CSM) 2009 annual report," Tech. Rep.

[29] Brannon, R., and et. al., 2010. "University of Utah computational solid mechanics (CSM) 2010 annual report," Tech. Rep.

[30] Burghardt, J., Leavy, B., Guilkey, J., Xue, Z., and Brannon, R., 2010. "Application of Uintah–mpm to shaped charge jet penetration of aluminum," IOP Conference Series: Materials Science and Engineering, **10**, pp. 12223–12232.

[31] Brannon, R., and et. al., 2011. "University of Utah computational solid mechanics (CSM) 2011 annual report," Tech. Rep.

[32] Brannon, R., and et. al., 2012. "University of Utah computational solid mechanics (CSM) 2012 annual report," Tech. Rep.

[33] ASME, 2006. *V&V 10-2006 (2006) Guide for verification and validation in computational solid mechanics.* The American Society of Mechanical Engineers.

[34] Reddy, J., 2008. *An introduction to continuum mechanics with applications*, 1st ed. Cambridge University Press.

[35] Brannon, R., Fossum, A., and Strack, O., 2009. *KAYENTA: Theory and user's guide*, sand2009-2282 ed. Sandia National Laboratories, March.

[36] Brannon, R. M., 2007. "Elements of phenomenological plasticity: Geometrical insight, computational algorithms, and topics in shock physics," in *ShockWave Science and Technology Reference Library*, Y. Horie, ed. Springer Berlin Heidelberg, pp. 225–274.

[37] Malvern, L., 1977. *Introduction to the mechanics of a continuous medium,* Prentice–Hall.

[38] Walters, W., and Zukas, J. A., 1989. *Fundamentals of shaped charges,* Wiley-Interscience.

[39] Pack, D. C., and Evans, W. M., 1951. "Penetration by high-velocity ('munroe') jets: I," Proc. Phys. Soc., **B64**, pp. 298–303.

[40] Eichelberger, R., 1956. "Experimental test of the theory of penetration by metallic jets," Journal of Applied Physics, **27**, pp. 63–68.

[41] Grove, B., 2006. "Theoretical considerations on the penetration of powdered metal jets," International Journal of Impact Engineering, **33**, pp. 316–325.

[42] Bin, L., and HeMing, W., 2010. "Alekseevskii-tate revisited: An extension to the modified hydrodynamic theory of long rod penetration," *Sci China Tech Sci,* **53**, May, pp. 1364–1373.

[43] Walters, W., Williams, C., and Normandia, M., 2006. "An explicit solution of the alekseevski–tate penetration equations," International Journal of Impact Engineering, **33**(112), pp. 837 – 846.

[44] Allison, F., and Vitali, R., 1963. "A new method of computing penetration variables for shaped-charge jets," Tech. Rep. 1184, Ballistic Research Laboratories, Aberdeen Proving Ground, Maryland, January.

[45] DiPersio, R., and Simon, J., 1964. “The penetration-standoff relation for idealized shaped charge jets.,” Memorandum 1542, Ballistic Research Laboratory.

[46] DiPersio, R., Simon, J., and Merendino, A., 1965. “Penetration of shaped-charge jets into metallic targets,” Memorandum 1296, Ballistic Research Laboratory.

[47] Raatschen, H., Pavel, W., Fuchs, S., Senf, H., and Rothenhausler, H., 1989. “Penetration efficiency of segmented rods,” in Proceeding of the 11th Internation Symposium on Ballistics.

[48] Charters, A., 1986. “The penetration of rolled homogeneous armor by continious and segmented rods at high velocity: Theory and experiments,” Tech. Rep. CR-86-1031, General Research Corporation, April.

[49] Zukas, J. A., 1990. “Numerical simulation of semi-infinite target penetration by continious and segmented rods,” Tech. Rep. BRL-TR-3081, Ballistic Research Laboratory, Aberdeen Proving Ground, MD, February.

[50] Flis, W., and Crilly, M., 1999. “Hypervelocity jet penetration of porous materials,” in Proceedings of the 18th International Symposium on Ballistics, Vol. 2, pp. 869–876.

[51] Walker, J. D., and Jr., C. E. A., 1995. “A time-dependent model for long-rod penetration,” International Journal of Impact Engineering, **16**(1), pp. 19 – 48.

[52] Novokshanov, R., and Ockendon, J. R., 2006. “Elastic-plastic modelling of shaped charge jet penetration,” in Proceedings of Royal Society of London A, no. ISSN 2006-1751, pp. 1–21.

[53] Aseltine, C., 1985. “Flash x-ray analysis of the interaction of perforators with different target materials, spe 14322,” in SPE 60th Annual Technical Conference and Exhibition, SPE.

[54] Asadi M., e. a., 1994. ““Effect of the perforation damage on well productivity,” in SPE Intl. Symposium on Formation Damage Control, Society of Petroleum Engineers.

[55] Behrmann, L., Grove, B., Walton, I., Zhan, L., Graham, C., and D. Atwood, J. H., 2009. “A survey of industry models for perforator performance: suggestions for improvements, spe 125020,” in SPE Annual Technical Converence and Exhibition, Society of Petroleum Engineers.

[56] Wesson, D. S., 1991. “Improved system test for perforators, spe 22813,” in 66th Annual Technical Conference and Exhibition of the Society of Petroleum Engineers, Society of Petroleum Engineers.

[57] Harvey, J., Grove, B., Zhan, L., and Behrmann, L., 2010. “New predictive model of penetration depth for oilwell-perforating shaped charges,” in SPE International Symposium and Exhibition on Formation Damange Control, Society of Petroleum Engineers.

[58] Grove, B., Heiland, J., Walton, I., and Atwood, D., 2008. “New effective stress law for predicting perforation depth at downhole conditions,” in SPE International Symposium and Exhibition on Formation Damage Control, no. SPE 111778, Society of Petroleum Engineers.

[59] Harvey, J., and B. Grove and, L. Z., 2012. “Stressed rock penetration depth correlation,” Society of Petroleum Engineers (SPE).

[60] Thompson, G. D., 1962. ““Effects of formation compressive strength on perforator performance,” in Drilling and Production Practice Conference Proceedings.

[61] Grove, B., Heiland, J., and Walton, I., 2007. “Shaped charge penetration into stressed rock,” in 23rd International Symposium on Ballistics.

[62] Ma, S., and Zhang, X., 2009. “Comparison study of mpm and sph in modeling hypervelocity impact,” International Journal of Impact Engineering, **36**, pp. 272–282.

[63] Resende, L., and Martin, J., 1985. “Formulation of drucker-prager cap model,” Journal of Engineering Mechanics **111**(7), July, pp. 855–881.

[64] Brannon, R., 2011. “Primer on the simplest inelastic model: non-hardening von mises (j2) plasticity,” pdf, October.

[65] Noll, W., 1995. “On material frame-indifference,” Tech. Rep. Paper 580, Carnegie Mellon University Department of Mathematical Sciences, January.

[66] Rashid, M. M., 1993. “Incremental kinematics for finite element applications,” Int. J. Numer. Methods Eng., **36**, pp. 3937–3956.

[67] Zukas, J., Nicholas, T., Swift, H., Greszczuk, L., and Curran, D., 1982. *Impact dynamics,* Wiley-Interscience.

[68] Guilkey, J., 2012. “Email concerning exact single element deformation,” private communication, Aug 25.

[69] Courant, R., Friedrichs, K., and Lewy, H., 1967. “On the partial difference equations of mathematical physics,” IMB J. Res. Dev. **11**(2), Mar., pp. 215–234.

[70] Wesson, D., and Pratt, D., 1992. “The effects of target configuration on the performance of deep-penetrating shaped charges,”.

[71] Orphal, D., and Jr., C. A., 2006. “The dependence of penetration velocity on impact velocity,” International Journal of Impact Engineering, **33**(112), pp. 546 – 554.

[72] Partom, Y., 1997. “On the hydrodynamic limit of long rod penetration,” International Journal of Impact Engineering, **20**(610), pp. 617 – 625.

[73] Lach, E., Anderson, C., Schirm, V., and Koerber, G., 2008. “Hypervelocity impact into a high strength and ductile steel alloy,” International Journal of Impact Engineering, **35**(12), pp. 1625 – 1630.

[74] Guilkey, J., 2012. “Meeting in person. Weekly project meeting,” private communication, Nov 29.

[75] Mast, C., Mackenzie-Helnwein, P., Arduino, P., Miller, G., and Shin, W., 2012. “Mitigating kinematic locking in the material point method,” Journal Of Computational Physics, **231**(16), pp. 5351–5373.

[76] Bower, A. F., 2009. *Applied mechanics of solids,* CRC Press, October.

[77] Felippa, C. A., 2005. “Appendix 3 locking,” pdf, May.

[78] Steffen, M., Kirby, R. M., and Berzins, M., 2008. "Analysis and reduction of quadrature errors in the material point method (mpm)," International Journal for Numerical Methods in Engineering, **76**(6), pp. 922–948.

[79] Cantrell, C. A., 2008. "Technical note: Review of methods for linear least-squares fitting of data and application to atmospheric chemistry problems," Atmospheric Chemistry and Physics Discussions, **8**(2), pp. 6409–6436.

[80] Zheng, Y., Gao, F., Zhang, H., and Lu, M., 2013. "Improved convected particle domain interpolation method for coupled dynamic analysis of fully saturated porous media involving large deformation," Computer Methods in Applied Mechanics and Engineering, **257**(0), pp. 150 – 163.

[81] Johnson, G. R., and Cook, W. H., 1985. "Fracture characteristics of three metals subjected to various strains, strain rates, temperatures and pressures," Engineering Fracture Mechanics, **21**(1), pp. 31 – 48.

[82] Murr, L., Staudhammer, K., and Meyers, M., 1986. *Metallurgical applications of shock-wave and high-strain-rate phenomena* Mechanical Engineeging. Taylor & Francis.

[83] Ruden, E., and Kiuttu, G., 2000. "Adiabatic, shock, and plastic work heating of solids and the cylinder test," Final Report AFRL-DE-TR-2000-1100, Air Force Research Laboratory, 3550 Aberdeen Ave SE Kirtland AFB, NM 87117-5776, May.

[84] Ravichandran, G., Rosakis, A., Hodowany, J., and Rosakis, P., 2001. "On the conversion of plastic work into heat during high-strain-rate deformation," in 12th APS Topical Conference on Shock Compression of Condensed Matter, Vol. 620, American Physical Society, pp. 557–562.

[85] Johnson, J., and Addessio, F., 1988. "Tensile plasticity and ductile fracture," Journal of Applied Physics, **64**(12), 15 December, pp. 6699–6712.

[86] Drucker, D., of Engineering, B. U. D., and of Naval Research, U. S. O., 1957. *A definition of stable inelastic material,* Tech Rep (Brown University. Division of Engineering). Division of Engineering, Brown University.

[87] Guilkey, J., 2013. "Meeting in person," private communication, May 29.

[88] Jr., C. E. A., Hohler, V., Walker, J. D., and Stilp, A. J., 1995. "Time-resolved penetration of long rods into steel targets," International Journal of Impact Engineering, **16**(1), pp. 1 – 18.

[89] Orphal, D., and Franzen, R., 1990. "Penetration mechanics and performance of segmented rods against metal targets," International Journal of Impact Engineering, **10**(14), pp. 427 – 438.

[90] Scheffler, D. R., and Zukas, J. A., 1990. "Numerical simulation of segmented penetrator impact," International Journal of Impact Engineering, **10**(14), pp. 487 – 497.

[91] Lee, M., and Normandia, M., 1999. "Successive impact of segmented rods at high-velocity," KSME International Journal, **13**(4), pp. 312–320.

[92] Cuadros, J., 1990. "Monolithic and segmented projectile penetration experiments in the 2 to 4 kilometers per second impact velocity regime," International Journal of Impact Engineering, **10**(14), pp. 147 – 157.

[93] Sorensen, B., Kimsey, K., Silsby, G., Scheffler, D., Sherrick, T., and de Rosset, W., 1991. "High velocity penetration of steel targets," International Journal of Impact Engineering, **11**(1), pp. 107 – 119.

[94] Lambert, D., 2008. "Re-visiting 1-d hypervelocity penetration," International Journal of Impact Engineering, **35**(12), pp. 1631 – 1635.

[95] Presnell, M. B., and Rajendran, A. M., 2011. "A computational study of segmented tungsten rod penetration into a thick steel plate at high velocities," in AIP Conference Proceedings, Vol. 1426, American Institute of Physics, American Institute of Physics, pp. 80–83.

[96] Childs, H., Brugger, E. S., Bonnell, K. S., Meredith, J. S., Miller, M., Whitlock, B. J., and Max, N., 2005. "A contract-based system for large data visualization," in Proceedings of IEEE visualization 2005, pp. 190–198.

[97] Neeman, A. G., 2009. "Visualization techniques for computational mechanics," PhD in computer science, University of California Santa Cruz, December.

[98] Choudhury, A. I., Steffen, M., Guilkey, J., and Parker, S., 2010. "Enhanced understanding of particle simulations through deformation-based visualization," Computer Modeling in Engineering and Sciences, **63**(2), pp. 117–136.